THE UNIVERSITY OF CHICAGO

ROLE OF DISORDER IN III-V NANOCRYSTAL EMITTERS AND SELF ASSEMBLY OF CHARGE STABILIZED COLLOIDS

A DISSERTATION SUBMITTED TO
THE FACULTY OF THE DIVISION OF THE PHYSICAL SCIENCES
IN CANDIDACY FOR THE DEGREE OF
DOCTOR OF PHILOSOPHY

DEPARTMENT OF CHEMISTRY

BY
ERIC MCNEAL JANKE

CHICAGO, ILLINOIS
AUGUST 2019

Table of Contents

List of Figures

List of Tables

Acknowledgements

I would like to thank all those who have provided me aid, guidance, expertise, and support over my time at The University of Chicago, a PhD is by no means a solo journey. First and foremost, I want to thank my advisor Dmitri Talapin for his mentorship and support and for always pushing me to expand my horizons, think creatively, and for teaching me the importance of continuously leaving my comfort zone and acquiring new skills in new areas. I want to also thank all members of my defense committee, Professors Dmitri Talapin, Gregory Engel, and Bozhi Tian. I am grateful to all of the Talapin Lab members with whom I have worked over my time here, especially Dr. Vishwas Srivastava, Margaret Hudson, Dr. Matthew Panthani, and Dr. Igor Fedin whose conversations have provided me with crucial feedback and inspiration. Among collaborators, I owe a particular thanks to Dr. Nicholas Williams, Dr. Danny Haubold, Dr. Chunxing She, Dr. Danylo Zherebetskyy, and Dr. Trung Dac Nguyen for their invaluable contributions. I am in debt to all those who maintained the physical infrastructure that my research depended on, including facilities managers at The University of Chicago, Dr. Justin Jureller, Dr. Qiti Guo, Dr. Alexander Filatov, Dr. Jin Qin, Yimei Chen, and Dr. Jotham Austin provided training and kept instrumentation, equipment, and facilities in excellent shape. At Argonne National Laboratory, I had help in both scientific expertise and instrumentation from staff at The Center for Nanomaterials and The Advanced Photon Source, Dr. David Goztola, Prof. Richard Schaller, Dr. Benjamin Diroll, Dr. Chengjun Sun and Dr. Byeongdu Lee. Finally, I want to thank my parents, Mike and Sue Janke and my brother, Scott, for their never-ending support and encouragement through highs and lows.

Abstract

I begin this dissertation with an overview of the colloidal nanomaterials field and highlight the versatility of colloidal methods for producing nanoscale soluble precursors to useful optoelectronic materials. The subsequent content is divided broadly between two aspects of colloidal nanomaterials science. In the first portion, Chapters 2 and 3, I discuss an in-depth study of the properties of InP quantum dot emitters with an emphasis on elucidating the barriers to achieving better performance and providing a path forward for future optimization. Chapter 2 covers an investigation into carrier dynamics in these materials by a range of spectroscopic techniques and presents evidence of defect coupled emission in passivated InP quantum dots. Chapter 3 continues to explore InP quantum dot emitters by following up on the hypothesis of defect coupled emission presented at the end of Chapter 2, and makes use of Raman spectroscopy, x-ray absorption fine structure spectroscopy and density functional theory calculations. Here, I aim to observe and account for classes of structural disorder in InP quantum dot emitters that can lead to defect coupled emission and persistently broad ensemble emission linewidths. In the latter portion of the document, Chapters 4 and 5, I turn the focus away from the properties of isolated colloidal particles and toward studying assembly of extended solids composed of colloidal nanomaterials. In particular, I examine the relation between surface chemistry and interparticle forces. I study the effect of this relationship on the morphology of aggregates grown from colloids that are electrostatically stabilized by compact inorganic ligands. In Chapter 4, I present a new method for growing ordered and maximally dense supercrystals of metal nanoparticles capped with inorganic ligands. Characterization of structural, optical, and electronic properties of these assemblies verifies strong electronic coupling and macroscopically metallic behavior. In Chapter 5, I investigate the mechanism of densification and ordering in these assemblies and find that an

interaction between the high polarizability of the individual nanocrystal units and asymmetric electrolyte species in solution produces a crucial short-range repulsive potential. It is this repulsion that prevents particles from jamming and allows for the system to settle into the thermodynamically favored, ordered, and dense supercrystalline phase.

1. Introduction

1.1 Colloidal nanoparticles as nanoscale building blocks for bottom-up construction of functional materials with designed properties

Countless technological achievements that have transformed societies and built the modern era have centered around understanding and manipulating matter at small legthscales. Efforts to extend and continue this progressive evolution of technology will require scientific investigation into natural phenomena that emerge at the nanometer scale in order to expand the scope of future possibilities. To this end, colloidal nanocrystals have recently attracted a great deal of interest for their potential as functional nanoscale building blocks[1,2]. Synthesized in the colloidal phase[3] and amenable to modification[4] and processing[5] by a wide variety of techniques, they have been investigated for applications in catalysis[6,7], magnetic storage[8], medicine[9-11], lighting and displays[12,13], and thin-film electronic devices[14,15]. Figure 1-1 depicts a typical workflow for processing colloidal nanoparticles into a thin-film coating. Following particle growth chemistry in a reaction vessel (a), particles are purified and formulated into an ink (b), which can

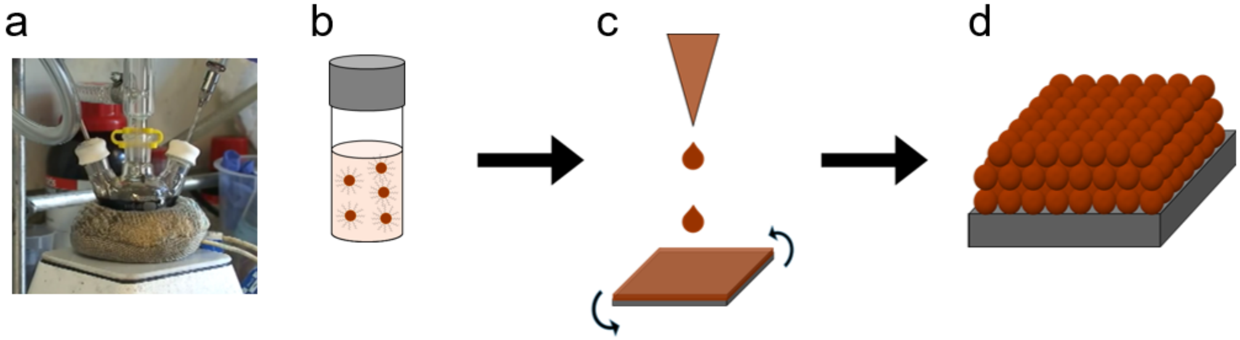

Figure 1-1: Scheme summarizing a process for fabricating a thin-film coating from nanocrystals. (a), synthesis in the colloidal phase by introduction of precursor species into a growth medium containing long-chain surfactant species. (b), formulation of a stable nanoparticle ink. (c), casting a thin film by e.g. spincoating. (d) dry solvent, conduct chemical post-treatments, to yield a thin coating consisting of an extended 3D solid made up of individual nanocrystal units.

then be cast onto a substrate by spincoating, slot-die casting, ink-jet printing etc. (c), to form an extended solid film of nanocrystals. Chemical treatments to modify the nanoparticle surfaces may accompany any of these four steps.

Colloidal synthesis techniques can access semiconducting[16], magnetic[17] and metallic[7,18,19] particles control over size, shape and surface chemistry. Figure 1-2 shows images of selected examples of these classes of colloidal nanoparticles dried on an amorphous carbon support and imaged by transmission electron microscopy (TEM).

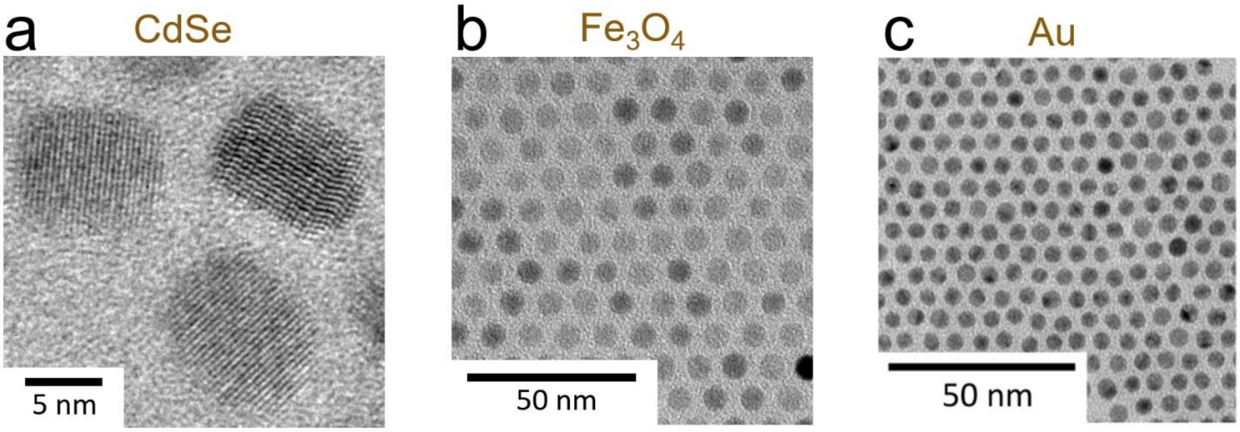

Figure 1-2: TEM micrographs of selected nanocrystals synthesized by colloidal techniques. (a) oblate spheroids of wurtzite CdSe. This image is taken at high magnification revealing individual atomic planes that make up the nanostructures. Crystalline defects in the form of dislocation planes are visible in the upper right nanoparticle. (b) Spherical magnetite particles with an average diameter of 8 nm stabilized by oleic acid. (c) Au nanoparticles with a 5 nm average diameter capped with dodecanethiol.

1.2. Electronic excitations in materials with reduced dimensions: The role of quantum confinement

A key factor in the utility of bottom-up synthetic methods for engineering new functional materials is the ability to exploit size dependence of physical properties of materials that emerges at the nanoscale. Perturbation of the bulk electronic density of states (DOS) due to quantum confinement[20] at the nanoscale represents one the most important and well-studied size and material dependent effects. When a particle of dielectric material is shrunk down to the nanoscale, it enters a regime where the energy of the lowest electronic excitation becomes size dependent. To understand this phenomenon intuitively, consider the most familiar example of a bound state between two particles with opposite charge, the hydrogen atom. In a single atom of hydrogen, the "hole" is a proton rather than a quasiparticle, and correspondingly has a much larger mass of 1836 m_e. Additionally, the medium that separates the electron and proton is simply vacuum, and there is no polarizable matter between them to screen their mutual Columbic interaction. Contrast this case to that of the semiconducting material CdSe, where the excited state consists of quasiparticles with "effective masses" of 0.13 and 0.45 for the electron and hole respectively. Here, the Columbic interaction between the positive and negatively charged particles is screened by the polarizability of the atoms that make up the CdSe lattice. The result is that whereas the bound state between an electron and proton in vacuum has a Bohr diameter of 0.11 nm, the exciton in CdSe is enlarged by two orders of magnitude and has a Bohr diameter of 10.8 nm. The values in Table 1-1 summarize the differences. Now, suppose a particle of CdSe is significantly smaller in diameter than 10.8 nm, for example consider a 5 nm diameter sphere of CdSe. When an incident photon is used to pump the particle into an excited state, the Coulombically bound electron and hole will not access the same equilibrium separation as in the bulk case where the Bohr diameter of the state was 10.8 nm.

CdSe:	H:
E_g: 1.75 eV (708 nm)	E_g: N/A
m_e: 0.13 m_h: 0.45	m_e: 1 m_h: 1836
ε: 10.2	ε: 1
Bohr Diameter: 10.8 nm	Bohr Diameter: 0.11 nm

Table 1-1: Parameters relevant to the Bohr exciton diameter in CdSe compared to the familiar example of a hydrogen atom.

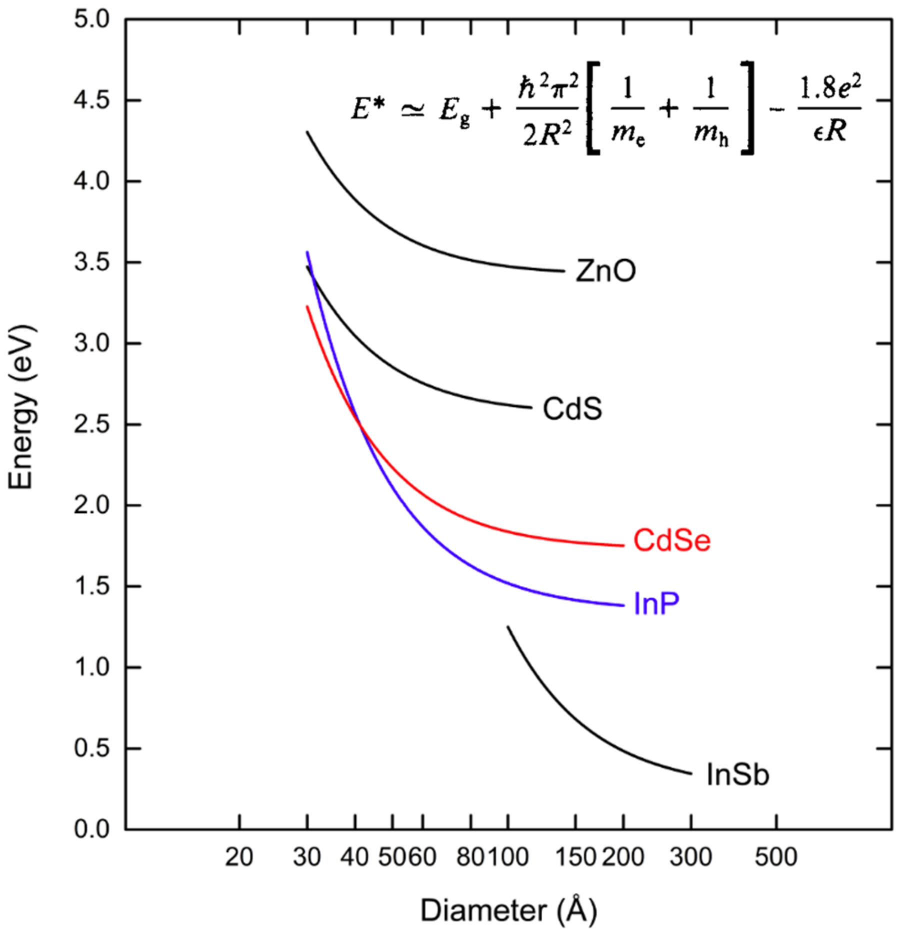

Figure 1-3: Plot of the relationship between particle diameter and energy of the first electronic excitation "bandgap energy", for selected semiconducting materials. The traces are based on confinement effects computed by the "Effective Mass Model[21,22]" (EMA), plot adapted from (21).

Because the electron and hole are each confined within the 5 nm dimension of the particle, the new confined excited state will be unable to relax to the bulk equilibrium electron-hole distance. Hence, the most relaxed possible confined excited state will be more energetic than for bulk material. This phenomenon manifests itself as a size-dependence of the bandgap of semiconductor nanoparticles (Figure 1-3). The traces plotted for two materials, InP and CdSe, are in color to highlight their relative importance. For these semiconductors, the materials parameters allow the confinement effect to tune energy gap across the entire visible spectrum (Figure 1-4) at a particle size range from 2-7 nm, a window that is easily accessible by colloidal semiconductor growth techniques.

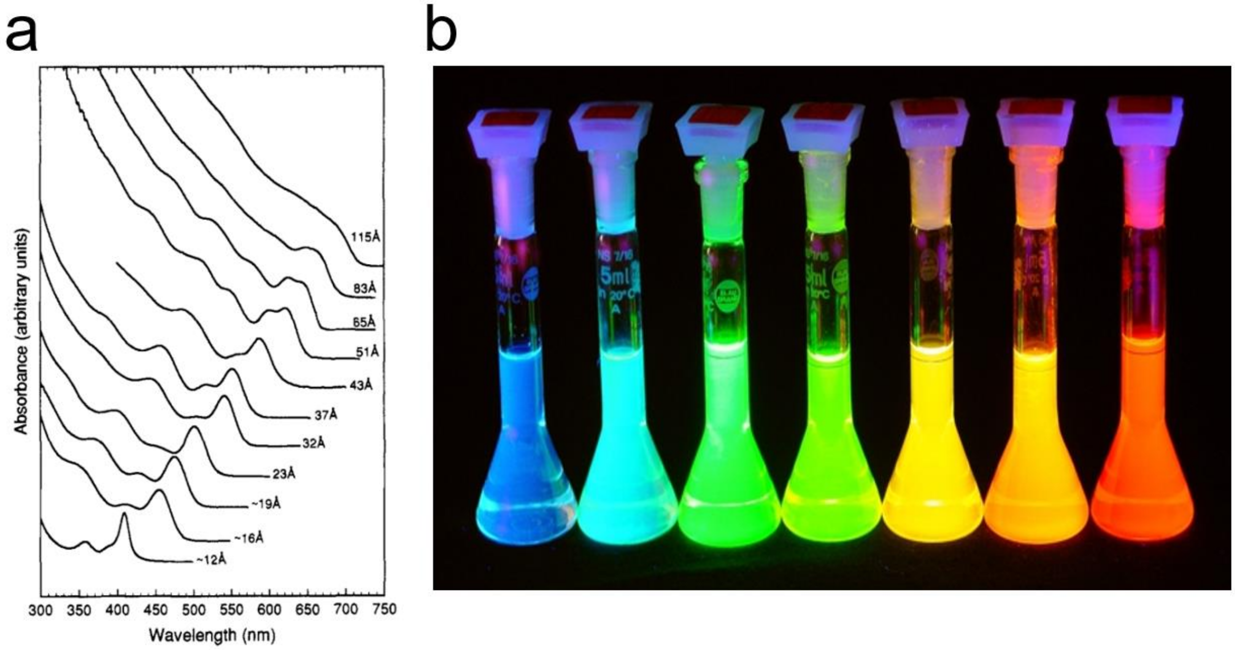

Figure 1-4: a. Size-dependent absorption spectra[23] of colloidal CdSe nanocrystals with diameters ranging from 11.5 nm (top spectrum) to 1.2 nm (bottom spectrum) **b.** Samples of CdSe colloids dispersed in non-polar solvent and illuminated by an ultraviolet light source[24]. The particles emit light with photon energy corresponding to that of their lowest available electronic excitation. Particle size for a given vial increases progressively moving to the right making energy of emission progressively decrease. Content of panels **a**[23] and **b**[24] reproduced with permission.

1.3. Application of semiconductor quantum dots: figures of merit for quantum dot light emitters and the role of structural and chemical homogeneity

Colloidal nanoparticles composed of semiconductor materials in the quantum confinement regime, or "colloidal quantum dots" show a great potential for solving problems related to light emitting devices. These nanostructures act as devices that convert an electrical or optical energetic input into emitted light at a wavelength that is continuously tunable. Recent technology development has seen quantum dot emitters applied to cutting edge displays[25], employed as phosphor down-converters for white LEDs[26], and as the active layer of electroluminescent devices[13,27,28]. Over the course of research and development into practical deployment of colloidal quantum dots for lighting, three major parameters have been identified as being key to defining

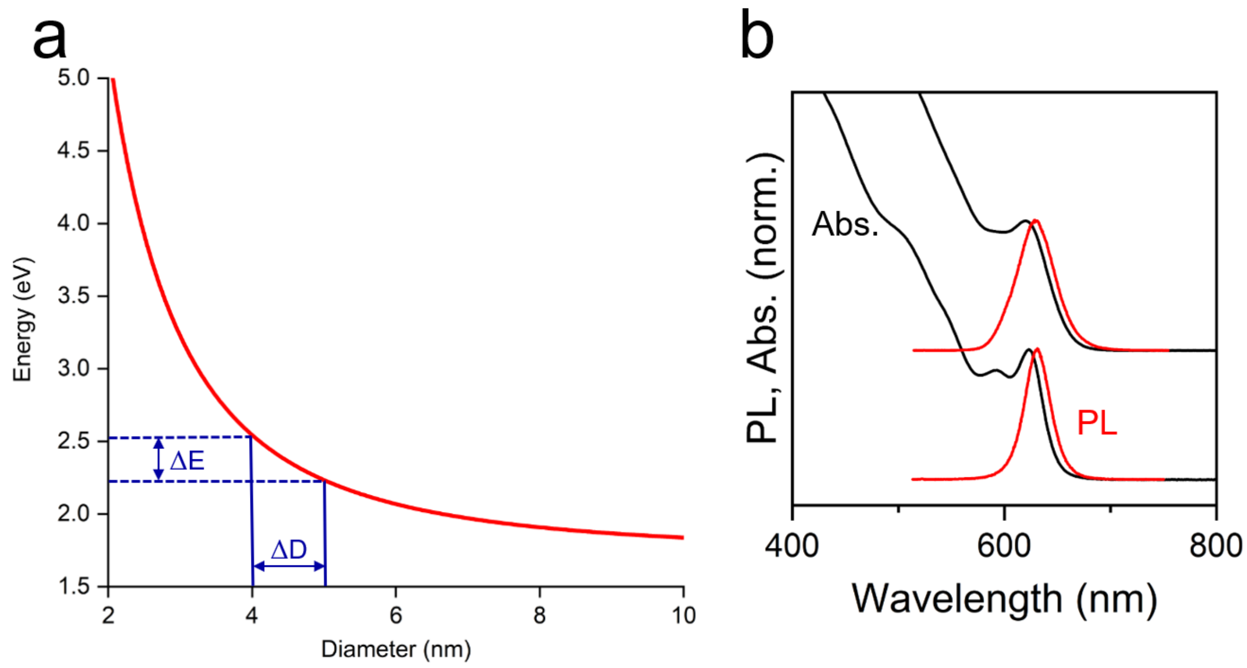

Figure 1-5: a. EMA size-bandgap relation for a prototypical semiconductor material with annotations indicating the interval of confinement energies ΔE that arises from a given interval in particle diameter, ΔD. **b.** A plot of absorbance (black) and photoluminescence (red) of two colloids of CdSe quantum dots, offset for clarity. The sample represented by upper traces contains a broader range of particle sizes and a concomitantly broadened range of first exciton energies.

optimum performance. These include chemical stability, energy conversion efficiency, and spectral purity of the emitted light. The last of these, spectral color purity, is related to the inverse of the width of the emission band. Narrow emitting ensembles of quantum dots are desirable for their ability to produce pure, saturated colors. A major source of spectral line broadening in an ensemble of quantum dots arises as a result of inhomogeneous distribution of sizes. With a distribution of particle diameters there will be a distribution of energy gaps (Figure 1-5a). The result is broadened spectral features at the ensemble level, Figure 1-5b shows the effect in a real system with two colloids of CdSe at differing levels of size dispersity. The size distribution obtained from as-synthesized particles can be addressed by synthetic optimizations[29] to control relative rates of precursor nucleation and particle growth.

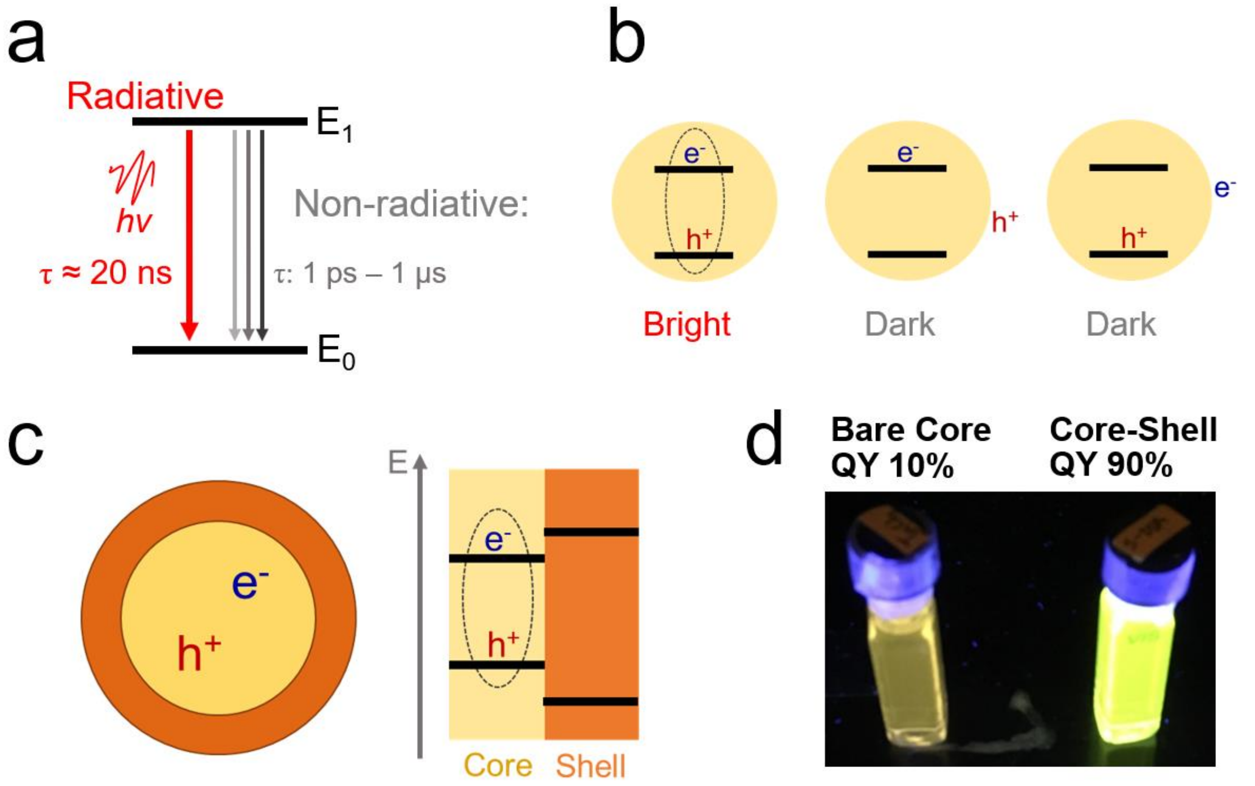

Figure 1-6: Charge trapping and surface passivation of colloidal quantum dots. a. State diagram depicting a competition between radiative recombination emitting a photon, and a manifold of non-radiative processes that occur over a wide range of timescales. **b.** Cartoon diagram comparing the "bright" excitonic state with delocalized bandedge carriers to two examples of "dark" states whereby localization of either an electron or a hole on the nanocrystal surface leads to subsequent non-radiative recombination. **c.** A diagram depicting a method for preventing surface localized charge carriers by shelling a semiconductor quantum dot with a layer of material with a wider bandgap. d. A photograph comparing photoluminescence intensity of a colloid of bare quantum dots to one of shelled quantum dots. Both samples are pumped by the same UV light source, the shelled particles exhibit a significantly brighter emission due to a relatively higher chance of radiative relaxation.

Sources of spectral line broadening at the single particle level have also been investigated[30,31]. These works have shown that exciton-phonon coupling strength plays an important role in linewidths that are observed at the single particle level and that this parameter is synthetically controllable by engineering emissive heterostructures where spatial separation between the electron and hole is minimized. Previous research efforts[32-34] investigating the luminescence of ternary copper chalcogenide nanocrystals demonstrated the effect of carrier localization and increased exciton-phonon coupling in a system where emission involves a state with a fully localized charge carrier. The deleterious effects of carrier localization on linewidth then motivate future work toward understanding what types of structural motifs lead to emission mechanisms involving localized electronic states.

Carrier localization also plays a key role in determining excitation energy to emitted light conversion efficiency of a quantum dot material system. Frequently, states with surface localized charge carriers are responsible for introducing non-radiative relaxation pathways (Figure 1-6a,b) that compete with emission and result in unwanted dissipation of input energy as heat[35]. Passivation strategies such as shelling a quantum dot material with a layer of another semiconducting material with a wider bandgap (Figure 1-6c) have commonly been employed to

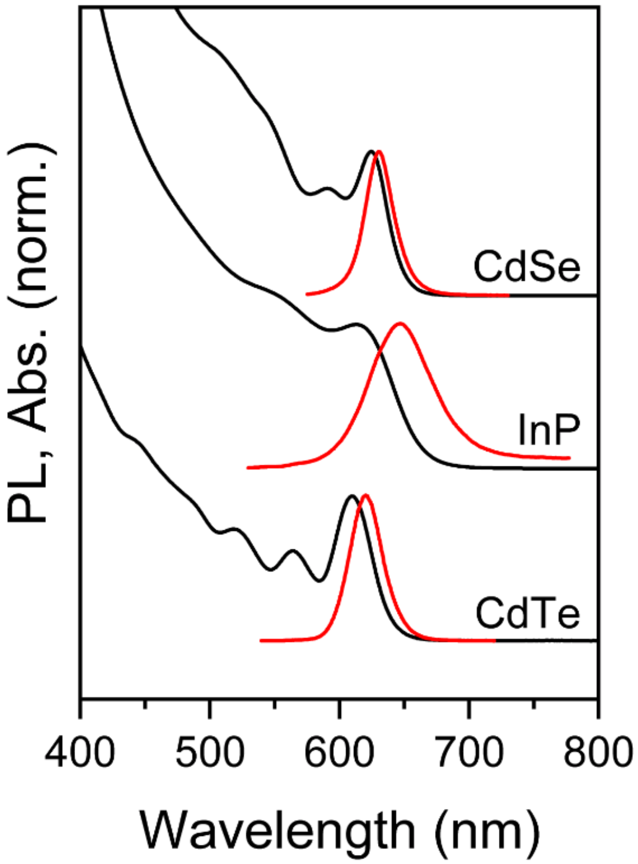

Figure 1-7: Absorption (red) and PL (red) spectra of typical samples of CdSe, InP, and CdTe quantum dots offset for clarity. Spectral features of the InP colloid are significantly broader.

minimize the effect of surface related trap states, “passivate the surface”, and lead to far higher radiative efficiencies (Figure 1-6d). In this work, I examine the relationship between passivation chemistry of InP colloidal quantum dots and provide evidence for a role of hole localization in broadening the ensemble photoluminescence linewidths. I identify a correlation between redshifted emission spectra and anomalous broadening of the excitation spectra of luminescent InP colloids, suggesting a trap-associated emission pathway in highly-emissive core-shell quantum dots. Time-resolved pump-probe experiments find that electrons are largely untrapped on photoluminescence relevant timescales pointing to emission from recombination of localized holes with free electrons. These localized hole states near the valence band edge are hypothesized to arise from incomplete surface passivation and structural disorder associated with lattice defects. I confirm the presence and effect of lattice disorder by x-ray absorption spectroscopy and Raman scattering measurements. Participation of localized electronic states that are associated with various classes of lattice defects gives rise to phonon-coupled defect related emission. With these findings, I seek to explain the origins of the persistently broad emission spectra of colloidal InP quantum dots and suggest future strategies to narrow ensemble emission lines comparable to what is observed for the canonical CdSe quantum dot materials system.

1.4. Incorporation of colloidal nanomaterials into solid films or composites: the relation between interparticle forces and packing

After a colloidal nanomaterial system aimed at a particular application is understood and optimized in terms of particle growth protocol, passivation, and surface chemistry, the nest step toward realizing functionality is incorporation of the nanocrystals into a desired structure. For catalysis, this may mean anchoring particles to an oxide scaffold[36], for quantum dot phosphor down converters, embedding particles into siloxane resins[37]. For all various schemes for building functional materials using colloidal nanocrystal units, an understanding of interparticle forces is crucial. Recent studies[38,39] along these lines have highlighted the role of ligand entropy in stabilization of colloidal particles and shown that nanocrystal inks can be formulated at very high weight loading when ligands are optimized as entropic springs to provide strong short range repulsive forces to stabilize particles and prevent aggregation. For many prospective applications of nanocrystal derived materials, density of nanocrystal packing is a critical parameter. The ultimate densified nanocrystal solid will take the form of a superlattice where average nearest neighbor interparticle distances have been minimized and translational order appears at the super-crystalline level. Such a morphology is readily achievable because the ordered and densest packing represents the global thermodynamic minimum. An ensemble of colloidal nanocrystals in a

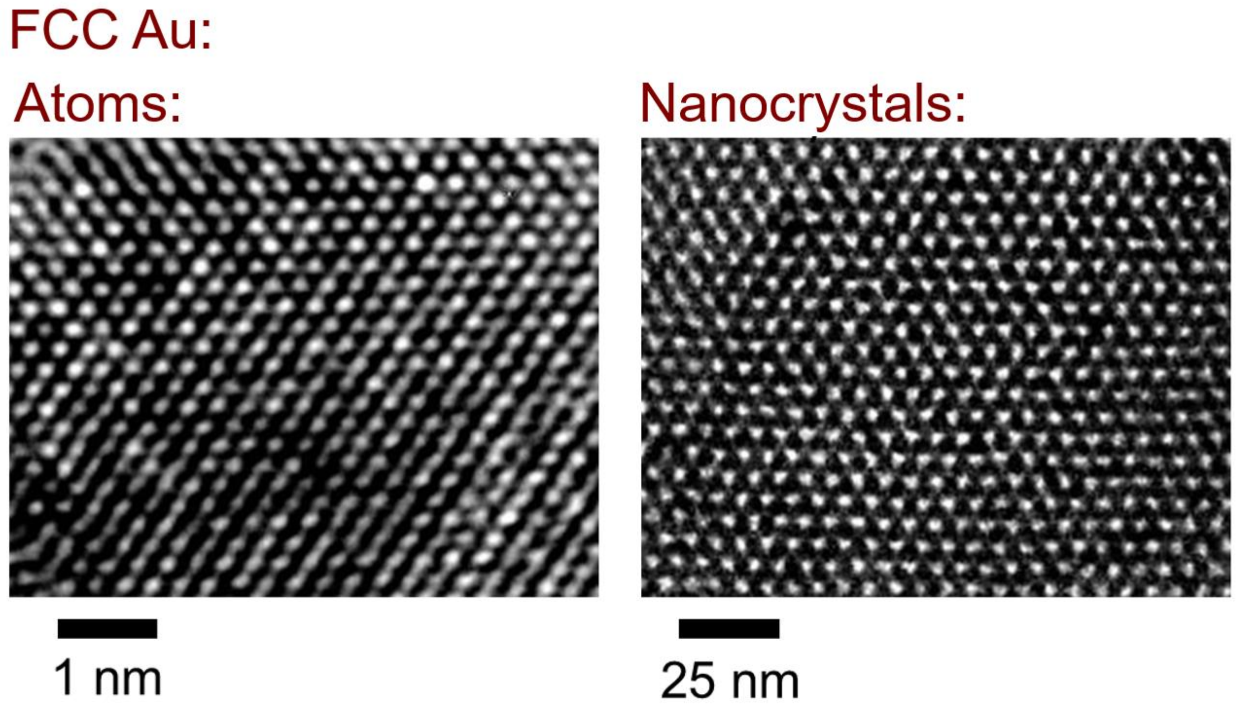

Figure 1-8: Translational symmetry in energetic minima. On the left, a bright field TEM image showing a lattice of FCC gold atoms viewed from the 111 direction. On the right, a bright field TEM image showing an FCC superlattice of Au nanocrystals, 5 nm in diameter.

confined volume of solvent will order spontaneously in an arrangement that minimizes free energy, $F = U - TS$[40] by maximizing both free volume entropy by more efficient space filling and configurational entropy at the per particle level by preventing jamming that would restrict particle motion. Figure 1-8 summarizes the ordered dense packing that can be achieved for 5 nm diameter colloidal Au nanocrystals and compares that system to one of Au atoms. Both the atoms and nanocrystals adopt ordered, close-packed FCC structures in their energetic minima. Energetics of nearest neighbor interaction are different in each case, but the rule of minimizing internal energy by minimizing average inter-unit spacings yields the same lattice arrangement in each case.

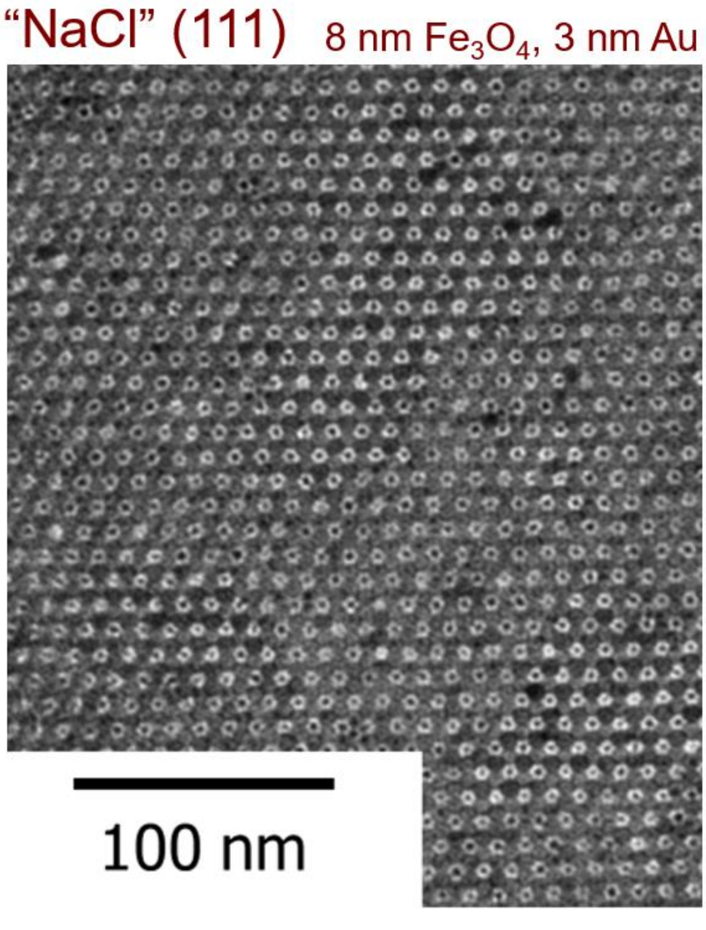

Figure 1-9: TEM image of a binary nanoparticle superlattice. The supercrystal is composed of Fe_3O_4 and Au nanocrystals, 8 nm and 3 nm in diameter respectively. The two populations of nanocrystals co-crystallize into an analogue of the NaCl lattice where Fe_3O_4 particles act as Cl^- ions while the smaller Au particles represent Na^+ cations.

Entropy driven self-assembly of colloidal nanocrystals that are sterically stabilized by long chain organic ligands has been thoroughly explored[41,42] as a way of building ordered, dense, and intricate structures from colloidal nanocrystals. Work on assembly of multicomponent systems[43-45] has succeeded in growing globally energy minimized structures producing binary nanoparticle superlattices crystallizing in a rich array of structural motifs. A related body of work[46-51] has sought to understand the physics that underpin the phase space that is accessed in these experiments. Research along the lines multicomponent nanocrystal assembly has produced the purest examples so far of employing nanoscale building blocks for ground up fabrication of totally novel materials. Figure 1-9 shows a TEM micrograph of an example of a binary phase where Fe_3O_4 and Au nanoparticles have co-crystallized into with relative positions that are the analogue of the sites in a NaCl crystal lattice. Despite the enormous success of colloidal self-assembly using organically capped nanoparticles dispersed in non-polar media, the technique has encountered fundamental limitations that have stifled attempts to take the field forward. The same organic capping ligands that provide short range repulsive forces and allow assembly into minimum energy structures to occur, also act as insulating barriers in the final solid. In fact, due to the high surface area to volume ratio of nanoscale particles, the organic ligands can compose a significant volume fraction of a total nanocrystal solid. For a close packed FCC superlattice of 5 nm diameter Au particles with dodecanethiol ligands, small-angle x-ray scattering experiments found an average nearest neighbor surface to surface distance between Au particles to be 2.2 nm (See Ch. 4, 5 for details). Considering an FCC lattice of 5 nm Au spheres with a 1.1 nm thick shell of organics, the total volume occupied by Au is only 25%. The large relative volume of organics places structures grown from sterically stabilized colloidal nanoparticles firmly on the insulator side of a metal-insulator transition and weak interparticle coupling undermines the ability of colloidal self-assembly to produce materials with novel properties that emerge from collective interactions between their constituent units.

1.5. Electronic coupling between nanocrystal units in the solid state: Ligand exchange and electrostatic stabilization

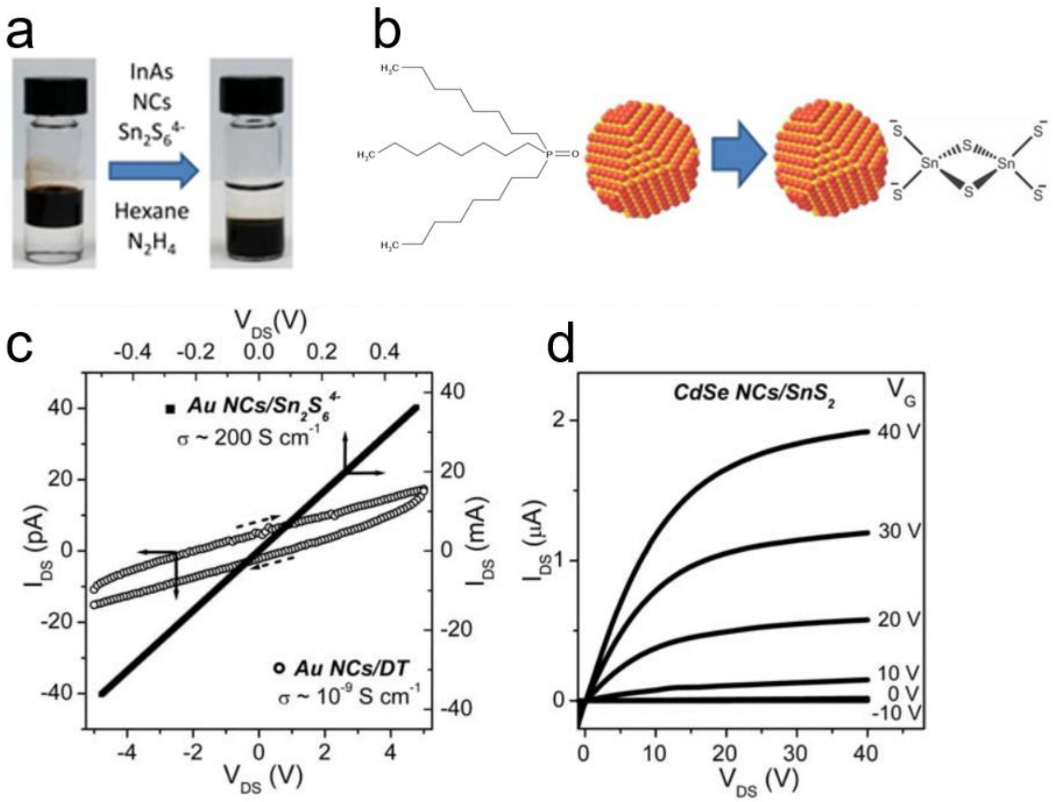

Figure 1-10: Ligand exchange from native bulky organics to compact inorganic anions. a. Photographs showing the ligand exchange process of InAs nanocrystals from tri-n-octylphosphine oxide (TOPO) capped and dispersed in hexane to $Sn_2S_6^{4-}$ capped and transferred to the lower hydrazine phase. **b.** A schematic depicting the change from a TOPO covered surface to a negatively charged, $Sn_2S_6^{4-}$ capped surface. **c.** Plot comparing IV curves for Au nanocrystal thin films with dodecanethiol (DT) and $Sn_2S_6^{4-}$ ligands. The inorganically capped Au particles show increased conductivity by 11 orders of magnitude. **d.** Transfer curves for a field effect transistor made from CdSe nanocrystals capped with $Sn_2S_6^{4-}$ ligands. Figure adapted with permission from content published in ([52]).

To date, successful application of colloidal nanocrystal-based materials to problems that require dense packed and electronically coupled nanocrystal units has made use of post-synthetic ligand exchange chemistries to modify the surfaces of as-synthesized colloidal materials and allow for neighboring particles to communicate electronically. Efforts in quantum dot photovoltaics[53,54], LEDs[55], and transistors[52,56,57] have all effectively made use of this strategy. Additionally, ligand exchanged nanocrystals have proven to be very effective solution-based precursors to thermally sintered dense films of bulk semiconductor material[15,58,59], in comparison organic capped nanocrystal solids are much more difficult to sinter[60]. Figure 1-10a,b summarizes an example of a solution-phase ligand exchange process that takes InAs quantum dots capped with bulky tri-n-octylphosphine ligands and ligand exchanges them for the anionic species $Sn_2S_6^{4-}$. The ligand exchanged particles disperse in polar media as “salts” where the nanocrystals acquire a net negative charge from the surface bound $Sn_2S_6^{4-}$ ligands and act as giant polyanions with charge balanced by free monovalent cationic species such as H^+ or Na^+. These inorganically capped colloids in polar solvents can then act as inks to deposit thin-films of electronically coupled metal (Figure 1-10c) or semiconductor (Figure 1-10d) nanocrystals. However, employing this strategy comes at a price: the compact inorganic ligands that allow for strong coupling and small minimum interparticle spacings due to their small size also tend to induce “sticky” pair potentials at short range. This leads to nanocrystal solids obtained from charge stabilized nanocrystals commonly exhibiting[61] low packing density and open, porous, fractal structures. Thus far, the trade-off has been positive and the benefits of inorganic capping strategies have outweighed these costs. The problem remains of how to understand interparticle potentials between charge stabilized colloidal particles in order to engineer systems that can achieve the same energy minimized dense packings that are observed for particles stabilized with long, insulating, surfactant molecules.

1.6. Demonstration of simultaneous order and strong electronic coupling: Assembly of charge-stabilized colloidal particles into supercrystalline solids

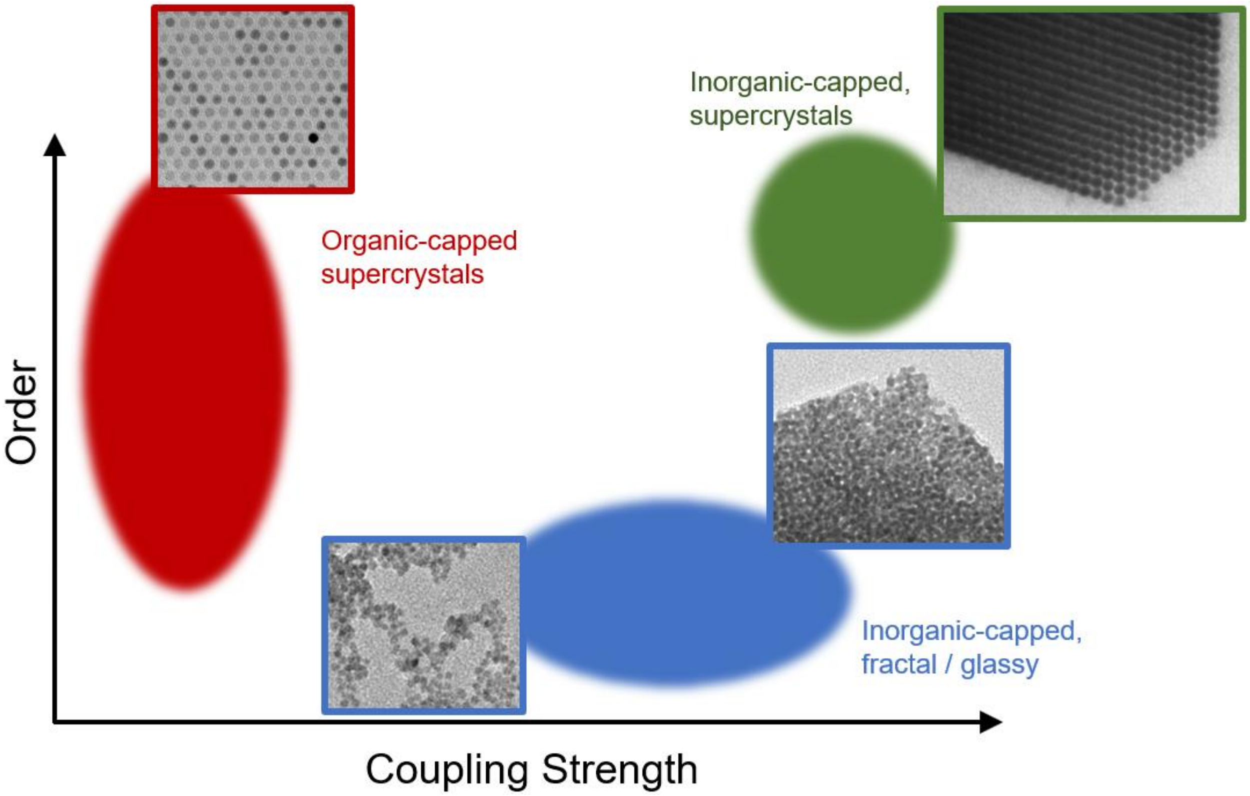

Figure 1-11: A map of the relationship between order and electronic coupling strength in nanocrystal solids. Supercrystals grown from charge stabilized, inorganically capped nanocrystals achieve an unprecedented combination of strong electronic coupling and maximally dense, ordered packing. TEM micrographs show images of examples of the three highlighted classes of material.

In the latter part of this work, Chapters 4 and 5, I discuss an in-depth study of the relation between surface chemistry of charge-stabilized colloids, interparticle interactions, and ultimate achievable densification and ordering. I present a novel method for self-assembly of colloidal metal nanoparticles that are stabilized in polar solvent by compact chalcogenidometallate (ChM) anions. Flocculation of such colloids by controlled addition of excess ChM salts results in loss of colloidal stability and growth of self-assembled superlattices. Structural characterization of the resulting supercrystalline material reveals cleanly faceted structures with micron scale edge lengths and a high degree of internal order. The ChM ligands are found to decompose and cross-link, forming an amorphous glassy metal chalcogenide matrix that fills the interstices of the ordered nanocrystal array. I seek to confirm by optical and electronic characterization that there is strong coupling between neighboring nanocrystal units and find evidence of metallic transport with DC conductivities that are within a factor of 10 from those of bulk metals. I further study the mechanism of the crystallization process that leads to formation of our supercrystals and find that the ordered phase appears by particles first agglomerating into a dense amorphous phase, and then subsequently rearranging into an ordered lattice. This assembly mechanism is found to be general for metal nanoparticles with diameters ranging from 4 – 10 nm flocculated by a wide variety of ChM salts in polar media. Experimental evidence points to a unique propensity for metallic, as opposed to dielectric, nanoparticles to assemble due to polarization effects whereby attractive image charges allow for a denser cloud of associated ChM anions to form around them. This effect in turn provides strong short-range repulsive forces that prevent jamming during the early stages of the assembly process. Simulations confirm the effects of particle polarizability and predict image-charge induced ion structuring and repulsive potentials that are exactly in line with observation.

1.7. Chapter 1 bibliography

(1) Talapin, D. V. *ACS Nano* **2008**, *2*, 1097.

(2) Kovalenko, M. V.; Manna, L.; Cabot, A.; Hens, Z.; Talapin, D. V.; Kagan, C. R.; Klimov, V. I.; Rogach, A. L.; Reiss, P.; Milliron, D. J.; Guyot-Sionnnest, P.; Konstantatos, G.; Parak, W. J.; Hyeon, T.; Korgel, B. A.; Murray, C. B.; Heiss, W. *ACS Nano* **2015**, *9*, 1012.

(3) Yin, Y.; Alivisatos, A. P. *Nature* **2005**, *437*, 664.

(4) Nag, A.; Zhang, H.; Janke, E.; Talapin Dmitri, V. In *Zeitschrift für Physikalische Chemie* 2015; Vol. 229, p 85.

(5) Talapin, D. V.; Lee, J.-S.; Kovalenko, M. V.; Shevchenko, E. V. *Chemical Reviews* **2010**, *110*, 389.

(6) Ruditskiy, A.; Peng, H.-C.; Xia, Y. *Annual Review of Chemical and Biomolecular Engineering* **2016**, *7*, 327.

(7) Cargnello, M.; Doan-Nguyen, V. V. T.; Gordon, T. R.; Diaz, R. E.; Stach, E. A.; Gorte, R. J.; Fornasiero, P.; Murray, C. B. *Science* **2013**, *341*, 771.

(8) Sun, S.; Murray, C. B.; Weller, D.; Folks, L.; Moser, A. *Science* **2000**, *287*, 1989.

(9) Shen, Z.; Wu, A.; Chen, X. *Molecular Pharmaceutics* **2017**, *14*, 1352.

(10) Wang, A. Z.; Langer, R.; Farokhzad, O. C. *Annual Review of Medicine* **2012**, *63*, 185.

(11) Kim, B. H.; Lee, N.; Kim, H.; An, K.; Park, Y. I.; Choi, Y.; Shin, K.; Lee, Y.; Kwon, S. G.; Na, H. B.; Park, J.-G.; Ahn, T.-Y.; Kim, Y.-W.; Moon, W. K.; Choi, S. H.; Hyeon, T. *Journal of the American Chemical Society* **2011**, *133*, 12624.

(12) Erdem, T.; Demir Hilmi, V. In *Nanophotonics* 2016; Vol. 5, p 74.

(13) Choi, M. K.; Yang, J.; Hyeon, T.; Kim, D.-H. *npj Flexible Electronics* **2018**, *2*, 10.

(14) Kagan, C. R. *Chemical Society Reviews* **2019**, *48*, 1626.

(15) Dolzhnikov, D. S.; Zhang, H.; Jang, J.; Son, J. S.; Panthani, M. G.; Shibata, T.; Chattopadhyay, S.; Talapin, D. V. *Science* **2015**, *347*, 425.

(16) Pu, Y.; Cai, F.; Wang, D.; Wang, J.-X.; Chen, J.-F. *Industrial & Engineering Chemistry Research* **2018**, *57*, 1790.

(17) Singamaneni, S.; Bliznyuk, V. N.; Binek, C.; Tsymbal, E. Y. *Journal of Materials Chemistry* **2011**, *21*, 16819.

(18) He, M.; Protesescu, L.; Caputo, R.; Krumeich, F.; Kovalenko, M. V. *Chemistry of Materials* **2015**, *27*, 635.

(19) Peng, S.; Lee, Y.; Wang, C.; Yin, H.; Dai, S.; Sun, S. *Nano Research* **2008**, *1*, 229.

(20) Bawendi, M. G.; Steigerwald, M. L.; Brus, L. E. *Annual Review of Physical Chemistry* **1990**, *41*, 477.

(21) Brus, L. E. *The Journal of Chemical Physics* **1984**, *80*, 4403.

(22) Brus, L. *The Journal of Physical Chemistry* **1986**, *90*, 2555.

(23) Murray, C. B.; Norris, D. J.; Bawendi, M. G. *Journal of the American Chemical Society* **1993**, *115*, 8706.

(24) Rogach, A. L.; Talapin, D. V.; Shevchenko, E. V.; Kornowski, A.; Haase, M.; Weller, H. *Advanced Functional Materials* **2002**, *12*, 653.

(25) Jang, E.; Jun, S.; Jang, H.; Lim, J.; Kim, B.; Kim, Y. *Advanced Materials* **2010**, *22*, 3076.

(26) Shimizu, K. T.; Böhmer, M.; Estrada, D.; Gangwal, S.; Grabowski, S.; Bechtel, H.; Kang, E.; Vampola, K. J.; Chamberlin, D.; Shchekin, O. B.; Bhardwaj, J. *Photon. Res.* **2017**, *5*, A1.

(27) Shirasaki, Y.; Supran, G. J.; Bawendi, M. G.; Bulović, V. *Nature Photonics* **2012**, *7*, 13.

(28) Wood, V.; Bulović, V. *Nano Reviews* **2010**, *1*, 5202.

(29) Peng, X.; Wickham, J.; Alivisatos, A. P. *Journal of the American Chemical Society* **1998**, *120*, 5343.

(30) Cui, J.; Beyler, A. P.; Marshall, L. F.; Chen, O.; Harris, D. K.; Wanger, D. D.; Brokmann, X.; Bawendi, M. G. *Nature Chemistry* **2013**, *5*, 602.

(31) Cui, J.; Beyler, A. P.; Coropceanu, I.; Cleary, L.; Avila, T. R.; Chen, Y.; Cordero, J. M.; Heathcote, S. L.; Harris, D. K.; Chen, O.; Cao, J.; Bawendi, M. G. *Nano Letters* **2016**, *16*, 289.

(32) Knowles, K. E.; Nelson, H. D.; Kilburn, T. B.; Gamelin, D. R. *Journal of the American Chemical Society* **2015**, *137*, 13138.

(33) Whitham, P. J.; Marchioro, A.; Knowles, K. E.; Kilburn, T. B.; Reid, P. J.; Gamelin, D. R. *The Journal of Physical Chemistry C* **2016**, *120*, 17136.

(34) Nelson, H. D.; Li, X.; Gamelin, D. R. *The Journal of Physical Chemistry C* **2016**, *120*, 5714.

(35) Jang, Y.; Shapiro, A.; Isarov, M.; Rubin-Brusilovski, A.; Safran, A.; Budniak, A. K.; Horani, F.; Dehnel, J.; Sashchiuk, A.; Lifshitz, E. *Chemical Communications* **2017**, *53*, 1002.

(36) Cargnello, M. *Chemistry of Materials* **2019**, *31*, 576.

(37) Kim, H. Y.; Yoon, D.-E.; Jang, J.; Lee, D.; Choi, G.-M.; Chang, J. H.; Lee, J. Y.; Lee, D. C.; Bae, B.-S. *Journal of the American Chemical Society* **2016**, *138*, 16478.

(38) Yang, Y.; Qin, H.; Jiang, M.; Lin, L.; Fu, T.; Dai, X.; Zhang, Z.; Niu, Y.; Cao, H.; Jin, Y.; Zhao, F.; Peng, X. *Nano Letters* **2016**, *16*, 2133.

(39) Zhou, J.; Zhu, M.; Meng, R.; Qin, H.; Peng, X. *Journal of the American Chemical Society* **2017**, *139*, 16556.

(40) Frenkel, D. *Physica A: Statistical Mechanics and its Applications* **1999**, *263*, 26.

(41) Murray, C. B.; Kagan, C. R.; Bawendi, M. G. *Annual Review of Materials Science* **2000**, *30*, 545.

(42) Boles, M. A.; Engel, M.; Talapin, D. V. *Chemical Reviews* **2016**, *116*, 11220.

(43) Shevchenko, E. V.; Talapin, D. V.; Kotov, N. A.; O'Brien, S.; Murray, C. B. *Nature* **2006**, *439*, 55.

(44) Shevchenko, E. V.; Talapin, D. V.; Murray, C. B.; O'Brien, S. *Journal of the American Chemical Society* **2006**, *128*, 3620.

(45) Chen, Z.; O’Brien, S. *ACS Nano* **2008**, *2*, 1219.

(46) Boles, M. A.; Talapin, D. V. *Journal of the American Chemical Society* **2015**, *137*, 4494.

(47) Coropceanu, I.; Boles, M. A.; Talapin, D. V. *Journal of the American Chemical Society* **2019**, *141*, 5728.

(48) Waltmann, C.; Horst, N.; Travesset, A. *ACS Nano* **2017**, *11*, 11273.

(49) Cersonsky, R. K.; van Anders, G.; Dodd, P. M.; Glotzer, S. C. *Proceedings of the National Academy of Sciences* **2018**, *115*, 1439.

(50) Schapotschnikow, P.; Vlugt, T. J. H. *The Journal of Chemical Physics* **2009**, *131*, 124705.

(51) Landman, U.; Luedtke, W. D. *Faraday Discussions* **2004**, *125*, 1.

(52) Kovalenko, M. V.; Scheele, M.; Talapin, D. V. *Science* **2009**, *324*, 1417.

(53) Tang, J.; Kemp, K. W.; Hoogland, S.; Jeong, K. S.; Liu, H.; Levina, L.; Furukawa, M.; Wang, X.; Debnath, R.; Cha, D.; Chou, K. W.; Fischer, A.; Amassian, A.; Asbury, J. B.; Sargent, E. H. *Nature Materials* **2011**, *10*, 765.

(54) Luther, J. M.; Gao, J.; Lloyd, M. T.; Semonin, O. E.; Beard, M. C.; Nozik, A. J. *Advanced Materials* **2010**, *22*, 3704.

(55) Li, X.; Zhao, Y.-B.; Fan, F.; Levina, L.; Liu, M.; Quintero-Bermudez, R.; Gong, X.; Quan, L. N.; Fan, J.; Yang, Z.; Hoogland, S.; Voznyy, O.; Lu, Z.-H.; Sargent, E. H. *Nature Photonics* **2018**, *12*, 159.

(56) Jang, J.; Liu, W.; Son, J. S.; Talapin, D. V. *Nano Letters* **2014**, *14*, 653.

(57) Fafarman, A. T.; Koh, W.-k.; Diroll, B. T.; Kim, D. K.; Ko, D.-K.; Oh, S. J.; Ye, X.; Doan-Nguyen, V.; Crump, M. R.; Reifsnyder, D. C.; Murray, C. B.; Kagan, C. R. *Journal of the American Chemical Society* **2011**, *133*, 15753.

(58) Crisp, R. W.; Panthani, M. G.; Rance, W. L.; Duenow, J. N.; Parilla, P. A.; Callahan, R.; Dabney, M. S.; Berry, J. J.; Talapin, D. V.; Luther, J. M. *ACS Nano* **2014**, *8*, 9063.

(59) Panthani, M. G.; Kurley, J. M.; Crisp, R. W.; Dietz, T. C.; Ezzyat, T.; Luther, J. M.; Talapin, D. V. *Nano Letters* **2014**, *14*, 670.

(60) Zhang, H.; Kurley, J. M.; Russell, J. C.; Jang, J.; Talapin, D. V. *Journal of the American Chemical Society* **2016**, *138*, 7464.

(61) Lin, M. Y.; Lindsay, H. M.; Weitz, D. A.; Ball, R. C.; Klein, R.; Meakin, P. *Nature* **1989**, *339*, 360.

2. Luminescence and carrier dynamics in surface passivated InP emitters

Adapted with permission from E.M. Janke, N.E. Williams, C. She, D. Zherebetskyy, M.H. Hudson, L. Wang, D.J. Gosztola, R.D. Schaller, B.Lee, C.Sun, G.S. Engel, and D.V. Talapin, *"Origin of Broad Emission Spectra in InP Quantum Dots: Contributions from Structural and Electronic Disorder",* J. Am. Chem. Soc. 2018, 140, 46, 15791-15803. Copyright 2018 American Chemical Society.

2.1. Introduction

Colloidal semiconductor quantum dots have recently garnered significant interest for their potential as versatile light emitters. They offer the prospect of narrow photoluminescence linewidths and produce saturated colors when pumped with excitation light that may be delivered anywhere over a broad range of wavelengths shorter than that of the emission band. Additionally, the dependence of emission energy on the particle dimensions allows for easy tuning of emission color. So far, the best combination of desirable qualities including emission colors spanning the visible spectrum, photoluminescence quantum yield, narrow PL linewidth, and stability of emission has come from semiconductor materials that incorporate heavy metals such as cadmium[1] or lead.[2] Indium phosphide nanocrystals are a promising alternative that retains the spectral range of size tunable emission while expanding the scope of applicability of soluble semiconductor emitters. By avoiding the use of the toxic heavy metals Pb and Cd, InP based emitters are a viable solution to a broad range of consumer lighting and display technologies, and to biological labeling[3] and imaging applications which preclude the use of emitters that leach heavy metal ions.

While efforts to improve InP nanocrystal synthesis have resulted in reports of photoluminescence quantum yields of 80%[4], and 96%,[5] achievable color purity remains modest with persistently broad ensemble emission profiles. Investigations of single particle linewidths[6] have reported comparably narrow single particle emission from InP and CdSe though achievable ensemble emission from InP remains roughly double what is attained from CdSe. The question remains open as to why the synthetic optimization paradigm which has been so successful for materials like CdSe has encountered such difficulty with InP. A likely path to the answer lies in identifying what key characteristics of InP distinguish it from the CdSe model system. Recent studies[7-9] have focused on this aspect and have found strong evidence that the growth of colloidal InP proceeds via non-classical nucleation dominated mechanisms in contrast to CdSe. The result can lead to polydispersity of particle sizes and a corresponding broadening of ensemble emission.

2.2. Particle size distribution and ensemble emission linewidths

The effect of size distribution is particularly important for InP emitters compared to CdSe because the smaller diameter required for a given emission color puts InP colloids on a steeper region of the sizing curve where a given percent dispersity in size produces a larger range of confinement energies.

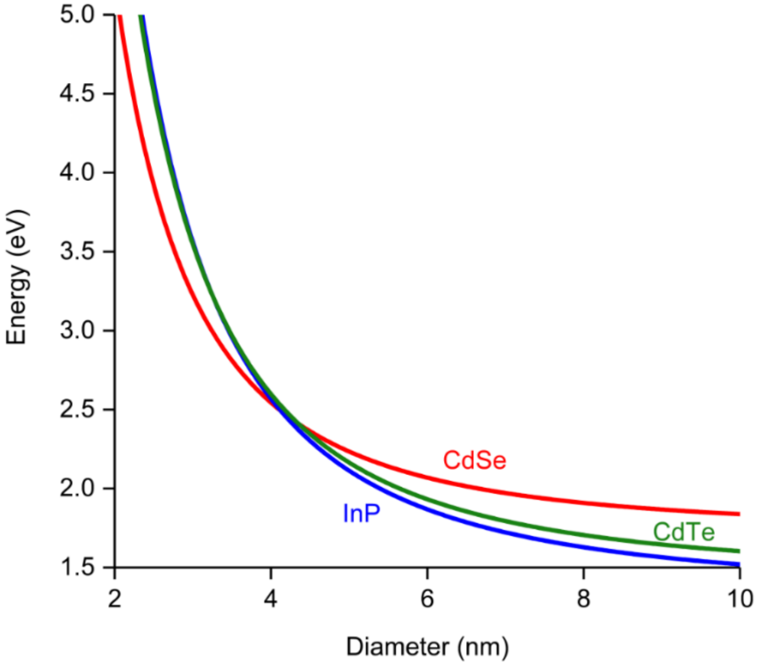

Figure 2-1: Confinement energies predicted by the effective mass model[10,11] for spherically confined excitons in CdSe, CdTe, and InP. There is a notable similarity in the optical gap – size relationship for CdTe and InP. Materials parameters were taken from ([12]).

This effect is summarized in Figure 2-1 and Figure 2-2:

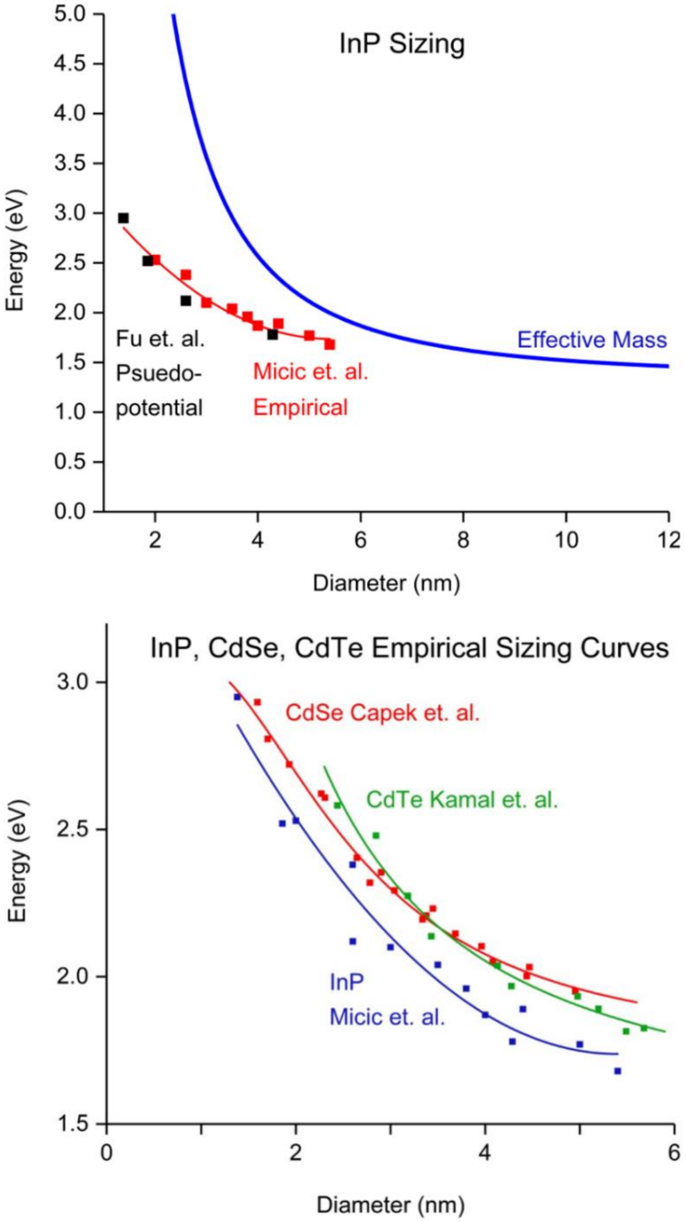

Figure 2-2: Top: A comparison of the simple effective mass model with an empirical sizing curve[13,14] and with results from atomistic pseudo-potential calculations[15] for InP nanocrystals. The effective mass model is known to overestimate confinement effects in the limit of small particle sizes. Bottom: Experimentally observed relations between particle diameter and first exciton energy for InP[13], CdSe[**16**], and CdTe[**17**].

Figure 2-1 shows a comparison of this relation for the common II-VI systems CdSe and CdTe, as well as for InP, calculated by the effective mass model. This simple method is known to overestimate confinement at small radii, shown in Figure 2-2. Nevertheless, the rough calculation identifies an important trend. It correctly makes the point that the sensitivity of confinement energy to particle size is similar for CdTe and InP, and greater than that of CdSe. Due to the lower bulk bandgap of InP as compared to CdSe, excitons in InP must be confined to smaller dimensions to reach technologically relevant emission energies. For a given percent dispersity in nanocrystal size, InP produces a larger range of confinement energies than CdSe (Table 2-1). This effect can indeed explain some part of the observed difficulty in obtaining narrow ensemble spectra features from InP colloids. However, the sizing curves for CdTe and InP are very similar and CdTe colloids can reliably be prepared with very narrow features in the ensemble emission and absorption without post-synthesis size fractionation.

Average diameter (nm)	Effective Mass Model broadening, ΔE (meV) at D ± 10%			Empirical sizing curve broadening ΔE (meV) at D ± 10%		
	CdSe	CdTe	InP	CdSe	CdTe	InP
3	642	891	931	180	239	199
4	355	495	519	129	161	154
5	223	313	328	88	119	66

Table 2-1: Energetic broadening calculations based on the effective mass model sizing curves and based on the empirical sizing curves that appear in Figure 2-2 for three materials at three average crystallite diameters. For example, for 5 nm CdSe, $\Delta E = E_g$ (4.5 nm) – E_g (5.5 nm).

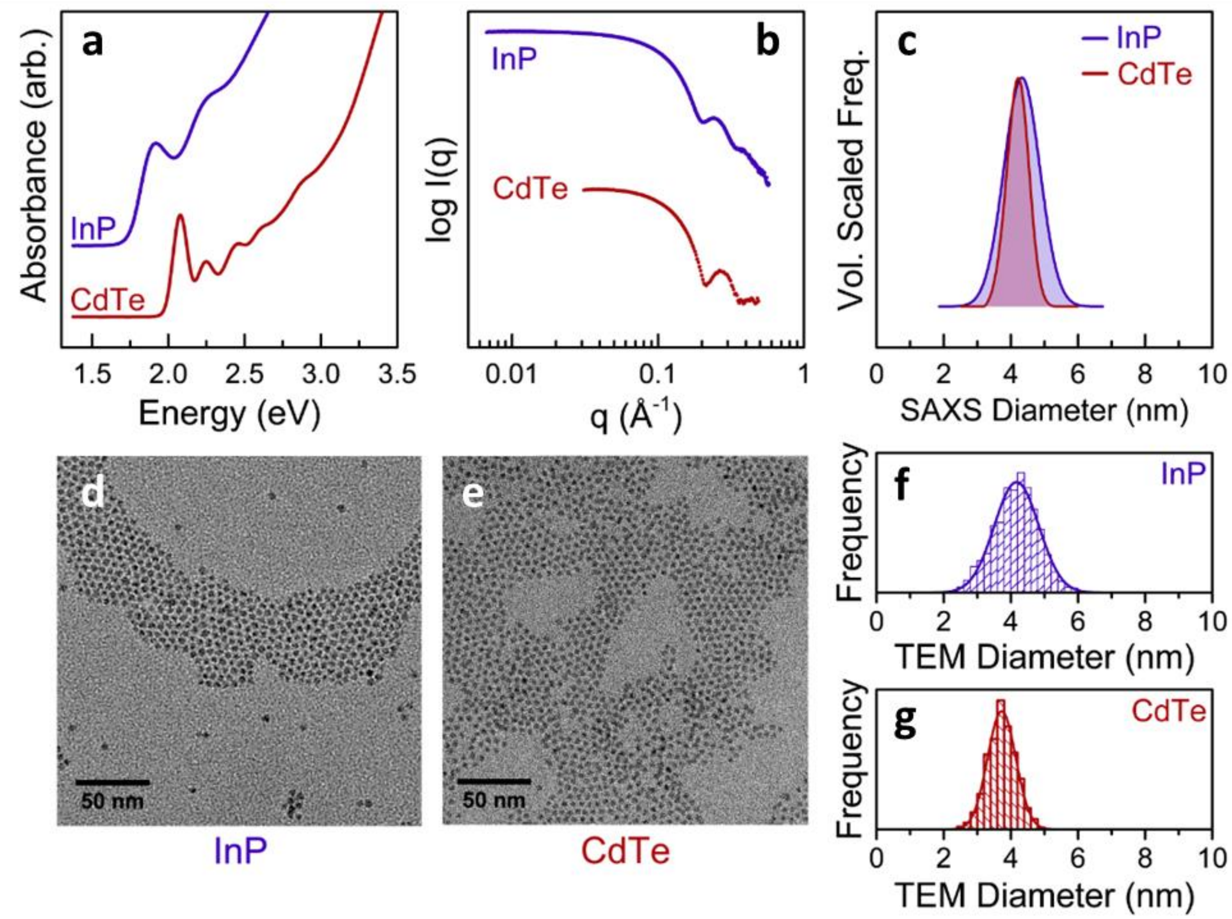

Figure 2-3: Size distribution analysis of InP and CdTe QDs a. Absorption spectra of ~4nm diameter CdTe and InP nanocrystals. b. SAXS patterns for each material measured as a colloid in toluene. c. Extracted volume scaled diameter distributions from SAXS. d.,e. TEM images of InP and CdTe. f.,g. Particle size distribution histograms extracted by TEM image analysis.

The characterization of a CdTe colloid in Figure 2-3 demonstrates that traditional colloidal synthesis methods are able to access the low levels of polydispersity required for narrow spectral linewidths despite the high sensitivity of CdTe to size distribution effects. Comparing the relative appearance of the spectra of the CdTe and InP data in this figure and the extracted size distributions, it is apparent that the boarder absorbance features of the InP sample are fully explained by its greater polydispersity. In this as-synthesized InP sample, there is no intrinsic line-broadening that would prevent further reduction of the ensemble spectral linewidth. This gives

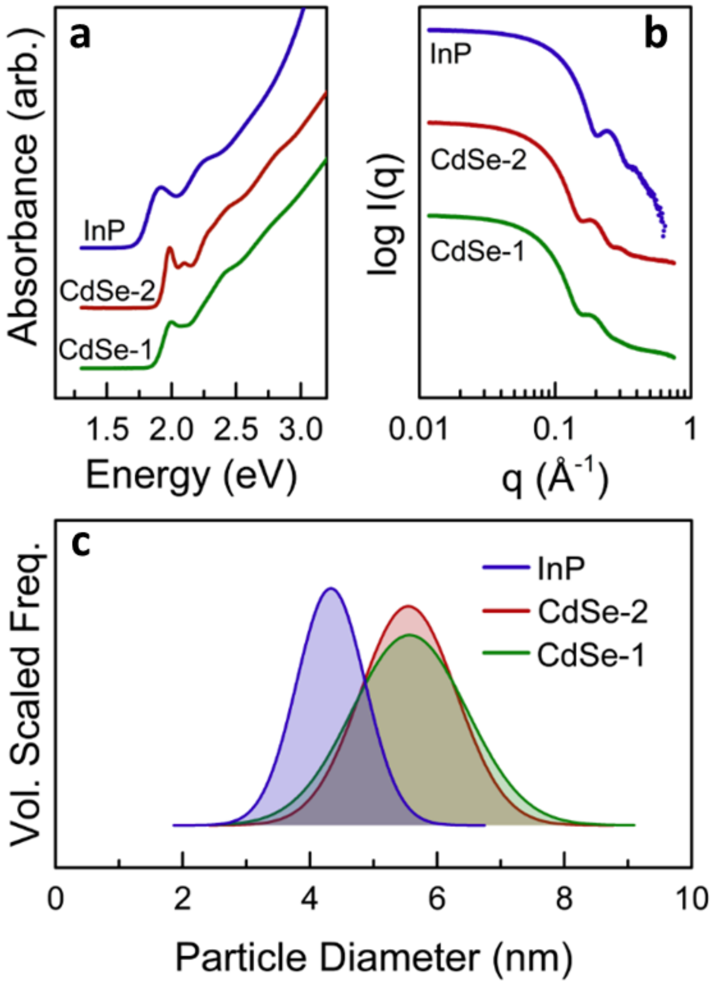

Figure 2-4: Small angle x-ray scattering for size distribution analysis. (a) Offset absorption spectra comparing CdSe of two different levels of polydispersity to a size selected sample of InP. (b) Scattering data and (c) Gaussian size distributions extracted by fitting the scattering traces.

reason to hope that further understanding of InP nucleation and growth processes will allow similar levels of size control and correspondingly narrow spectral widths to be achieved. These new synthetic techniques will have the difficult task of reducing size distribution related broadening while also not unintentionally introducing disorder related PL broadening from impurity atoms and lattice defects. There should be no fundamental barrier to meeting these requirements and eventually attaining ensemble spectral widths for InP that are comparable to what is currently available for CdSe and CdTe emitters. The SAXS data shown in Figure 2-4 outlines the challenge associated with producing InP colloids with linewidths that are competitive with CdSe. The InP sample shown is more monodisperse than either of two examples of CdSe colloids, “CdSe-1” and “CdSe-2”. Despite this, the more monodisperse of the two CdSe colloids, CdSe-2 shows considerably narrower spectral features than “InP”, a clear representation of the greater sensitivity of ensemble properties of InP QD emitters to homogeneity of the sample.

2.3. Preparation and chemical surface passivation of InP colloids

The previous section establishes that polydispersity If size distribution related broadening were the dominant factor in determining ensemble PL linewidth in colloidal InP, we should expect that photoluminescence excitation spectra collected for narrow selected energy ranges of emission should correspond to the narrow absorption features of a very monodisperse sub-population of particles. However, this is not generally true. As I report here, behavior of InP emission is strongly dependent on chemistry and is related to the presence of lattice disorder and impurity atoms. In this work, internal disorder within InP nanocrystals is considered as an additional factor, independent of particle size, which confounds the preparation of colloidal InP with narrow ensemble emission. The sources of this disorder are related to the chemical schemes used for synthesis and surface passivation of InP quantum dots necessitating a discussion of synthesis and passivation chemistry.

Colloidal InP quantum dots were synthesized by common literature methods[18,19] reacting $InCl_3$ as the indium precursor and made use of tris(trimethylsilyl)phosphine or tris(dimethylamino)phosphine as phosphorous precursors. The colloids were washed in a nitrogen glovebox by repeated dissolution in toluene and precipitation using ethanol as a non-solvent. Finally, the particles were stored as a colloidal stock solution in toluene. These freshly prepared particles are poorly luminescent and are termed "As-synthesized InP" for the purposes of this study. I additionally consider two chemically different types of luminescent InP samples: "InP/ZnS" core-shells synthesized by established protocols[19-21] and as-synthesized InP cores made luminescent by passivation with dilute (200 ppm) HF. Exposure of InP quantum dots to HF solution under nitrogen atmosphere and with particles protected from light results in a modest increase of photoluminescence (PL) quantum yield from nearly zero out of synthesis to around 1% after the treatment. As has been reported previously,[13,22] when this HF treatment is conducted under illumination and in air, it results in slow etching and oxidation accompanied by significant

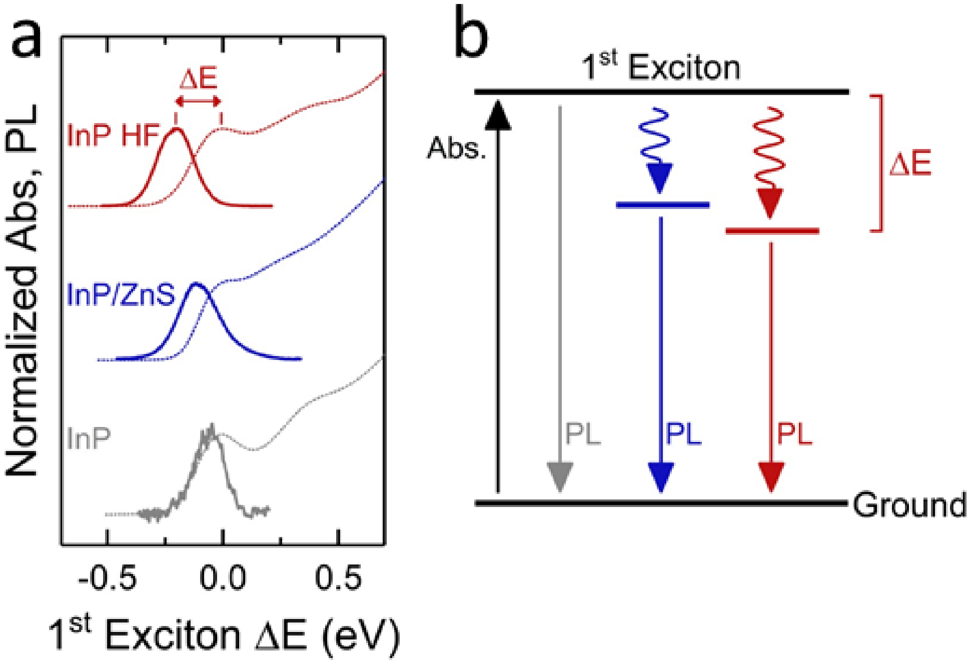

Figure 2-5: Ensemble emission redshift of InP quantum dots. (a) Absorption and emission spectra for three types of InP quantum dots plotted on a scale zeroed at the first exciton energy. The treatments commonly used to enhance PL quantum yield result in emission bands that are shifted red of the first excitonic absorbance by varying amounts. **(b)** Differing amounts of non-radiative energy dissipation precedes emission for different types of luminescent InP quantum dots.

increase of PL quantum yields to 20-40%. This highly luminescent material derived from the as-synthesized particles is termed “InP-HF”.

InP quantum dots reveal an interesting and unusual relationship between behavior as emitters and the chemistry involved in their preparation and surface passivation. Aerobic HF etching introduces a large redshift of the PL band relative to the first absorption maximum (Figure 2-5). The relatively large emission redshift in aerobically HF treated InP is also observed in highly emissive InP/ZnS core-shell samples grown via the commonly used method wherein InP cores are grown from a solution containing mixed In and Zn metal precursors[19,21,23]. Subsequent addition of a sulfur precursor induces the free Zn already present in the reaction mixture to react and form a ZnS shell over the InP cores. While this chemistry is very distinct from the HF-based passivation scheme, the resulting material shows similar PL quantum yield, linewidth, and a PL band centered greater than 150 meV red of the first absorption maximum. The redshift of the emission across these multiple classes of InP shown in Figure 2-5 suggests that more than one radiative recombination pathway is active in the material.

2.4. Energy selective spectroscopies for examining subpopulations within InP quantum dot ensembles

The observation of a variable emission redshift relative to the first excitonic absorption across different InP colloids motivates a deeper look into the origin of emission events across the range of energies within the broad ensemble PL band. Energy selective PL spectroscopies including photoluminescence excitation (PLE) and fluorescence line narrowing (FLN) both allow examination of subsets of emitters within the samples and shed light on the homogeneity of emitting states in nanocrystal colloids. Analysis of ensemble emission of InP, CdSe, and CdTe colloids by PLE and FLN reveals a clear difference between the materials. For polydisperse CdSe colloids, excitation spectra corresponding to narrow emission sub-bands taken in steps across the whole emission profile strongly resemble absorption spectra of monodisperse CdSe samples. Each narrow band of the total emission profile yields an excitation spectrum which scans the absorbance of a more monodisperse subset of the particles. Such behavior is commonly observed from samples made of II-VI semiconductor materials with various surface passivation schemes, including plain cores and various core-shell structures.[24,25]

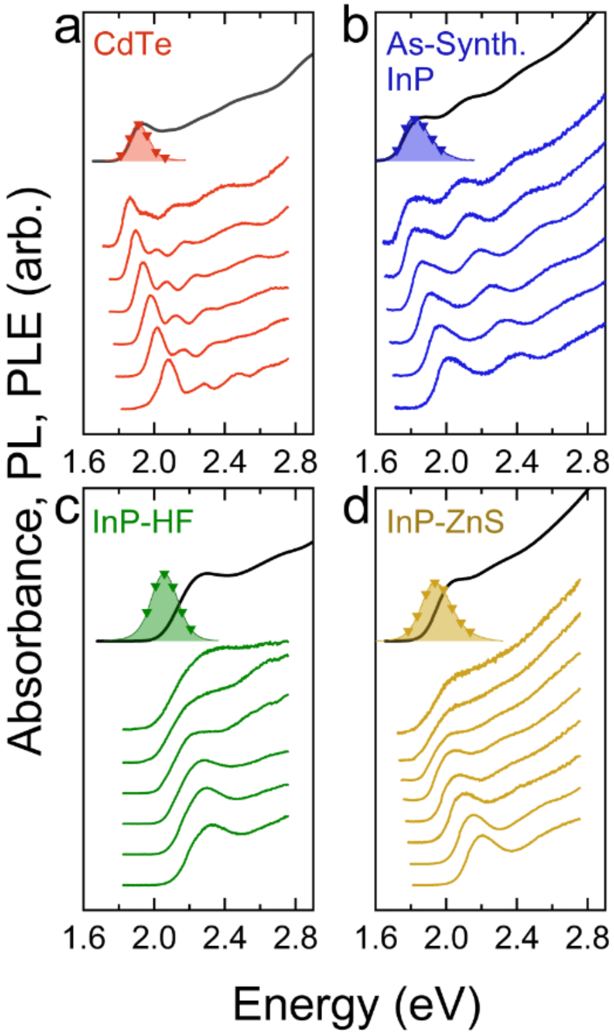

Figure 2-6: PLE spectra of selected InP samples compared to CdTe. Absorption (black traces), PL (shaded), and PLE spectra (colored traces) for polydisperse CdTe quantum dots **(a)**, as-synthesized InP cores **(b)**, HF–treated InP **(c)**, and InP–ZnS core-shell quantum dots **(d)**. The PLE spectra are collected by scanning at emission energies marked by triangle symbols. Spectra are offset higher for successively redder emission energies scanned.

The same is true for other well studied II-VI semiconductors such as CdTe; plotting PLE spectra obtained from energies across the broad emission profile of a polydisperse CdTe colloid (Figure 2-6) yields a particle size series of absorption spectra with sharp excitonic features. InP nanocrystals that are exposed only to anaerobic HF treatment and which retain their small emission redshift show similar behavior to CdSe and CdTe. PLE spectra narrow significantly compared to the ensemble absorption and spectral features shift as the selected emission energy is varied. For all three of these systems, the FLN experiment in which samples are excited at the red edge of their absorption gives similar results as well. Selective excitation of the largest and reddest absorbing particles in the ensemble results in a narrower emission band originating from a subset of absorbers. Taken together, these data suggest that there is no fundamental barrier that prevents colloidal InP from achieving the narrow emission lines that are commonly obtained for II-VI emitters.

While the PLE data from unoxidized and unshelled samples imply that InP emitters behave similarly to CdSe and CdTe, samples of InP with bright PL show a significantly different behavior (Figure 2-6c,d). InP samples that are treated with HF under illumination and exposure to air, or alternatively, samples that are passivated by ZnS shells are both characterized by bright PL that is redshifted from the first absorption peak. Both show broad excitation spectra which broaden further as the analyzed emission band is shifted redder. Figure 2-6 summarizes this result: while II-VI materials of varying degrees of size polydispersity allow for extraction of a narrow sub-population absorption by PLE, the two classes of bright InP considered here do not. As excitation spectra are measured for successively redder emission bands, their spectral features broaden further but do not appreciably change in energy. In other words, redder emission is not correlated with redder absorbers in these samples. The implication here is that the emission at the red-edge of the PL spectrum does not simply originate from a redder population of emitters but from a population of emitters that have a similar absorption edge as the entire ensemble average but that have a recombination pathway that allows emission at lower energy. For typical high quantum yield samples of InP, including both shown in Figure 2-6, the first exciton in the PLE spectra for deep red emission occurs approximately 200 meV blue of the scanned emission band.

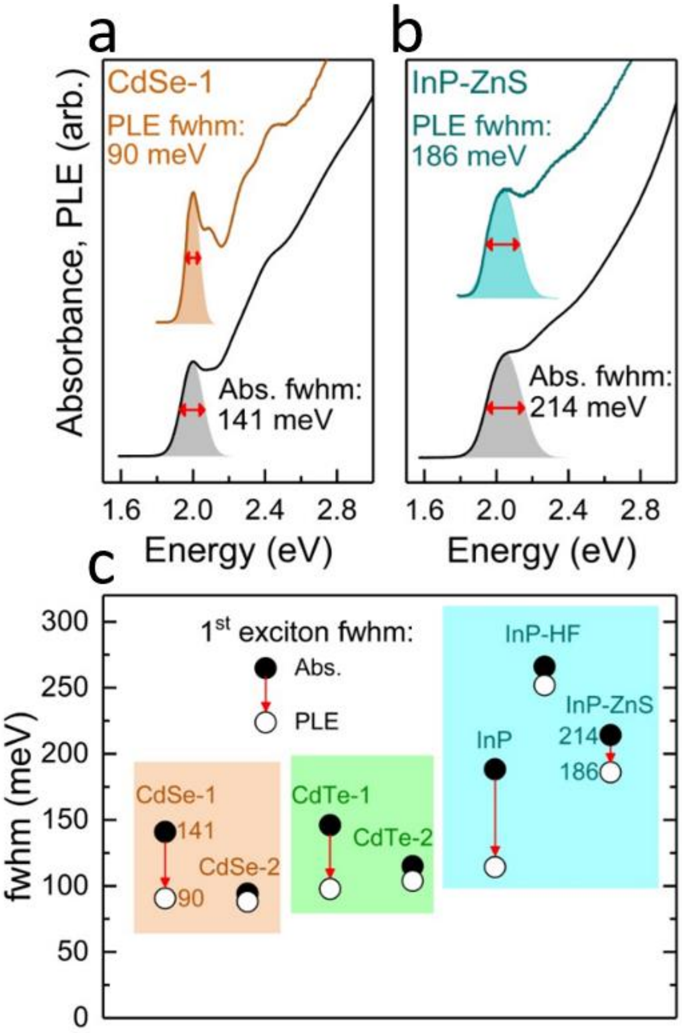

Figure 2-7: Comparison of ensemble absorption spectrum and PLE spectrum linewidths. a,b. Gaussian fits (shaded) compare the fwhm of the first excitonic peak in absorption (black) and PLE (colored) for polydisperse CdSe **(a)** and InP-ZnS core-shells **(b)**. **c.** A summary of first exciton fwhm for absorption (black circles) and PLE(white circles) for a variety of quantum dot samples. PLE linewidth values are extracted from spectra obtained by scanning the center of the PL band for each sample. CdSe and CdTe samples appended by “1” and “2” represent more polydisperse and more monodisperse samples respectively.

The ramifications of the PLE studies can be summarized by comparing ensemble absorption linewidths to those of the corresponding excitation spectra extracted from the center of the emission band. Figure 2-7 displays the results of making such a comparison. Data is included for four samples of II-IV semiconductor emitters: CdSe-1(polydisperse), CdSe-2(monodisperse), CdTe-1(polydisperse), and CdTe-2(monodisperse). From these four samples PLE spectra are extracted with a full width at half maximum (fwhm) of the first excitonic feature of roughly 90 meV, independent of material or polydispersity. That narrower PLE spectra are not extractable for the more monodisperse samples suggests that this ~90 meV value originates from a combination of the single particle emission linewidth and measurement related broadening. The weakly emitting InP colloid (Figure 2-6b, Figure 2-7c) behaves similarly to CdSe and CdTe yielding a narrowed PLE spectrum with a 114 meV first exciton fwhm. For a detailed view of PLE spectra of the samples in Figure 2-7 that includes excitation spectra measured for a range of energies across the ensemble emission profiles of the samples see Figure 2-14 through Figure 2-22. The roughly 20% broader linewidth for InP compared to CdSe and CdTe is consistent with prior determinations[26] of the single particle emission widths of these materials. In contrast, the brightly emitting classes of InP (Figure 2-6c,d), InP-HF, and InP-ZnS both yield broad features in their PLE spectra. This observation contradicts the characterization of these bright InP colloids as emitting from a size distribution broadened ensemble of narrow single emitters. Rather it points to the bright redshifted PL as resulting from a shallow trap assisted radiative recombination process. If the depth of traps states (ΔE as described in Figure 2-5) varies from dot to dot, the broad ensemble emission is expected from reasonably monodisperse samples of InP NCs showing narrow emission lines in single-particle PL studies. In the following sections I investigate the nature of the emissive states in bright InP NCs using time-resolved spectroscopies.

2.5. Time-resolved spectroscopies for investigation of picosecond timescale carrier dynamics

Transient absorption and fast time-resolved photoluminescence measurements by streak camera were undertaken to further understand the role of HF etching and ZnS shelling in bringing about bright luminescence. In particular, I sought to understand the effect of passivation chemistry on the lifetimes of photogenerated electrons and holes individually. According to the state filling picture[27] for describing transient absorption in quantum confined II-VI and III-V semiconductors differential absorption signals are dominated by the state occupation of the electron due to its lower effective mass and the lower degeneracy of the conduction band. We should thus expect that decay kinetics of the transient bleaching signal will reflect electron state occupation

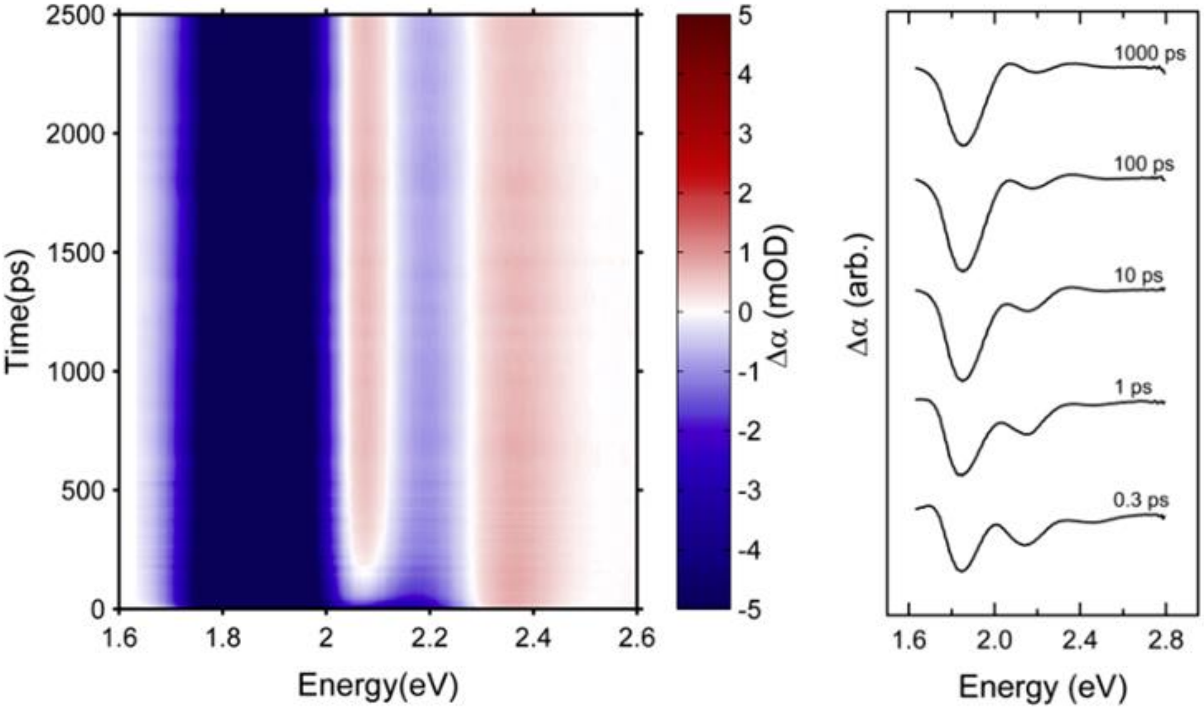

Figure 2-8: Left, a colormap showing the spectral evolution of the transient absorption of an as–synthesized InP sample as an example dataset. Right: offset, un-normalized Δα spectra extracted at a discrete series of probe delays (0.3ps – 1000 ps) from the same data used to generate the colormap at left.

only and be relatively insensitive to hole trapping events. In contrast, picosecond timescale photoluminescence measurements give information about the net population of the emissive state. Irreversible trapping of either carrier will contribute to the observed kinetics. By combining the two techniques, the relationship between InP passivation chemistry and relaxation pathways of electrons and holes can be understood.

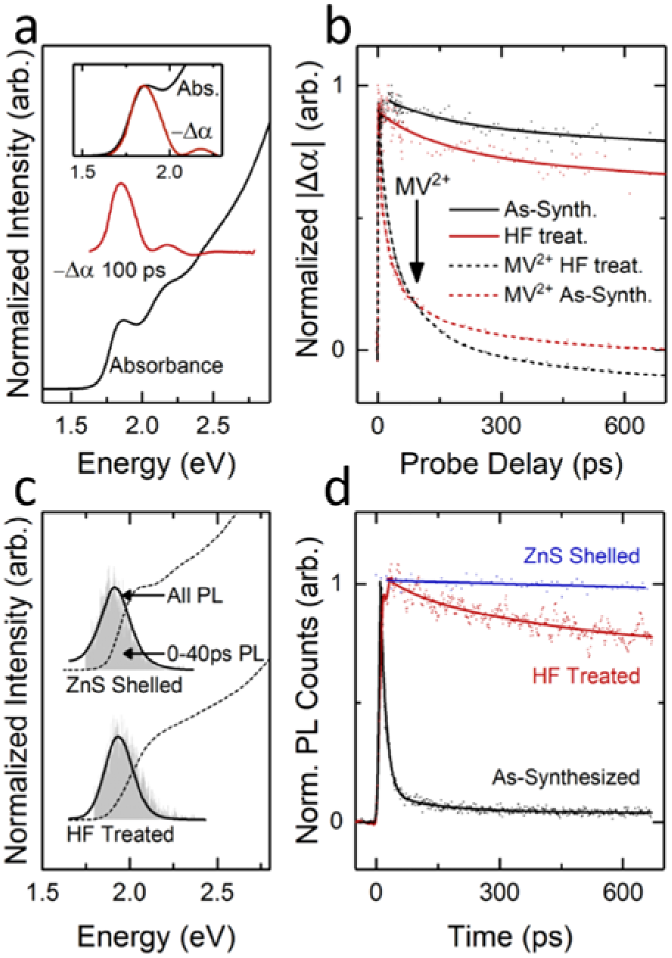

Figure 2-9: a. Absorbance and 100 ps probe delay differential absorption spectra from InP with or without post-synthetic modifications. The inset compares the absorption line to the ground state bleach of the first exciton. The pump energy is 3.0 eV. **b.** Intensity of the first exciton bleach vs. probe delay time for as synthesized and HF treated InP. The dashed lines show measurements where methyl viologen dichloride, acting as the electron scavenger, was added to the sample. **c.** Comparison of steady-state PL spectra, solid lines, and emission in the 40 picoseconds following a pulsed excitation measured by streak camera, shaded grey. Dashed lines show the corresponding absorption spectra. **d.** Spontaneous PL decay for three types of InP also by streak camera. Excitation is at 3.1 eV for the steady-state and pulsed PL measurements.

A pump-probe transient absorption experiment with blue pump (3.0 eV) and broadband probe yielded set of differential absorption spectra vs. pump delay for all samples. Spectra taken in the first few picoseconds following excitation show a rapid spectral evolution due to carrier cooling (Figure 2-8). The observation that evolution of the shape of the Δα spectrum ceased completely by 100 picoseconds was found to hold generally for all samples considered. For probe delays of 100 ps and longer, the Δα signal at all probe energies simply decayed monotonously. Following the completion of this process, the spectral evolution ceases and the shape of the differential absorption spectrum then remains static and the signal strength decays monotonously in intensity with increasing pump delay. At this stage, photo-excited electrons bleach the oscillator strength of transitions which correspond to promotions of valence band electrons to the occupied conduction band level. Accordingly, the strongest and slowest decaying signal is a bleach which corresponds in energy and lineshape to the first excitonic feature in the linear absorption spectrum (Figure 2-9). The energy of this transition has a well-studied dependence on nanocrystal size due to quantum confinement effects.[13,28] Thus, electrons relax to a delocalized $1S_e$ “particle in a spherical box” state and bleach the first excitonic absorption by blocking valence band to $1S_e$ transitions.

The first exciton bleach recovery kinetics on the timescale of hundreds of picoseconds should then simply track the population of electrons in the $1S_e$ state: $|\Delta\alpha| \propto [e^-]$. Analysis of these kinetics (Figure 2-9b) for samples with different surface passivation chemistries finds that decay of the conduction band electron population is slow on the sub-nanosecond timescale. Measurements at longer probe delays (Figure 2-10, Figure 2-11) find that depletion of the $1S_e$ state following the pump takes place over tens of nanoseconds, a similar rate as for radiative recombination in emissive samples. Slow kinetics were seen for all samples investigated with no

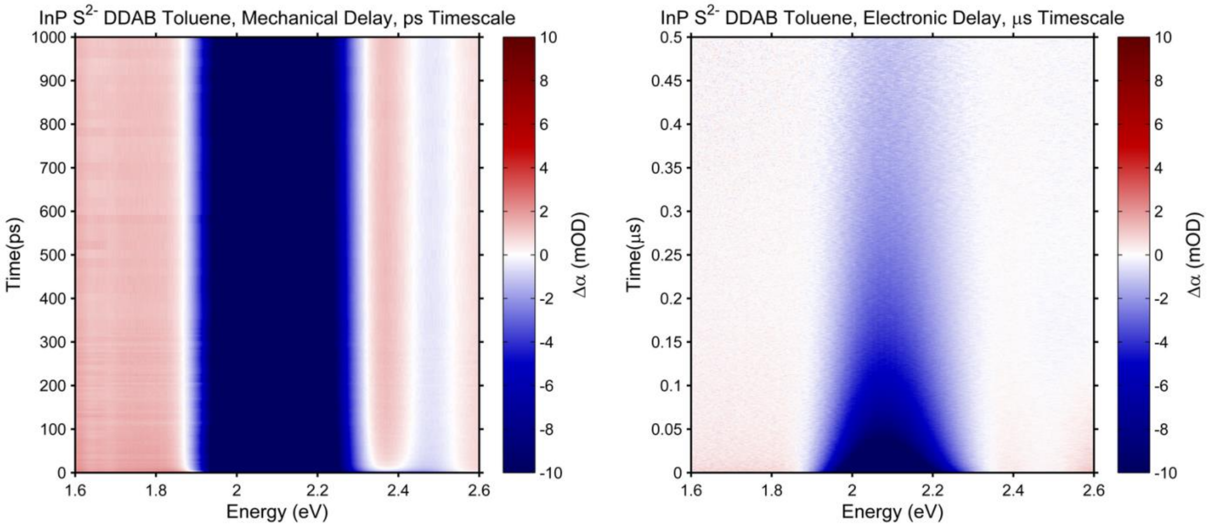

Figure 2-10: Transient absorption maps at different timescales. An example of two transient absorption experiments at different timescales measured on the same sample of InP nanocrystals. Left, picosecond timescale data collected using the Ultrafast Systems Helios instrument with a probe delay modulated by a mechanical translation stage. Right, data collected at microsecond timescales using an electronically delayed pump on the Ultrafast Systems Eos instrument.

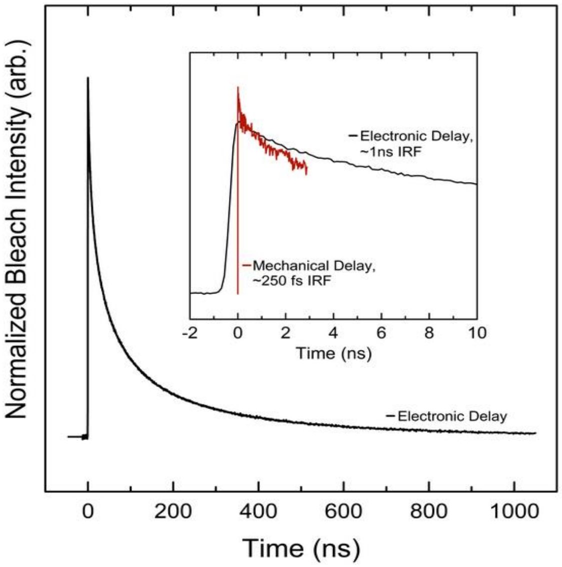

Figure 2-11: Transient absorption kinetics at different timescales. Kinetics extracted for the first exciton bleach decay of InP nanocrystals in the long timescale transient absorption experiment with electrically delayed probe. The inset shows a comparison between kinetics at early times for this experiment and for the data collected with the mechanically delayed pump and with pump and probe pulses that are shorter in time. The instrument response functions for the two measurements are approximately 1 ns and 150 ps for the electronically delayed and mechanically delayed setups respectively.

apparent connection between the rate of bleach recovery and the steady state PL quantum yield of the sample. These data imply that electron trapping rates are similar, and negligible, in all samples. This is a surprising conclusion given that the PL quantum yields of the HF treated samples are approximately 3 orders of magnitude greater than the as-synthesized quantum dots. The implication is that sub-nanosecond PL quenching in the non-luminescent samples can be attributed to hole trapping.

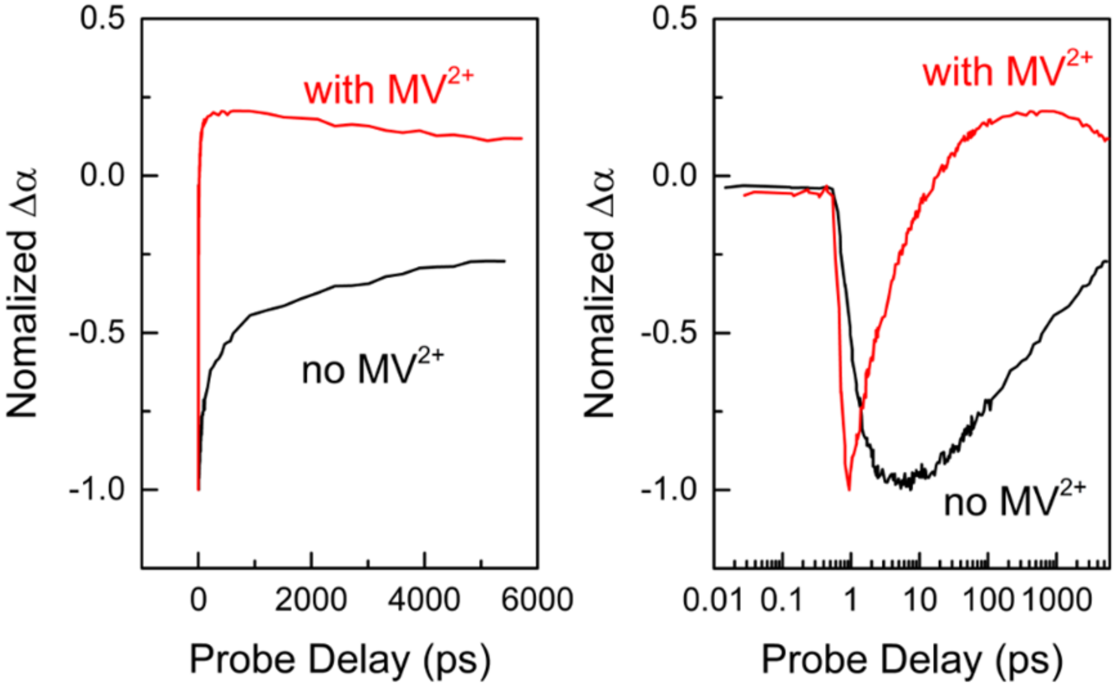

Figure 2-12: Left, first exciton bleach decay kinetics for sulfide capped InP nanocrystals dispersed in N-methylformamide. In the sample with addition of methyl viologen (MV^{2+}), the population of the 1S$_e$ state is rapidly depleted due to excited state electron transfer to MV^{2+}. The bleach signal gives way to an induced absorption originating from the MV^{+} radicals that form due to the charge transfer. Right, the same information is plotted but with a log scale on the horizonal axis for clarity. The charge transfer process goes to completion within tens of picoseconds.

To validate the interpretation of the transient absorption data as providing selective information about electron dynamics, I conducted an additional control experiment by repeating measurements with addition of an electron scavenger, methyl viologen dichloride (MV^{2+}), to the nanocrystal solutions under investigation. Previous studies of carrier dynamics in quantum dots,[29,30] have used MV^{2+} as a selective electron scavenger which undergoes rapid reduction by photogenerated conduction band electrons. Indeed, its addition to the InP quantum dot solutions results in rapid loss of the conduction band electron population following excited state electron transfer to MV^{2+} (Figure 2-9b and **Figure *2-12***). The spectroscopic signature of the singly reduced methyl viologen radical MV^{+}• appears concomitantly with the loss of the bleach signal from the quantum dots and decays negligibly slowly over the 2.5 nanosecond time interval of the TA experiment. The long life of the radical indicates that there is no fast hole transfer following the initial electron transfer. Rather, the reduced MV^{+}• radical coexists with positively charged quantum dots. Additionally, there is not a strong differential absorption signature observed from the hole remaining on these positively charged InP quantum dots, an observation that agrees well with the prediction that the high valence band density of states will obscure the contribution of a single valence band hole to the absorbance. The conclusion is that for all InP chemistries studied, electron trapping is negligible on sub-nanosecond scales unless an electron trapping species is intentionally introduced.

In contrast, measurements of photoluminescence show a strong relationship between surface chemistry and kinetics (Figure 2-9d). While luminescent HF treated and ZnS-shelled quantum dots show a PL decay that matches the TA kinetics (Figure 2-13), for as-synthesized InP PL decay is quite fast. Even for non–luminescent InP with PL decay on the timescale of tens of picoseconds, the bleach intensity decay in transient absorption takes place over tens to hundreds of nanoseconds. Further, this decay is slower than the PL decay of the passivated samples. This reinforces the evidence that hole trapping is the dominant PL quenching mechanism in colloidal InP and that electron trapping is slow even on the half microsecond timescale. However, trapping

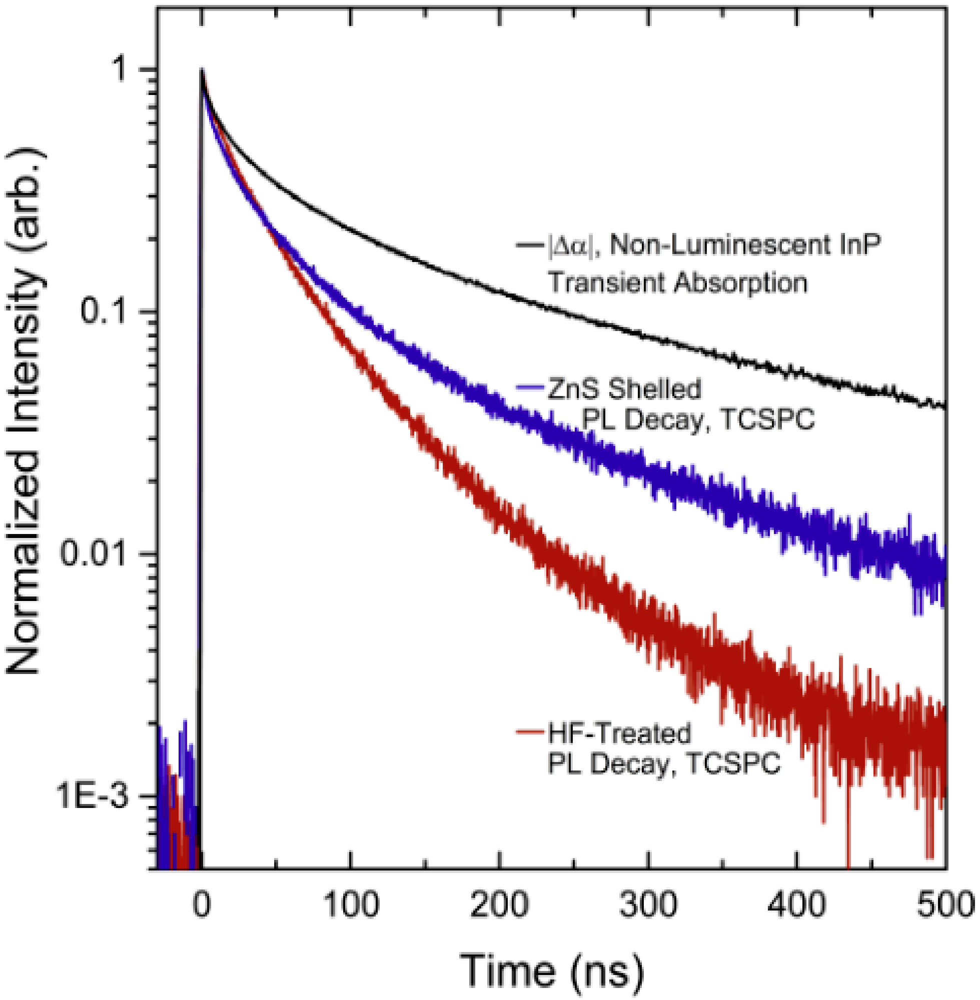

Figure 2-13: A comparison of bleach recovery and PL decay at the hundreds of nanoseconds timescale. The black trace shows the bleach recovery kinetics obtained from a transient absorption setup using an electronically delayed pump. The blue and red traces show PL lifetime data obtained from TCSPC for InP made luminescent by post–synthesis ZnS shelling or by HF treatment.

of electrons can be an important quenching mechanism when fast electron traps are present as they are upon addition of methyl viologen. All samples with MV^{2+} added exhibited total quenching of measurable PL from the nanocrystals, further supporting the interpretation of the TA results as rapid reduction of MV^{2+} by $1S_e$ electrons in excited InP. Given the long lifetime of electrons in the $1S_e$ state, the observed PL decay kinetics on the sub-nanosecond timescale can be attributed to hole trapping rates. PL decay dominated by hole trapping allows the kinetics in Figure 2-9d to be interpretable as tracking the hole population remaining in a state that can recombine radiatively with electrons in the $1S_e$ state: $I_{PL} \propto [h^+]$. This is in line with predictions made by previous studies of the photochemical mechanism of HF passivation[22,31] and contradicts other reports[32,33] which pointed to electron trapping at phosphorous vacancies as the predominant source of PL quenching in unmodified InP.

Given that InP quantum dots show PL decay rates which either match or greatly exceed the decay rate of the $1S_e$ population, photoluminescence is expected to come from recombination of holes with these delocalized conduction band electrons. A question then arises as to whether the highly Stokes shifted PL in luminescent InP is a band to band process with a hole in the $1S_h$ state recombining with the $1S_e$ electron. Alternatively, the low energy of the emission could be explained by a trap to band process in which the holes relax to a midgap state and subsequently recombine radiatively with the long-lived free electrons. If this is the case, emission at early times may contain a significant higher energy component from electrons combining with untrapped holes. The trapping process should then be resolvable as a shift in emission energy by spectrally resolved fast photoluminescence measurements. The result of integrating photon counts Figure 2-9d. Photons emitted in the time interval from 0 to 40 picoseconds after excitation show very similar spectral width and Stokes shift to those collected in a steady state PL measurement. The conclusion is that any population transfer of holes must occur faster than the tens of picoseconds timescale. Given the fast kinetics of excited state electron transfer to adsorbed MV^{2+} seen in sulfide capped InP (**Figure *2-12***), a hole relaxation rate that exceeds the time resolution of the streak camera measurement is plausible.

2.6. Further investigations, concluding remarks, and a hypothesis

In order to understand carrier dynamics in InP nanocrystal colloids at a femtosecond timescale, and to deconvolute the effects of homogenous and inhomogeneous broadening of ensemble optical signals, I worked in collaboration with Dr. Nicholas Williams for further spectroscopic characterization using Two-Dimensional Electronic Spectroscopy (2DES). For detailed discussions of these experiments, please see the sections titled "*Femtosecond Excited Carrier Dynamics Accessed by Two-Dimensional Electronic Spectroscopy*" and "*Exciton–Phonon Coupling Probed by 2DES Quantum-Beating Maps*" in J. Am. Chem. Soc. 2018, 140, 46, 15791-15803. The measurements compared as-synthesized InP to ZnS-shelled material and found evidence the broad linear absorption features seen in ZnS shelled InP (Figure 2-6), are the result of a manifold of closely spaced electronic states rather than pure heterogeneity of size. Further, analysis of signal beating amplitudes pointed to increased strength of exciton phonon-coupling in InP-ZnS. Stronger exciton-phonon coupling had been previously investigated[34,35] and reported to be typically attributable to spatial separation of charge carriers. Such a finding is explainable if surface or interior defects are unintentionally introduced during the chemical passivation processes involved in ZnS shelling. The combination of findings from the PLE, TA, streak camera, and 2DES experiments led to the hypothesis that the observed broad, redshifted emission from bright InP samples is related to lattice disorder that results in emission coupled to localized band edge carriers.

2.7. Gallery of selected photoluminescence excitation data:

This section contains full sets of absorption, PL, and PLE data. The panels on the left show steady-state absorption (black traces) and PL (red traces) under blue light excitation for samples examined in the PLE study. The left panel insets show a zoomed in view of the emission line with "o" markers designating the emission energies at which PLE spectra were acquired. The fwhm labels refer to the linewidth of the PL bands. The panels on the right show normalized, offset, excitation spectra collected for the reddest emission energies on top and incrementally bluer energies descending. Regions of the PLE spectra where scattered excitation light was detected are removed for clarity.

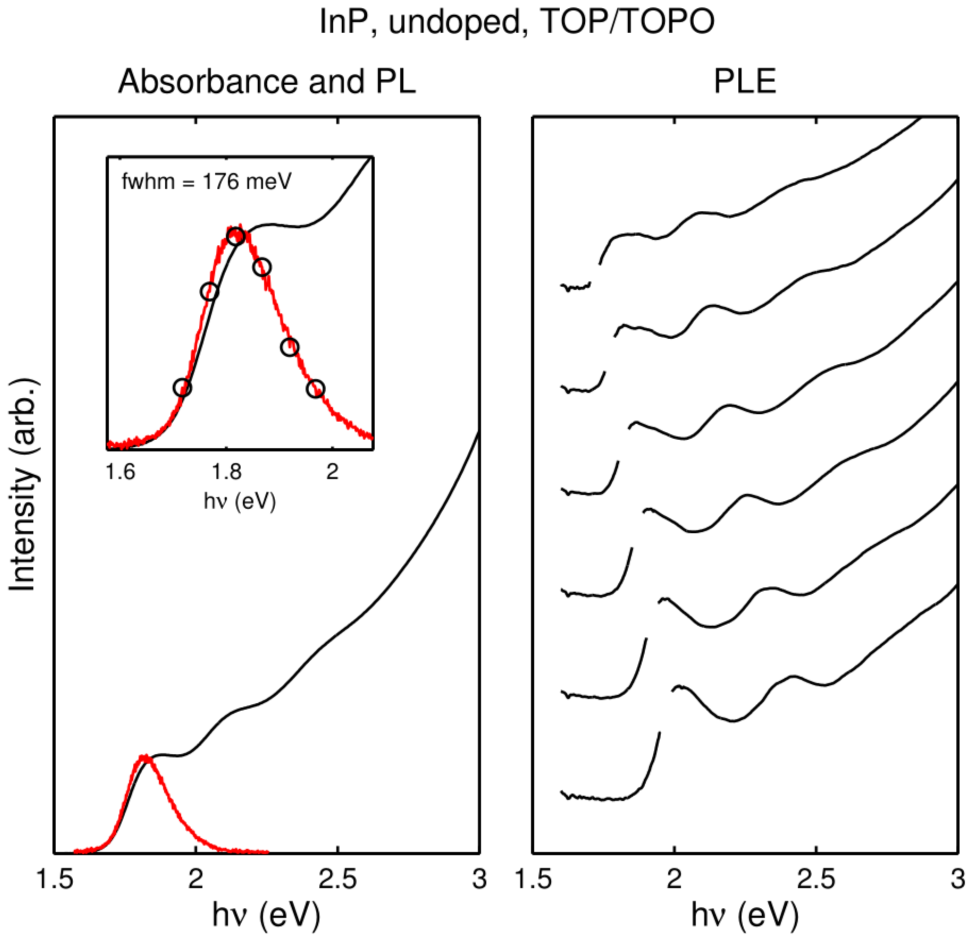

Figure 2-14: Absorption and steady-state PL, and PLE for as-synthesized InP.

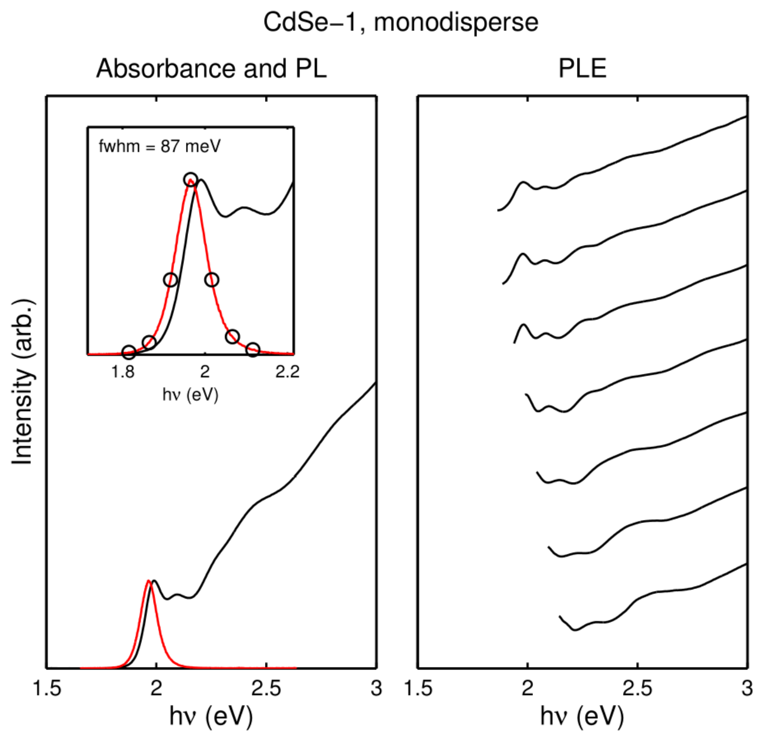

Figure 2-15: Absorption and steady-state PL, and PLE for monodisperse CdSe.

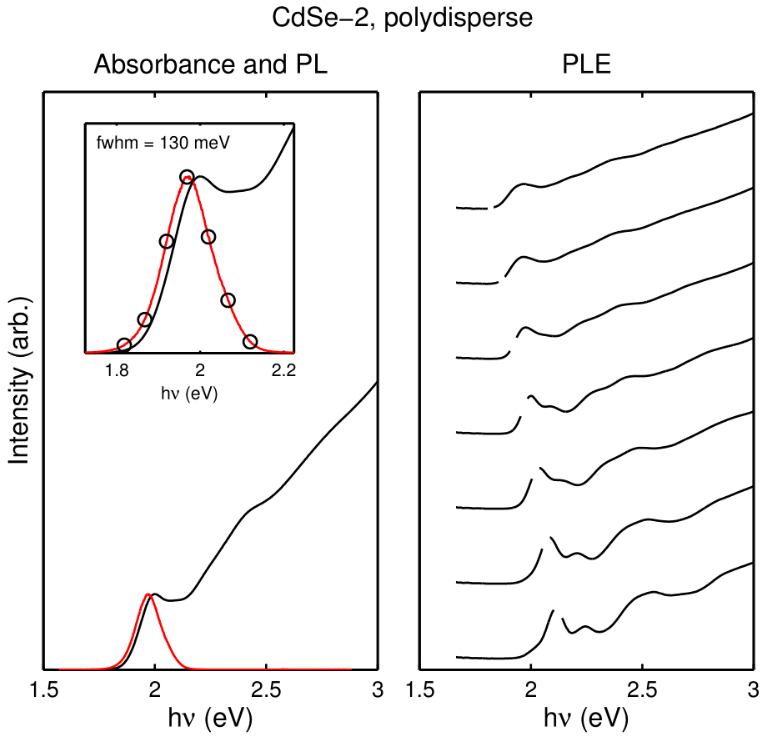

Figure 2-16: Absorption and steady-state PL, and PLE for polydisperse CdSe

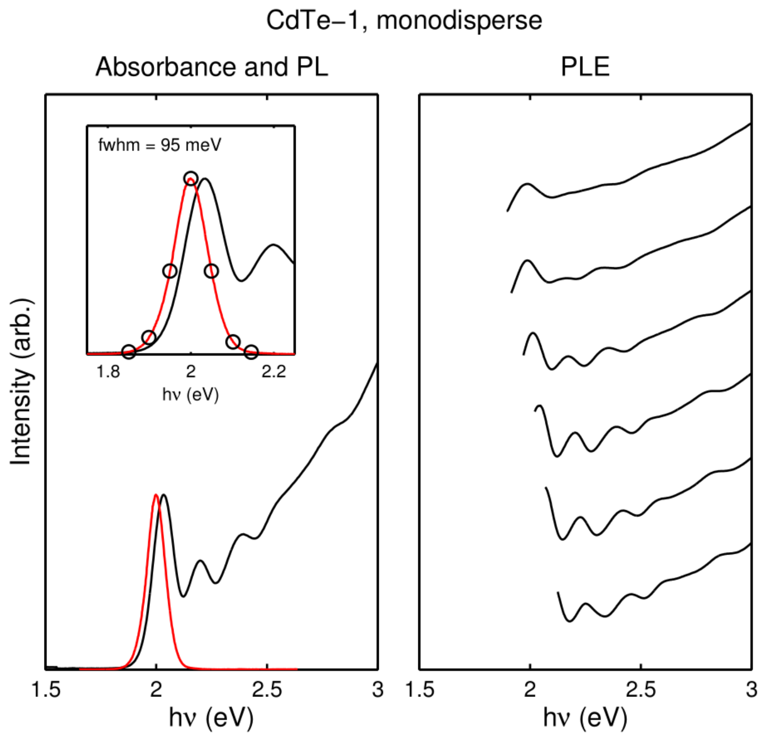

Figure 2-17: Absorption and steady-state PL, and PLE for monodisperse CdTe.

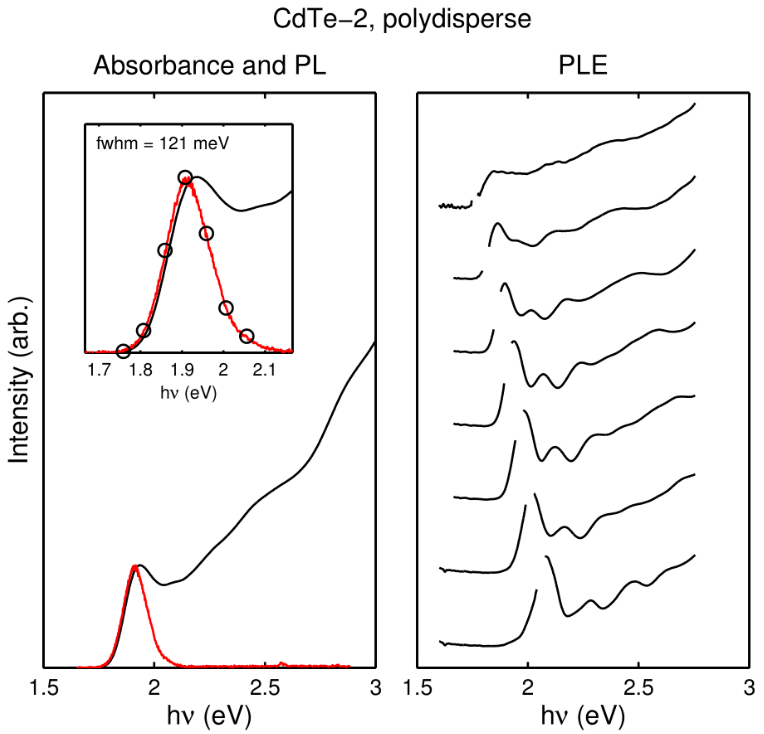

Figure 2-18: Absorption and steady-state PL, and PLE for polydisperse CdTe.

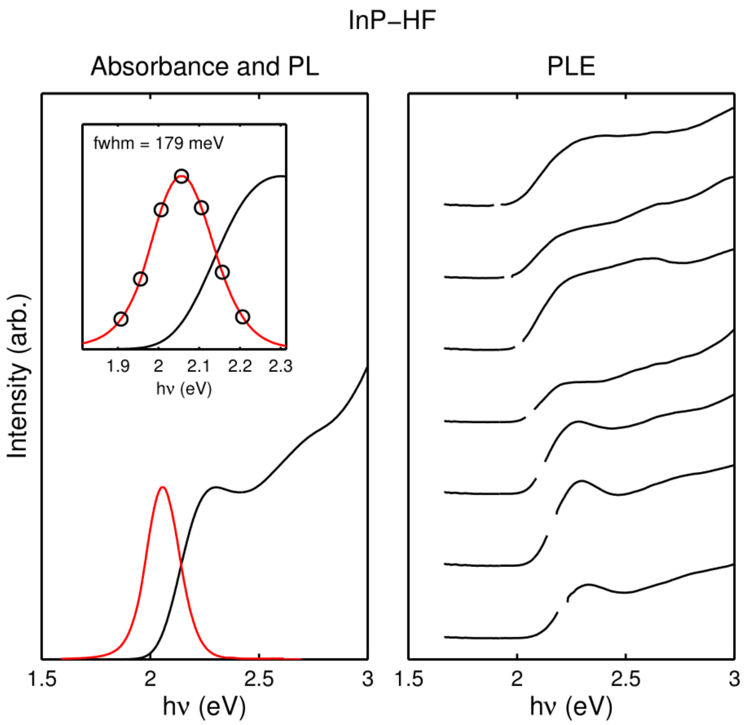

Figure 2-19: Absorption and steady-state PL, and PLE for aerobically HF-treated InP.

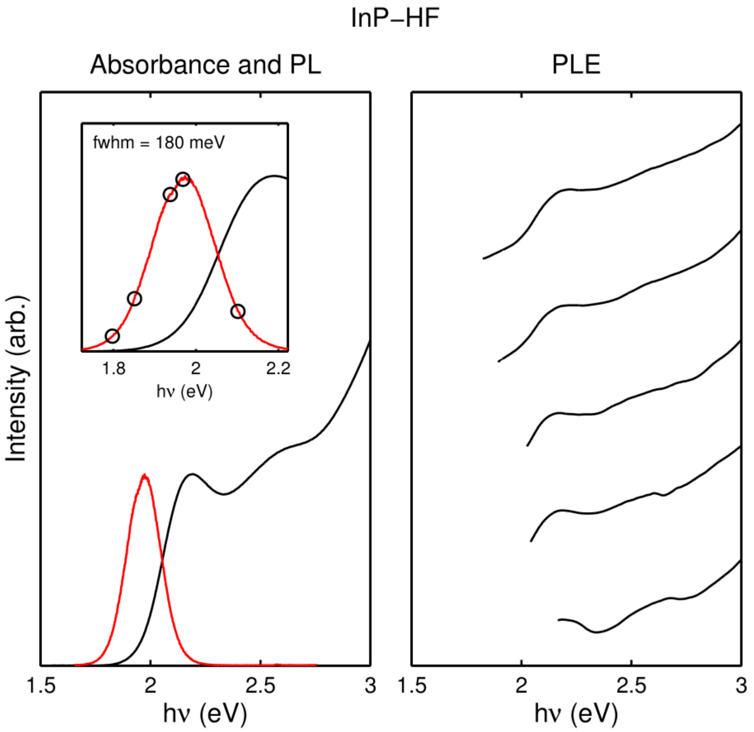

Figure 2-20: Absorption and steady-state PL, and PLE for another sample of aerobically HF-treated InP.

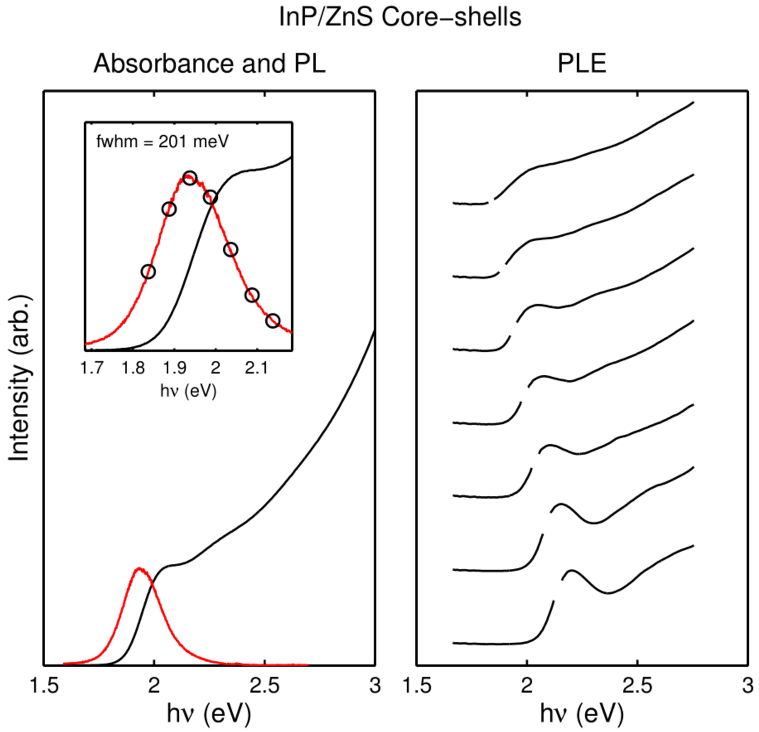

Figure 2-21: Absorption and steady-state PL, and PLE for ZnS shelled InP.

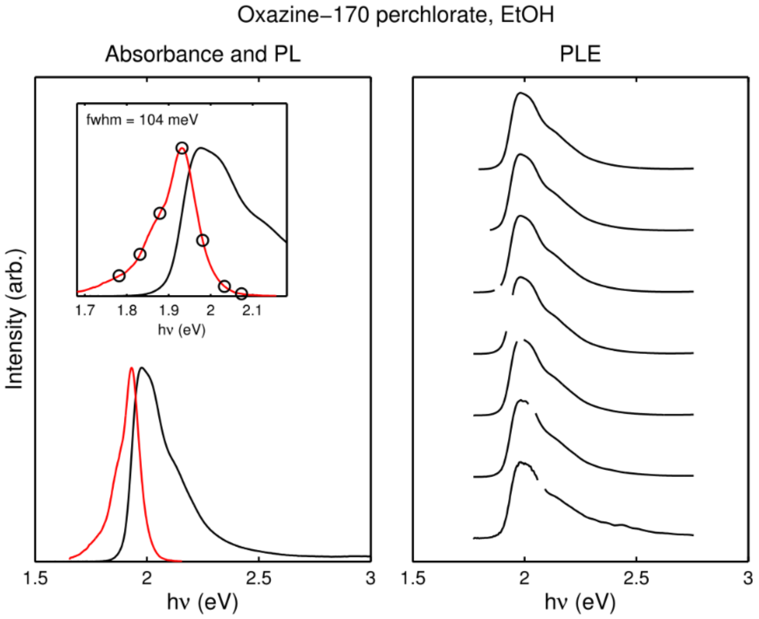

Figure 2-22: Absorption and steady-state PL, and PLE for oxazine-170 perchlorate dissolved in ethanol.

2.8. Experimental methods:

Nanocrystal growth procedures:

InP Nanocrystals:

InP nanocrystals were synthesized following a route adapted from (18). Briefly, 1g $InCl_3$ (4.52 mmol), 1.5g trioctylphosphine oxide (3.88 mmol) and 15 mL of tri-n-octylphosphine were combined in a nitrogen glovebox and stirred at room temperature. After complete dissolution of the solids, the solution was filtered through a 0.2 micron PTFE filter into a three neck flask which was then sealed and transferred air-free to a Schlenk line under nitrogen purge. With the contents of the flask at 25°C, 0.75g (869 µL, 4 mmol) of tris(trimethylsilyl)phosphine was injected. The temperature of the flask was then raised to 270°C and maintained under stirring for 16 hours. Particles were washed under the inert atmosphere of a nitrogen filled glovebox by precipitation with ethanol followed by redispersal in toluene. After another step of precipitation/redispersal, the particles were size selectively precipitated from toluene by incremental addition of ethanol followed by centrifugation after each addition.

Zn-Doped InP Nanocrystals:

InP nanocrystals doped with Zn were synthesized by a method adapted from ([19]) mixing 1g $InCl_3$ (4.52 mmol), 616 mg $ZnCl_2$ (4.52 mmol), and 15 mL of oleylamine in a three-neck flask connected to a Schlenk line. The flask is then purged of air by three cycles of evacuation for 5 minutes followed by refilling with nitrogen. Under nitrogen, the flask is then heated to 115°C and evacuated for 30 minutes, refilled and heated under nitrogen to 230°C. At 230°C, 1.5 mL of tris(dimethylamino)phosphine (8.25 mmol) is injected. Caution should be used in this step to not build up too large an overpressure in the flask as the injection is accompanied by evolution of gas. After injection of the phosphorous precursor, the mixture is left to stir at 230°C for one hour then is cooled to room temperature and transferred to a nitrogen glovebox for purification. Particles are recovered from the reaction mixture by precipitation with ethanol and are washed by cycles of dispersal in toluene and precipitation by ethanol just as for undoped nanocrystals.

InP/ZnS Core-Shell Nanocrystals:

InP cores with ZnS shells were grown by a similar method to ([21]), following the standard Zn-doped InP core synthesis with the addition of a shelling step. The sulfur precursor, tri-n-octylphosphine sulfide (TOP-S) was prepared in a nitrogen glovebox by stirring a stoichiometric equivalent of sulfur in tri-n-octylphosphine solvent for 1 day. The resulting clear liquid was filtered and stored. The Zn precursor, Zn-oleate, was prepared by Schlenk line chemistry in a three-neck flask. A stock solution of Zn-oleate in 1-octadecene was prepared by reacting 1 equivalent of zinc acetate with 2 of oleic acid to yield a 0.2 M final solution of Zn-oleate. The reagents were combined in a three-neck flask, purged of air by cycles of vacuum and nitrogen refill, heated to 115°C, and placed under vacuum for 30 minutes. The flask was then refilled with nitrogen and heated to 280°C, held at that temperature for 1 hour, then cooled to 100°C for use as a Zn precursor. A 3 mmol aliquot of TOP-S was injected into a flask containing a completed InP synthesis, still at 230°C and allowed to react at that temperature for 30 minutes. An additional 3 mmol each of Zn-oleate and TOP-S were then injected in alternating 1 mmol aliquots starting with TOP-S and finishing with the last 1 mmol of Zn-oleate in 1-octadecene. The reaction was then heated to 250°C and allowed to react at that temperature for 1 hour before cooling to room temperature and standard washing in a nitrogen glovebox.

CdSe Nanocrystals:

Monodisperse CdSe (CdSe-2) nanocrystals were synthesized following the zincblende CdSe seeds recipe from ([36]). Cadmium and selenium precursors were prepared in two separate three-neck flasks connected to a Schlenk line. For the Cd precursor, 5mmol CdO, 15 mmol oleic acid and 10 mL of 1-octadecene were combined and after a standard de-gas at room temperature and 115°C, the flask was heated to 300°C and later cooled to 270°C. The selenium precursor was prepared by adding 1 mmol of Se to 10 mL of 1-octadecene, de-gassed at room temperature and heated up to 300°C under nitrogen. 4mL of the Cd precursor solution was then injected into the Se precursor solution and allowed to react for 15 minutes at 270°C. After cooling to room temperature the nanocrystals were recovered by precipitation with acetone and were then washed as normal with cycles of dispersion in toluene and precipitation by ethanol. Polydisperse CdSe nanocrystals (CdSe-1) were obtained by Ostwald ripening of washed monodisperse material. Half the product of a synthesis was mixed with 10 mL 1-octadecene and 2 mL oleic acid, de-gassed and heated to 250°C for 90 minutes. After cooling the material was recovered with acetone and washed with toluene and ethanol.

CdTe Nanocrystals:

Monodisperse zincblende CdTe nanocrystals (CdTe-2 in the main text) were prepared following a scaled up version[37] of the synthesis from ([38]). A stock solution of tri-n-butylphosphine telluride in tri-n-butylphosphine (10% wt Te) was prepared by stirring elemental Te in tri-n-butylphosphine for 24 hrs in a nitrogen glovebox. The Cd precursor was prepared by mixing 1 mmol CdO and 2 mmol tetradecylphosphonic acid in 40 grams of 1-octadecene. The precursor was de-gassed at room temperature and 115°C, then heated to 300°C to form a clear solution of the cadmium phosphonate complex. The Cd precursor solution was cooled to 250°C and a mix of 2.5 g of the Te precursor solution (2 mmol Te), 2.5 g of tri-n-butylphosphine, and 10 g of 1-octadecene were injected into it. After 3.5 minutes of reaction, 30 mL of de-gassed, room temperature 1-octadecene was injected into the flask to quench the reaction mixture and prevent unwanted Ostwald ripening. Polydisperse CdTe nanocrystals (CdTe-1) were synthesized by the same Ostwald ripening procedure as was used for the polydisperse CdSe, but with a cooking temperature of 230°C and a cook time of 30 minutes.

Spectroscopic and x-ray characterization methods:

UV-Vis-NIR Absorption:

Steady-state optical absorption measurements were collected on a Varian Cary 500 UV-Vis-NIR spectrophotometer.

PL/PLE:

Steady-state photoluminescence (PL) and photoluminescence excitation (PLE) spectra were collected using a Horiba Fluoromax-4 fluorimeter. Unless otherwise stated, PL spectra were acquired with a 450 nm excitation. For both the PL and PLE measurements reported in the main text, monochromator slits were set at 3 nm at both the entrance and exit slits. PLE spectra collected at 1 nm slit settings were found to yield comparable lineshapes indicating a negligible instrumental broadening. Excitation spectra shown in the main text have excitation scatter subtracted for clarity. Quantum yields were measured by comparison to the reference dye Oxazine-170.

Transient Absorption:

The pump-probe transient absorption experiment was carried out using a Helios (Ultrafast Systems) spectrometer and amplified Ti:sapphire laser operated at 800 nm with a 2 kHz repetition rate and a 35 fs pulse width. 5% of the amplifier output was delayed and focused onto a sapphire plate producing a white light probe pulse. The pump pulse was 400nm (3.1 eV) with fluence varied from 0.005 to 1mJ/cm^2.

Streak Camera:

Sub-nanosecond timescale PL decay dynamics were measured via excitation with a 2 kHz 400 nm pump with 250 nJ excitation power. Spectrally resolved dynamics were acquired using a Hamamatsu streak camera with single photon sensitivity.

TCSPC:

Hundreds of nanoseconds to microsecond PL decay dynamics were measured by time-correlated single photon counting (TCSPC) on a Horiba TemPro using a 392 nm pulsed LED source with 1.3 ns pulse width and a PPD-650 modular photomultiplier tube (PMT) based detector.

SAXS:

Small angle x-ray scattering (SAXS) measurements were collected at the Advanced Photon Source beamline XSD-CMS 12-ID-B at Argonne National Laboratory.

TEM:

Transmission electron micrographs were acquired using a Tecnai F30 microscope at 300 kV accelerating voltage. Samples were imaged on 400 mesh copper grids with amorphous carbon support (Ted Pella).

2.9. Chapter 2 bibliography

(1) Dai, X.; Deng, Y.; Peng, X.; Jin, Y. *Advanced Materials* **2017**, 1607022.

(2) Manser, J. S.; Christians, J. A.; Kamat, P. V. *Chemical Reviews* **2016**, *116*, 12956.

(3) Chang, J. C.; Kovtun, O.; Blakely, R. D.; Rosenthal, S. J. *Wiley Interdisciplinary Reviews: Nanomedicine and Nanobiotechnology* **2012**, *4*, 605.

(4) Kim, S.; Kim, T.; Kang, M.; Kwak, S. K.; Yoo, T. W.; Park, L. S.; Yang, I.; Hwang, S.; Lee, J. E.; Kim, S. K.; Kim, S.-W. *Journal of the American Chemical Society* **2012**, *134*, 3804.

(5) Li, Y.; Hou, X.; Dai, X.; Yao, Z.; Lv, L.; Jin, Y.; Peng, X. *Journal of the American Chemical Society* **2019**, *141*, 6448.

(6) Cui, J.; Beyler, A. P.; Marshall, L. F.; Chen, O.; Harris, D. K.; Wanger, D. D.; Brokmann, X.; Bawendi, M. G. *Nat Chem* **2013**, *5*, 602.

(7) Franke, D.; Harris, D. K.; Xie, L.; Jensen, K. F.; Bawendi, M. G. *Angewandte Chemie International Edition* **2015**, *54*, 14299.

(8) Li, Y.; Pu, C.; Peng, X. *Nano Research* **2017**, *10*, 941.

(9) Xie, L.; Shen, Y.; Franke, D.; Sebastián, V.; Bawendi, M. G.; Jensen, K. F. *Journal of the American Chemical Society* **2016**, *138*, 13469.

(10) Brus, L. E. *The Journal of Chemical Physics* **1984**, *80*, 4403.

(11) Brus, L. *The Journal of Physical Chemistry* **1986**, *90*, 2555.

(12) Adachi, S.; Capper, P.; Kasap, S.; Willoughby, A. *Properties of Semiconductor Alloys: Group-IV, III-V and II-VI Semiconductors*; Wiley, 2009.

(13) Mićić, O. I.; Cheong, H. M.; Fu, H.; Zunger, A.; Sprague, J. R.; Mascarenhas, A.; Nozik, A. J. *The Journal of Physical Chemistry B* **1997**, *101*, 4904.

(14) Mićić, O. I.; Sprague, J.; Lu, Z.; Nozik, A. J. *Applied Physics Letters* **1996**, *68*, 3150.

(15) Fu, H.; Zunger, A. *Physical Review B* **1997**, *56*, 1496.

(16) Karel Čapek, R.; Moreels, I.; Lambert, K.; De Muynck, D.; Zhao, Q.; Van Tomme, A.; Vanhaecke, F.; Hens, Z. *The Journal of Physical Chemistry C* **2010**, *114*, 6371.

(17) Kamal, J. S.; Omari, A.; Van Hoecke, K.; Zhao, Q.; Vantomme, A.; Vanhaecke, F.; Capek, R. K.; Hens, Z. *The Journal of Physical Chemistry C* **2012**, *116*, 5049.

(18) Micic, O. I.; Curtis, C. J.; Jones, K. M.; Sprague, J. R.; Nozik, A. J. *The Journal of Physical Chemistry* **1994**, *98*, 4966.

(19) Song, W.-S.; Lee, H.-S.; Lee, J. C.; Jang, D. S.; Choi, Y.; Choi, M.; Yang, H. *Journal of Nanoparticle Research* **2013**, *15*, 1750.

(20) Xie, R.; Battaglia, D.; Peng, X. *Journal of the American Chemical Society* **2007**, *129*, 15432.

(21) Tessier, M. D.; Dupont, D.; De Nolf, K.; De Roo, J.; Hens, Z. *Chemistry of Materials* **2015**, *27*, 4893.

(22) Talapin, D. V.; Gaponik, N.; Borchert, H.; Rogach, A. L.; Haase, M.; Weller, H. *The Journal of Physical Chemistry B* **2002**, *106*, 12659.

(23) Li, L.; Reiss, P. *Journal of the American Chemical Society* **2008**, *130*, 11588.

(24) Talapin, D. V.; Haubold, S.; Rogach, A. L.; Kornowski, A.; Haase, M.; Weller, H. *The Journal of Physical Chemistry B* **2001**, *105*, 2260.

(25) Ithurria, S.; Talapin, D. V. *Journal of the American Chemical Society* **2012**, *134*, 18585.

(26) Cui, J.; Beyler, A. P.; Marshall, L. F.; Chen, O.; Harris, D. K.; Wanger, D. D.; Brokmann, X.; Bawendi, M. G. *Nature Chemistry* **2013**, *5*, 602.

(27) Klimov, V. I. *Annual Review of Physical Chemistry* **2007**, *58*, 635.

(28) Guzelian, A. A.; Katari, J. E. B.; Kadavanich, A. V.; Banin, U.; Hamad, K.; Juban, E.; Alivisatos, A. P.; Wolters, R. H.; Arnold, C. C.; Heath, J. R. *The Journal of Physical Chemistry* **1996**, *100*, 7212.

(29) Dworak, L.; Matylitsky, V. V.; Breus, V. V.; Braun, M.; Basché, T.; Wachtveitl, J. *The Journal of Physical Chemistry C* **2011**, *115*, 3949.

(30) Wu, K.; Song, N.; Liu, Z.; Zhu, H.; Rodríguez-Córdoba, W.; Lian, T. *The Journal of Physical Chemistry A* **2013**, *117*, 7561.

(31) Adam, S.; Talapin, D. V.; Borchert, H.; Lobo, A.; McGinley, C.; de Castro, A. R. B.; Haase, M.; Weller, H.; Möller, T. *The Journal of Chemical Physics* **2005**, *123*, 084706.

(32) Mićić, O. I.; Nozik, A. J.; Lifshitz, E.; Rajh, T.; Poluektov, O. G.; Thurnauer, M. C. *The Journal of Physical Chemistry B* **2002**, *106*, 4390.

(33) Langof, L.; Ehrenfreund, E.; Lifshitz, E.; Micic, O. I.; Nozik, A. J. *The Journal of Physical Chemistry B* **2002**, *106*, 1606.

(34) Groeneveld, E.; de Mello Donegá, C. *The Journal of Physical Chemistry C* **2012**, *116*, 16240.

(35) Cui, J.; Beyler, A. P.; Coropceanu, I.; Cleary, L.; Avila, T. R.; Chen, Y.; Cordero, J. M.; Heathcote, S. L.; Harris, D. K.; Chen, O.; Cao, J.; Bawendi, M. G. *Nano Letters* **2016**, *16*, 289.

(36) Lim, J.; Bae, W. K.; Park, K. U.; zur Borg, L.; Zentel, R.; Lee, S.; Char, K. *Chemistry of Materials* **2013**, *25*, 1443.

(37) Zhang, H.; Kurley, J. M.; Russell, J. C.; Jang, J.; Talapin, D. V. *Journal of the American Chemical Society* **2016**, *138*, 7464.

(38) Yu, W. W.; Qu, L.; Guo, W.; Peng, X. *Chemistry of Materials* **2003**, *15*, 2854.

3. Characterization of lattice disorder in InP nanocrystals

Adapted with permission from E.M. Janke, N.E. Williams, C. She, D. Zherebetskyy, M.H. Hudson, L. Wang, D.J. Gosztola, R.D. Schaller, B.Lee, C.Sun, G.S. Engel, and D.V. Talapin, *"Origin of Broad Emission Spectra in InP Quantum Dots: Contributions from Structural and Electronic Disorder",* J. Am. Chem. Soc. 2018, 140, 46, 15791-15803. Copyright 2018 American Chemical Society.

3.1. Introduction

As described in the previous chapter, InP quantum dots show persistently broad emission and unusually broad absorption of selected sub-populations of emitters. The outcome of linear and pump-probe spectroscopic investigations was a hypothesis regarding the relationship between the nature of emission from passivated InP colloids and structural disorder within the colloidal particles. The increase in Stokes shift observed upon ZnS shelling or HF treatment could either originate from fast hole trapping and a "band to trap" type emission or from an increased degree of excited state reorganization resulting in effectively higher exciton phonon coupling in the band to band emission.[1] In the case of fast trapping, the relationship between surface chemistry and Stokes shift could be explained by a hypothesis that PL enhancing treatments work by introducing a new radiative recombination route through states that are related to the chemical modification of the structure. If the emission redshift is from a large geometric reorganization in the excited state and a correspondingly large Huang-Rhys parameter, the effect of chemical modification may be to alter the deformation potential of the structure, perhaps by "softening" the crystal surface and introducing new geometric motions that couple to the electronic excitation. The importance of soft deformations in lead salt quantum dots has been highlighted previously.[2,3] Because the electron is long-lived in a delocalized state (Section 2.6), we should then consider that excited state geometric distortion will be most likely related to distortion of the lattice centered around a localized hole.

The purpose of this chapter is to follow up on the spectroscopic studies by thoroughly characterizing the degree of lattice disorder in colloidal InP quantum dots as it relates to their utility as light emitters.

3.2. Raman spectroscopy as a sensitive probe of symmetry reduction in nanocrystals

To clarify the role of phonon coupling and lattice dynamics on the properties of InP quantum dot emission, a Raman scattering study was undertaken. Analysis of the spectral

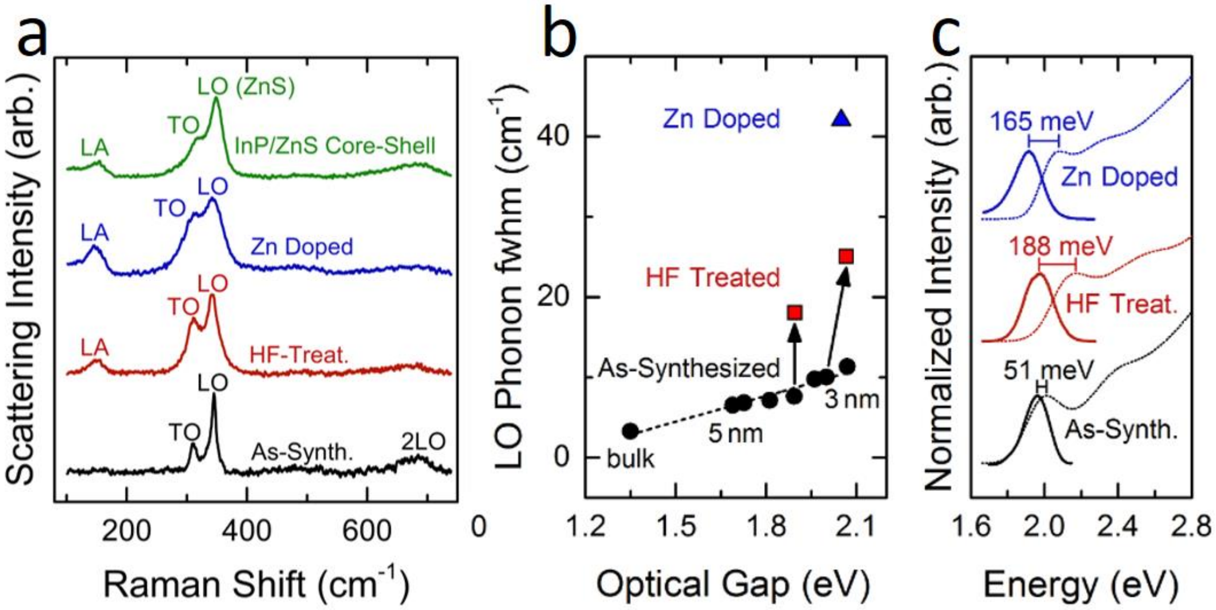

Figure 3-1: a. Raman spectra of InP as-synthesized, with post synthetic HF treatment, and Zn doped from synthesis. Zn-doped and HF treated material both show broadening of the optical phonon features as well as appearance of scattering from the longitudinal acoustic (LA) mode. **b.** A comparison of the LO phonon linewidths for the undoped, as-synthesized material and for HF treated and Zn doped material. HF Treatment and Zn doping by inclusion of $ZnCl_2$ in the synthesis both account for a significant portion of the spectral broadening at a given size and optical gap. Black arrows connect measurements for the same material out of synthesis and after the post synthesis treatment with HF. **c.** Absorption spectra of the three classes of InP and PL under 2.8 eV excitation. Large apparent Stokes' shifts are correlated with the lattice disorder related broadening seen in the Raman spectra and also with PLE spectra which show little narrowing compared to ensemble absorption.

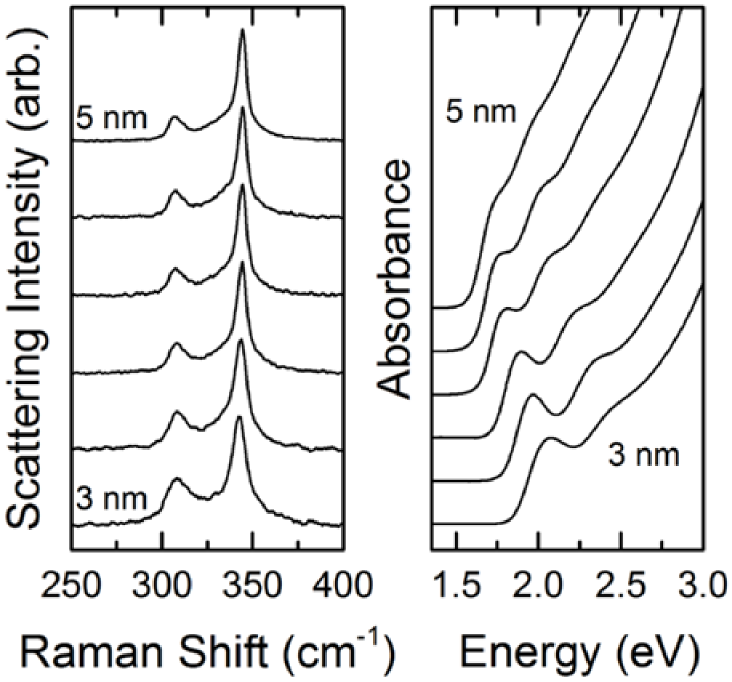

Figure 3-2: The effect of finite crystallite dimensions on Raman lineshape: Left, Raman spectra showing the optical phonon region for a size series of as-synthesized InP nanoparticles with average diameters ranging from 5nm to 3nm. Right, absorbance spectra corresponding to the same series of samples.

lineshapes and overtone intensities reveals that InP samples with broad PLE spectra and bright, redshifted emission are also characterized by broadened features in their Raman spectra (Figure 3-1). I further argue that this broadening is not due to size effects, surface reconstruction, or appearance of impurity phases. Rather, the broadened Raman features of InP/ZnS core-shells and aerobically HF treated InP are derived from internal lattice defects. The resulting reduction of crystal symmetry and associated effects on the electronic structure of the quantum dots are responsible for the changes to the Raman spectra and their behavior as emitters.

3.3. Assignment of features in nanocrystal Raman spectra

Poorly luminescent InP with no post synthesis modification shows a Raman spectrum that resembles that of bulk single crystals albeit with a size dependent broadening (Figure 3-2). The Γ–valley longitudinal optical (LO) and transverse optical (TO) phonon resonances are assigned to the

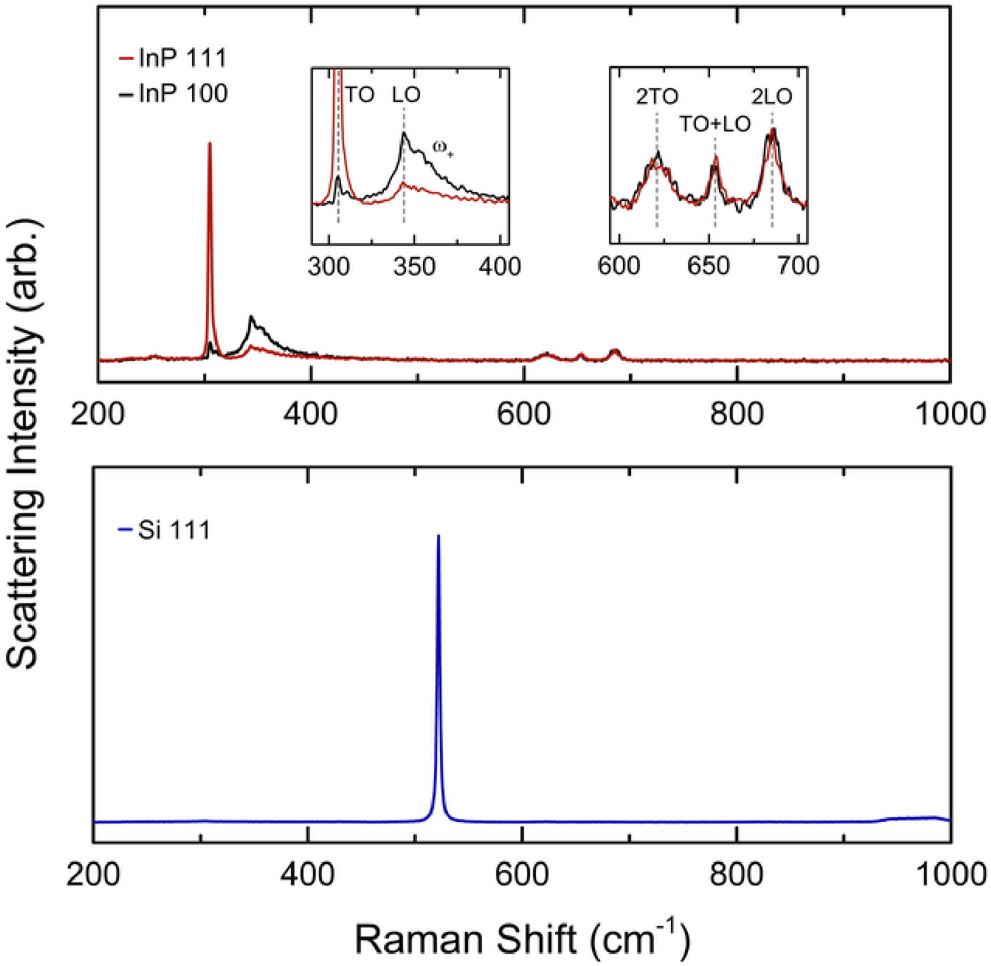

Figure 3-3: Backscattering geometry Raman measured on InP single crystals at 473 nm excitation. Top, data for two different crystallographic orientations of InP, p-type doped at 5*10^{17} Zn atoms cm^{-3}. The left and right insets show the fundamental and first overtone scattering features respectively. Transverse optical (TO), longitudinal optical (LO) and their overtones are observed. Phonon polariton scattering is also seen in the form of a broad peak centered at 355 cm^{-1} and labeled as ω_+. Bottom, the Raman spectrum of the Silicon wafer used as a substrate for the nanocrystal Raman experiments. The single characteristic peak near 520 cm^{-1} was not observed in spectra of deposited nanocrystals. This ensures that nanocrystal spectra are not convoluted with background signals from the substrate.

two prominent resonances around 310 cm^{-1} and 340 cm^{-1} respectively. At higher frequencies, spectra show an indistinct feature that can be attributed to three overtones, 2TO, TO+LO, and 2LO. These three features are well resolved for single crystal InP (Figure 3-3) but produce a single broad scattering signal in the nanocrystalline samples.

Raman measurements were also made on luminescent chemically passivated InP samples. InP cores shelled with ZnS show a resonance at 350 cm^{-1} which corresponds to the LO phonon frequency of ZnS and which appears to overlap with the InP LO phonon resonance and obscure it (Figure 3-1a). I analyze the InP/ZnS core-shell system further by also considering "Zn-doped" InP. For ZnS shelling of InP, it is a common practice to include a Zn precursor in the original InP core synthesis mixture. Unshelled InP quantum dots grown from a mixed metal precursor of $InCl_3$ and $ZnCl_2$ are termed here Zn-doped InP. The red shift of PL spectra observed in for Zn-doped InP is very similar to that in InP/ZnS core-shells and aerobically HF treated InP quantum dots (Figure 3-1c). Chemical analysis by ICP (Table 3-1) finds that for our growth conditions with a 1:1 molar ratio of In:Zn, the final atomic ratio is 21:1. Raman spectra of as-synthesized, Zn doped and aerobically HF treated InP quantum dots are compared in Figure 3-1a.

	Undoped InP	Zn-Doped InP
In content (ppm)	119.68	69.42
Zn content (ppm)	-0.02± 0.03	1.88
Atomic ratio, In:Zn	N/A	21:1

Table 3-1: Elemental analysis of InP NCs. Results of inductively coupled plasma atomic emission spectroscopy (ICP-OES) for InP nanocrystals synthesized by reaction of metal chlorides and aminophosphines in oleylamine as the solvent and ligand.

For InP samples that are modified by HF phototreatment, ZnS shelling, or Zn doping, an additional low frequency mode appears centered at 150 cm^{-1}. Because it appears for both HF phototreated particles and for Zn doped material as well, it is highly unlikely that it can be attributed to a motion involving a specific impurity atom. If, for example, In–F bonds were to be responsible then the same should not be seen in the ZnS core–shells, if Zn–P bonds were the cause then HF treated particles with no Zn content should not show the peak in their Raman spectra. The possibility of oxidation resulting in modes from surface oxide phases such as In_2O_3, $InPO_4$ also

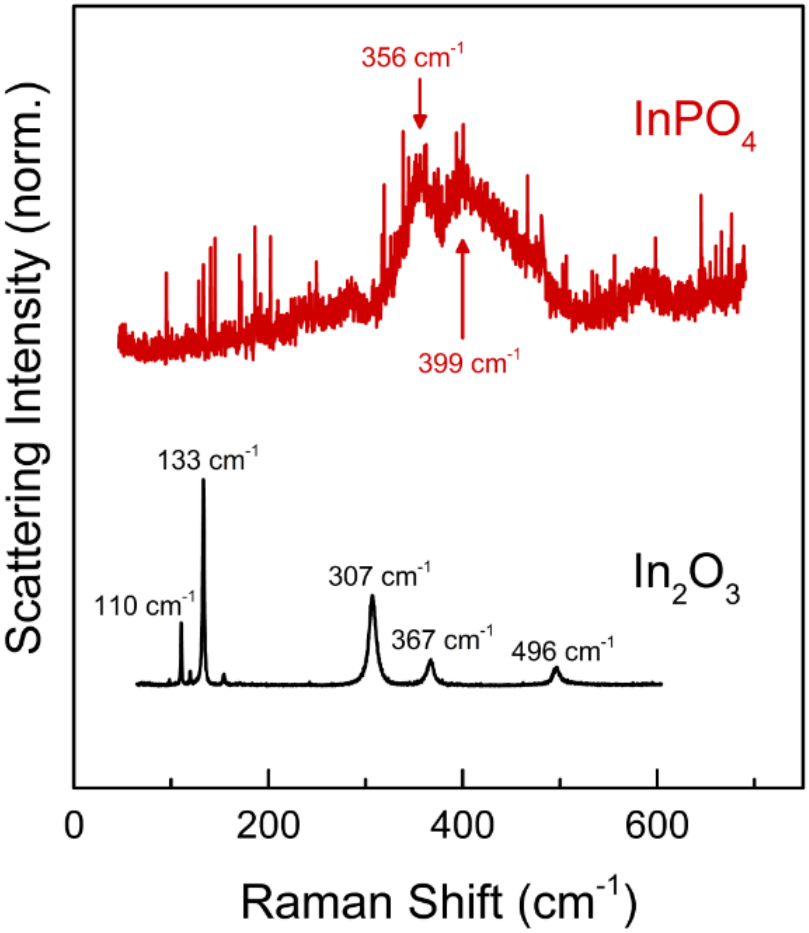

Figure 3-4: Raman scattering for bulk powder samples of the two dominant native oxides of InP, normalized and offset for clarity. The features of these spectra are not evident in any of the InP nanocrystal samples that were investigated. The fine lines in the $InPO_4$ sample spectrum are due to detection artifacting due to very low overall signal intensity, the broad feature with a double peak at 356 cm^{-1} and 399cm^{-1} is true signal from the sample.

fails to account for the observations as no Raman features found in the spectra of these oxides match 150 cm^{-1} peak seen from modified InP (Figure 3-4). Rather, the frequency of the new peak matches very well with that of longitudinal acoustic (LA) phonons of InP.[4]

The assignment of the low frequency feature around 150 cm^{-1} to scattering from longitudinal acoustic phonons has important implications. Inelastic scattering from acoustic phonons is not typically observed in nanocrystal samples and is not seen at very low frequencies in bulk crystals due to the acoustic phonon frequencies approaching zero at the Brillouin zone center. The acoustic phonon related feature in HF-phototreated or Zn-doped InP occurs at a frequency corresponding to the acoustic branch density of states maximum rather than near zero frequency[5]. The observed scattering must then be from the equivalent of non-Brillouin zone center modes. The translational symmetry of an ordered lattice imposes the requirement that one phonon scattering occur from phonons very near the Brillouin zone center in order to satisfy momentum conservation. Without translational symmetry considerations this selection rule does not apply as lattice motions will no longer be characterized by a definite wavevector.

Broadening of the Raman spectrum and appearance of scattering from modes far from the Brillouin zone center has been observed previously in bulk systems as a characteristic of lattice disorder. The effect of reduced lattice symmetry on Raman scattering is seen clearly in single crystal InP[6-8] and GaAs[6,9] with ion implantation induced disorder. Ion bombarded samples show pronounced broadening of the optical phonon resonances as well as appearance of new features. The new peaks originate from scattering involving the disordered material equivalent of what would, in the ordered case, be phonons that are far from the Brillouin zone center. In the limit of high disorder, the ion bombardment studies find a scattering intensity spectrum that closely resembles the total phonon density of states of the corresponding ordered material. The appearance of this “density of states–like” Raman spectrum indicates that a degree of lattice disorder that is sufficient to drastically alter Raman scattering behavior may not strongly perturb the phonon density of states.

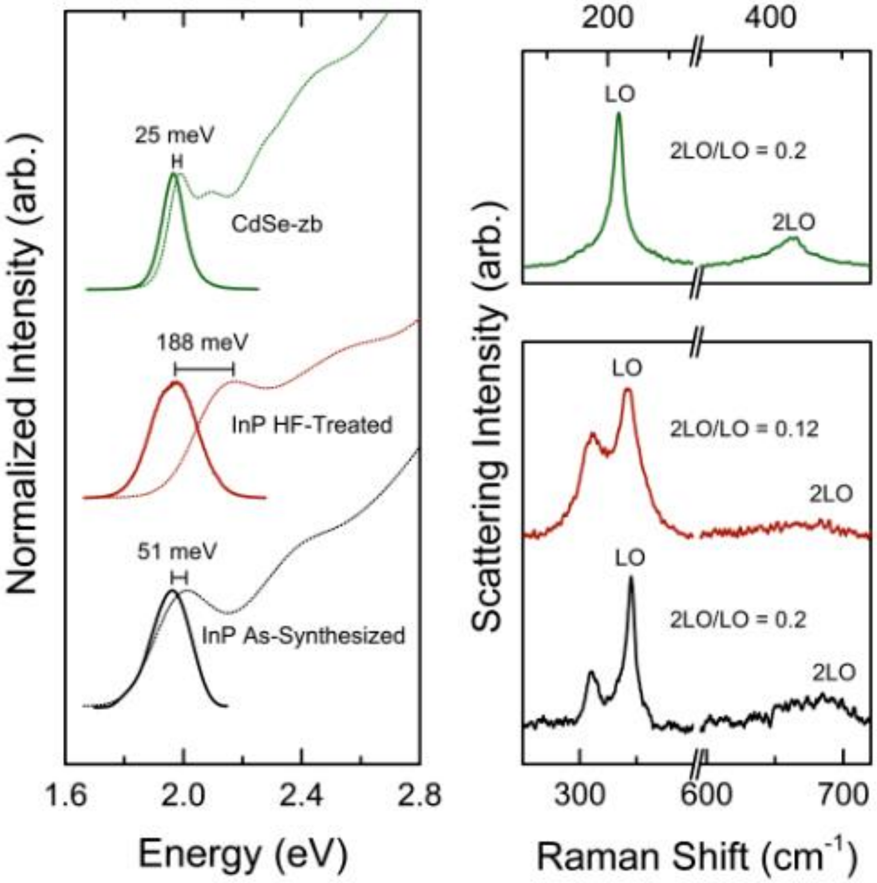

Figure 3-5: Raman overtone intensity analysis of InP and CdSe. Left, absorption and PL spectra of InP and CdSe nanocrystals. The InP sample that is made luminescent by HF treatment has a substantially greater apparent Stokes shift of 188 meV compared to either the InP as–synthesized or to the CdSe. Right, a comparison of Raman fundamental to first LO phonon overtone for the same samples.

3.4. Overtone analysis: competing roles of lattice order and Fröhlich coupling

This type of disorder related activation of non-Brillouin zone center Raman scattering seems to describe the spectra of luminescent nanoparticles quite well. Comparing untreated and aerobically HF treated InP, the Raman spectrum differs in four notable ways: The appearance of the LA phonon scattering feature, a relative increase in the intensity of the TO phonon peak, broadening of these features by a factor of two or more, and a lessening of the optical phonon overtone scattering intensity. All of these changes match those seen upon ion bombardment of single crystals including the weakened overtones. Concomitant with the shift to a density of states like Raman spectrum, ion bombardment disordered III-V materials exhibit a decrease in overtone intensities with increasing ion dose[8]. This provides a ready explanation for the weakening of overtone intensity seen when comparing luminescent HF photoetched InP particles to untreated particles of the same size (Figure 3-5). Rather than tracking strength of electron phonon coupling of the resonant excitation, the change to the overtone intensity indicates a reduced lattice symmetry.

Previous investigations[10-14] of Raman scattering from nanocrystals have attempted to correlate the optical phonon overtone to fundamental ratio to the Huang Rhys parameter (S) of the resonant excitation. Ideally, a more intense overtone in resonance Raman correlates with a larger value of S though more recent commentary[15,16] has pointed out the difficulty in rigorously extracting values of S by this method. Examination of the overtone strengths seen in InP spectra collected with different laser lines and from a variety of sample types reveals no clear relation of overtone intensity to linewidth or Stokes shift. The seeming lack of agreement between electron phonon coupling strengths predicted by resonance Raman and those predicted by a cursory analysis of emission and absorption spectra is with precedent however. Theoretical predictions[17] have posited that strong confinement of excitons should be accompanied by a weakened Fröhlich interaction due to decreased spatial separation of electron and hole. These claims were experimentally supported by resonance Raman measurements[10] which claimed that the Fröhlich interaction in nanoscale CdSe is weakened by an order of magnitude relative to bulk.

However, single particle linewidths of CdSe quantum dots increase with decreasing radius suggesting that the aggregate effect of vibrational broadening follows a trend counter to that predicted by optical phonon overtone analysis. A similar trend has been observed for InP nanoparticles. While phonon coupling from resonance Raman appears weaker with decreasing size[12], the Stokes shift and linewidths tend to systematically increase[18] with decreasing size. Figure 3-5 summarizes the point, overtone ratios for as synthesized InP and CdSe are quite comparable while luminescent HF treated InP gives a weaker overtone signal despite a much larger ensemble Stokes shift. Higher order Raman scattering requires a coherent lattice and, as discussed in the main text, the lower overtone frequencies of the treated, luminescent InP is due to lower effective crystallinity as seen in both Raman and powder x-ray diffraction and is not indicative of weak electron-phonon coupling.

3.5. Correlating the effects of lattice disorder on Raman spectra with powder x-ray diffraction measurements

The degree of disorder required to produce such a suppression of a selection rule is apparently relatively small. Measurements of powder x–ray diffraction (PXRD) of InP quantum dots as–synthesized, HF treated, or Zn-doped all yield very similar diffraction patterns (Figure S24). The PXRD peak widths and extracted Scherrer sizes for these different types of InP quantum dots are all comparable when comparing between particles with similar first exciton energy. Additionally, the PXRD data does not find evidence of impurity phases in any of the measured samples. We might expect to find InF_3, $InPO_4$, In_2O_3, or $In(PO_3)_3$ phases in material that is illuminated in the presence of HF and air but none are evident. Similarly, in Zn-doped InP there is no significant impurity phase of tetragonal Zn_3P_2. Only zinc blende InP is found, albeit with diffraction peaks shifted slightly to higher angles due to lattice contraction. Thus, the disorder

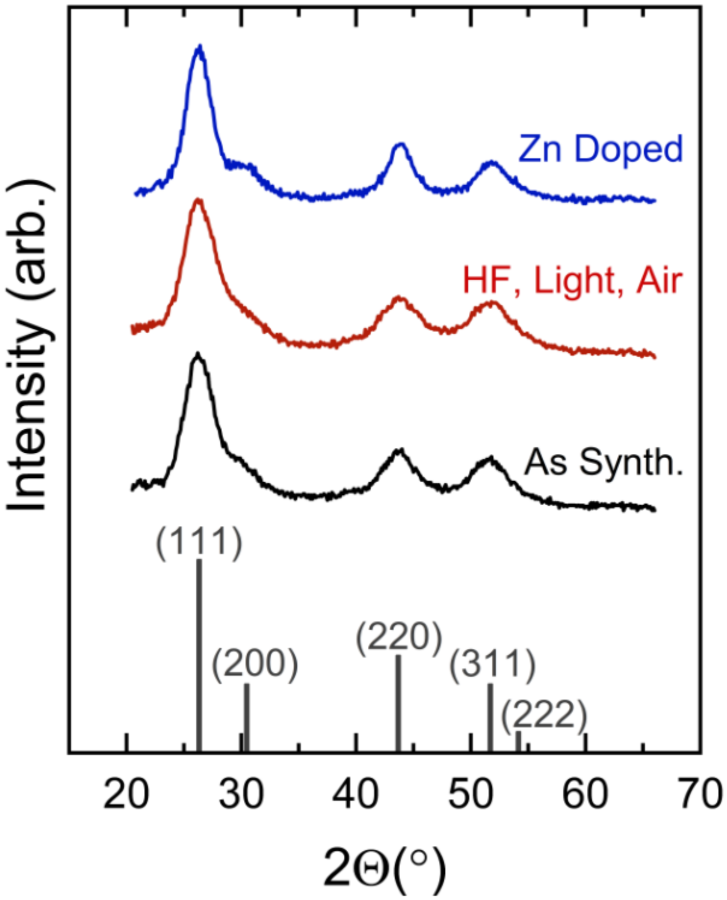

Figure 3-6: Powder x-ray diffraction data for three InP nanocrystal samples. Pure InP; as-synthesized, and post HF-treatment; and for InP doped with Zn from synthesis. In all samples, the evident diffraction peaks can be attributed to zincblende InP, there are no clear impurity phases.

observed in Raman spectroscopy likely originates from point defect sites such as vacancies, substitutions, and interstitials that result in an effectively reduced symmetry. A similar kind of disorder was seen in ion bombarded single crystals.[6-8]

In the case of a nanocrystal, even if perfectly ordered within, there is no translational symmetry comparable to a bulk single crystal where the lattice extends approximately infinitely. Typical colloidal InP quantum dots have diameters of 3 – 5 nanometers compared to a lattice constant of 0.59 nanometers. As structures approach the scale of a unit cell, it is important to carefully consider size effects in interpreting nanocrystal Raman scattering. A size series of InP

Raman spectra from material all from the same synthetic batch indeed shows the expected broadening of Raman features with decreasing crystal radius (Figure 3-2). Plotting the LO phonon linewidth vs. optical gap for this series gives an empirical linear relation shown in Figure 6b. Here it can be clearly seen that treatment by illumination in the presence of HF and air results in a broadening of the LO phonon line that is far greater than what can be attributed to size effects resulting from a reduction of the radius. The quantum dots doped with Zn show even larger LO phonon line broadening at the same size. In both cases, the Raman line broadening is accompanied by a pronounced increase in Stokes' shift of the emission (Figure 3-1c) pointing to a link between the vibrational properties of InP quantum dots and their properties as emitters. For Zn doped quantum dots the apparent reduction of lattice symmetry is easily understandable; Zn^{2+} ions incorporated at substitutional or interstitial sites are expected to introduce internal disorder. Phototreatment by HF on the other hand, is expected on the basis of previous studies[19-21] to act on the crystal surface.

This raises the question of whether the changes seen in Raman spectra of HF treated InP can be explained by surface effects alone or if there is an implied role of disorder in the interior of the quantum dots. In the case of a surface localized effect of the treatment, we should expect that surface phonon modes will be predominantly affected. Fitting of the optical phonon fundamental region reveals that the changes to the Raman seen upon treatment are best described as affecting the bulk derived TO and LO motions (Figure 3-7). The surface optical phonon (SO) scattering contribution is cleanly resolvable in the fits but does not show pronounced variation with chemical treatment. The center of this mode at 338 cm^{-1} corresponds exactly with the surface optical (SO) mode frequency previously observed by inelastic neutron scattering in bulk InP.[22]

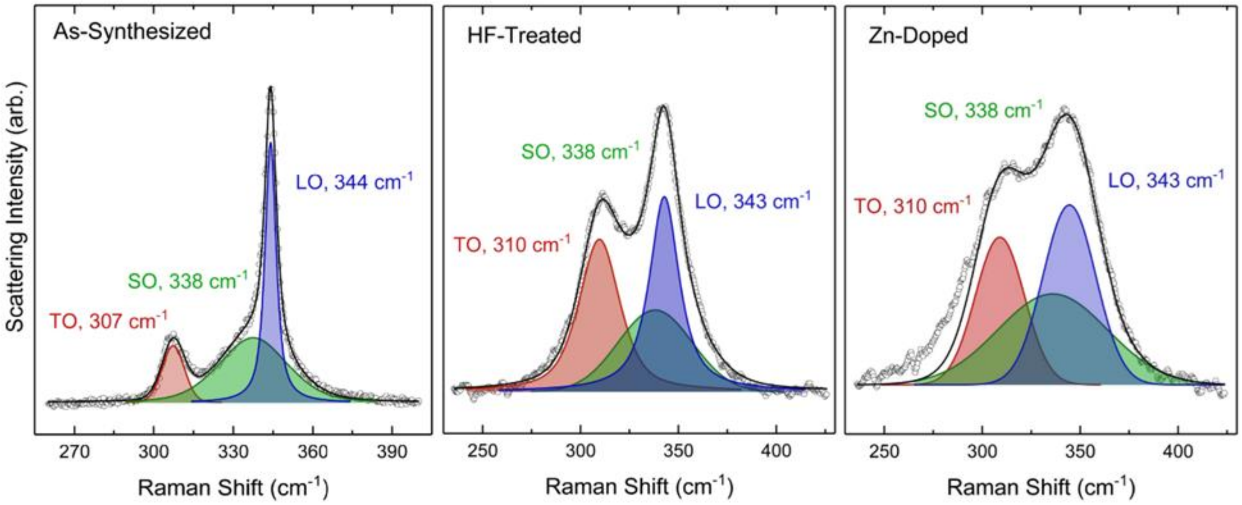

Figure 3-7: Raman spectra fitting of the optical phonon fundamental region of InP to pseudo-Voight functions. Fitted peaks are represented by shaded colored regions, data is shown as white circles, and the solid black line shows a sum of the fitted functions. At left, a spectrum for as-synthesized InP shows sharper resonances and a clear third feature assigned as a surface optical phonon appears at a frequency between that of the TO and LO phonons. Center, the broadened lineshape of HF treated InP is described by a sum of three features with broadening resulting predominantly from changes to the TO and LO phonon features. At right, the optical phonon spectrum of Zn-doped InP showing a high degree of broadening which can be described by many such three peak fits making extraction of the SO phonon scattering ambiguous.

The same fitting procedure for nanocrystals of InP treated with HF shows that the lineshape for the broadened spectrum can be decomposed into the same three features. While the SO phonon feature is similar in frequency and lineshape, the TO and LO modes both show a pronounced broadening. Both the line broadening and the relative increase in intensity of the TO phonon feature are seen in ion-bombarded bulk InP samples. This is consistent with the hypothesis that both Zn doping and HF treatment both result in changes to the Raman spectrum by their effects on the interior of the nanocrystals. This analysis implies that putative surface treatments affect vibrational structure of the quantum dots beyond the surface alone.

3.6. Identifying the chemical origin of lattice disorder in passivated InP

We gain insight into the way that luminescence enhancing modifications can result in defected nanocrystal interiors by reducing them to their component parts and examining the effects of each individually. In the case of ZnS shelling, the process can be broken down effects of Zn and S separately. When as-synthesized InP cores are stirred at 270°C with trioctylphosphine sulfide (TOP-S), the sulfur precursor for shell growth, there is little observable change in the Raman spectrum. A more aggressive sulfidation of the surface is possible by exchange of the long chain organic ligands as-synthesized InP for S^{2-} resulting in electrostatically stabilized colloids soluble in polar solvents. This ammonium sulfide treatment has been thoroughly investigated on surfaces of bulk InP where it has been found to induce surface reconstruction and alter surface electronic properties upon annealing.[23-26] Sulfide stabilized InP quantum dots show little change in the Raman spectrum even after a 350°C anneal. An analogous experiment to test the effect of surface Zn^{2+} yields a similar result: undoped InP cores that are exchanged to $ZnCl_2$ capping ligands also do not show significant broadening after annealing. Figure 7a summarizes these results and also shows Zn-doped InP capped with its native oleylamine ligands for comparison. The post-synthetic Zn^{2+} and S^{2-} treatments are both expected to have pronounced effects on the nanocrystal surfaces but likely not on the interior. So, the small effect of surface treatments on the Raman spectrum is consistent with the hypothesis that internal disorder is a necessary condition to observe broadened phonon lines. That only the Zn-doped material shows significant changes to its Raman spectrum is strong evidence that the signatures of disorder are related to internal defects.

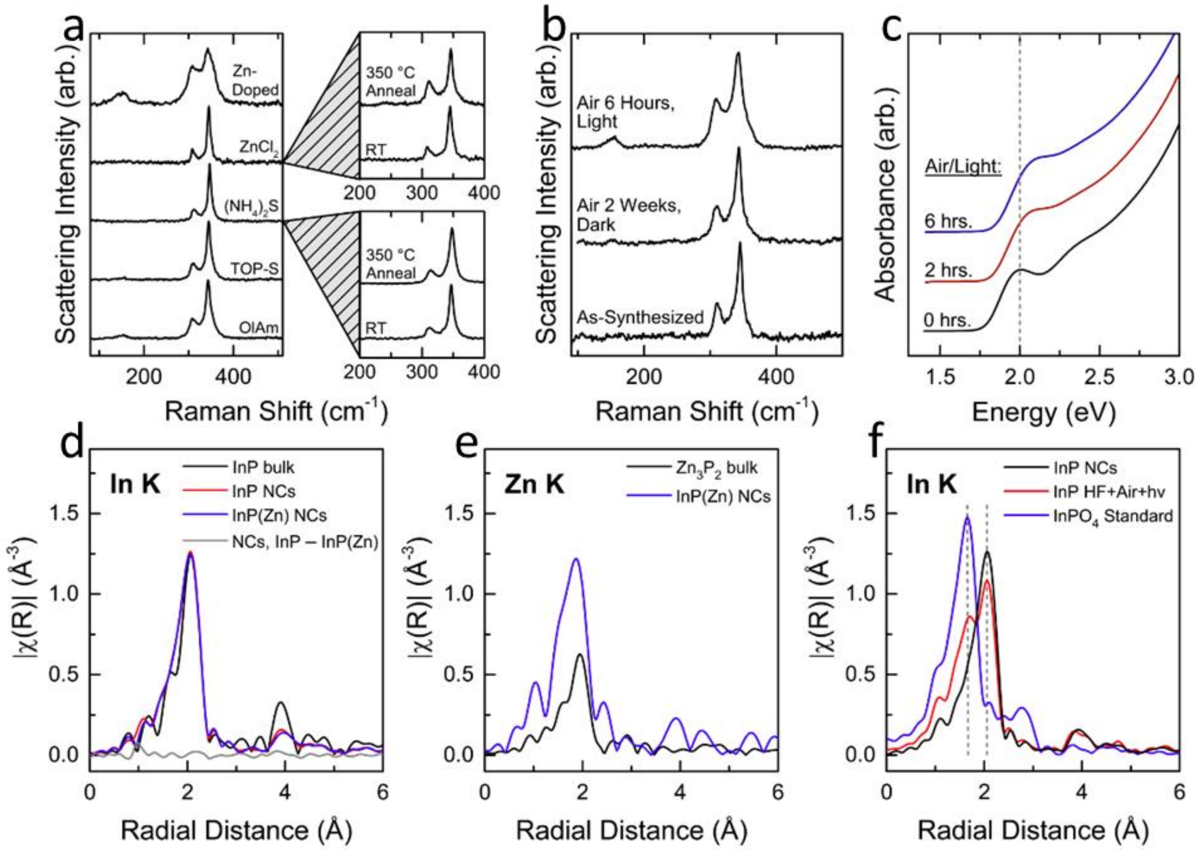

Figure 3-8: a. Raman spectra for as-synthesized InP cores capped with: native oleylamine ligands (OlAm), trioctylphosphine sulfide(TOP-S), ammonium sulfide, and zinc chloride. The Zn-doped spectrum shows data for oleylamine capped InP synthesized from a mixed $InCl_3$/$ZnCl_2$ precursor. **b.** Raman spectra showing the same particles fresh and exposed to air with and without light. **c.** Absorption spectra showing the effect of aerobic illumination of InP colloids. **d.,e.,f.** R-space representations of In and Zn K-edge EXAFS.

While InP passivation by dilute HF and illumination in air has been previously considered as a treatment which affects only nanocrystal surfaces, the fact that signatures of internal disorder appear in Raman spectra of treated InP implies that the effect goes beyond the surface. Separating the HF, illumination, and air exposure elements of the passivation, we find that disorder appears when InP is exposed to light and air simultaneously (Figure 3-8b,c). This can be explained by a hypothesis that photo-oxidation induces intercalation of interstitial O^{2-} ions into the lattice to

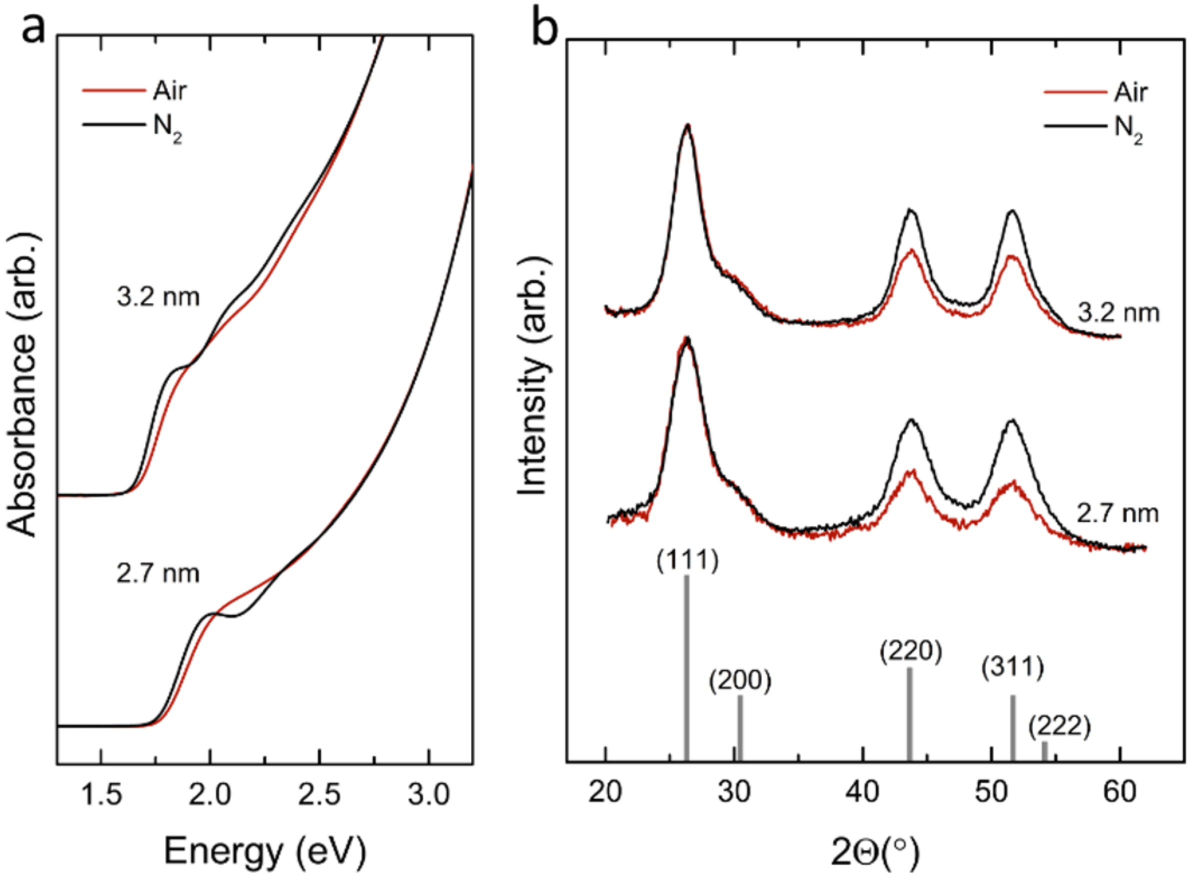

Figure 3-9: Effects of oxidation on absorption and x-ray diffraction of two sizes of InP NCs. At left, absorption spectra offset for clarity and taken using identical dilutions with toluene of the aged stock solutions show the effect of mild oxidation. At right, powder XRD data showing the suppression of diffraction from the (220) and (311) planes in samples that were stored in air.

produce a structural change that goes beyond the surface. This idea is consistent with previous observations of photooxidation of InP nanowires[27] and supported by a computational study[28] which found that oxygen atoms favorably insert into the InP lattice to form In-O-P bridges.

Effects of oxidation on absorption and diffraction were tested further by making these measurements on pairs of identical InP samples where one member of a pair was stored under inert gas and the other in ambient air (Figure 3-9). Two samples of InP nanocrystals with different average diameters were stored for two weeks in foil wrapped glass vials in a nitrogen filled glove box (N_2) or in air. Samples stored in air were pipetted as 2mL of 20 mg/mL toluene solution into new air filled 4mL glass vials (leaving 2mL air in the headspace) and sealed. The same treatment was used but with nitrogen gas filling the headspace for the samples stored in the glovebox. Comparison of absorption data (Figure 3-9a) shows that excitonic transitions become less distinctly defined for the samples exposed to air while samples stored in nitrogen show no change in absorption relative to the new unaged particles. I have found that samples stored in the dark in a nitrogen filled glovebox are stable for at least a year against changes to the absorption spectra. Powder x-ray diffraction measurements (Figure 3-9b) show a marked suppression of diffraction from the (220) and (311) lattice planes. This observation was reproducible for multiple batches and sizes of InP nanocrystals. To exclude preferred orientation effects, samples for XRD were prepared by precipitating the toluene dispersions using methanol, removing supernatant, drying and applying the dry powder to clean silicon substrates. The resulting samples gave diffraction rings that were completely isotropic and independent of sample orientation when rotated around the vertical axis. It should be noted here that samples that were simply dropcasted from the toluene dispersion onto the silicon substrates and dried also showed the same isotropic diffraction rings and the same suppression of the (220) and (311) diffractions. I interpret this to mean that significant preferred orientation effects are absent for both methods of sample preparation and that the changes to the XRD pattern of oxidized material is due to an internal reconstruction of the oxidized particles.

3.7. Extended x-ray absorption fine structure (EXAFS) for further evaluation of lattice disorder

Studies of Zn-doped and HF-treated InP by extended x-ray absorption fine structure (EXAFS) corroborate the assignment of lattice disorder inducing species inferred by the Raman study (Table 3-2, Table 3-3). I present evidence for substitutional Zn^{2+} ions on In^{3+} sites in

Sample	P coord. #	O coord. #	In coord. #	In-P length	In-O length	In-In length	R (fit quality)	R-range (Å)	k-range
InP (bulk standard)	4 (set)		12 (set)	2.546 ± 0.004		4.17 ± 0.01	0.011	1.2 – 5.4	2 – 11
In_2O_3 (bulk standard)		6 (set)	3 (set)		2.167 ± 0.005	3.314 ± 0.008	0.004	1.0 – 4.3	2.5 – 13.2
InP(Zn)	4.4 ± 0.2		10 ± 4	2.520 ± 0.003		4.18 ± 0.02	0.008	1.0 – 5.5	2.8 – 12.5
InP_TOP	4.5 ± 0.2		9 ± 3	2.533 ± 0.005		4.18 ± 0.02	0.010	1.0 – 4.5	2.8 – 11.8
InP_OlAm	4.4 ± 0.2		9 ± 3	2.525 ± 0.004		4.18 ± 0.02	0.0097	1.0 – 5.2	2.8 – 12
InP_HF_hv_air	3.2 ± 0.6	2.2 ± 0.6	12 ± 6	2.528 ± 0.009	2.14 ±0.02	4.22 ± 0.04	0.013	1.1 – 5.3	2.4 – 13

Table 3-2: Materials parameters extracted from In K-edge (27.9399 keV) EXAFS. Of particular note here is that the local coordination environment around In atoms is unchanged between Zn-doped and un-doped InP nanocrystals. Also, the aerobically HF phototreated InP shows a significant degree of oxidation with 0.68 In-O bonds per In-P. This is consistent with the lattice symmetry reduction and oxygen intercalation inferred from the Raman scattering study.

Sample	P coord. #	O coord. #	Zn-P length	Zn-O length	R (fit quality)	R-range (Å)	k-range
ZnO (standard)		4 (set)		1.96 ± 0.01	0.015	1.0 – 4.8	4.3 – 12.5
InP(Zn)_041	4.7 ± 0.7		2.332 ± 0.015		0.015	1.0 – 3.5	3.0 – 8.5

Table 3-3: Materials parameters extracted from Zn K-edge (9.6586 keV) EXAFS. The analysis of the Zn atoms within a Zn-doped InP finds them to occupy 4-coordinate tetrahedral sites with phosphorous atom nearest neighbors. This supports the conclusions inferred from the Raman scattering study that these Zn atoms occupy internal lattice sites and are distinct from surface bonded Zn.

Zn-doped InP and interstitial O^{2-} in aerobically HF treated InP. Data from the In K-edge represented in R-space, Figure 3-8d, shows identical coordination environments around In atoms in both doped and undoped InP. This indicates that Zn-doped material retains a tetrahedral four phosphorous atom coordination environment around indium and that there is no evidence of reduction in crystallinity upon Zn doping. It further argues that Zn inside the quantum dots should be on substitutional rather than interstitial sites as interstitial Zn^{2+} would appear in the first coordination sphere of neighboring In atoms. Data from the Zn K-edge, Figure 3-8e, shows that Zn dopant atoms are characterized by bonds to phosphorous atoms in their first coordination spheres. If Zn were significantly concentrated on the surface of the material, we would expect to see evidence in EXAFS of short Zn-N bonds from coordination to the oleylamine capping ligands. This is not the case and the observed Zn coordination provides strong support for the conclusion of the Raman study: growth of InP in the presence of a Zn salt results in Zn trapped inside the crystallites. Examination of the indium K-edge data for aerobically HF treated InP, Figure 3-8f, finds further support for the conclusions of the Raman study. Compared to untreated InP, the luminescent material is oxidized and shows that a significant amount of In-O bonds form as a result of the treatment. Fitting this data by considering In-P and In-O scattering paths finds that there are roughly two In-O bonds for every three In-P bonds. Given the large number of oxygen atoms, it is unlikely that oxidation is confined only to the surface. In agreement with the hypothesis motivated by the Raman data, EXAFS shows that photo-oxidation of InP leads to intercalation of O^{2-} ions deep into the quantum dots.

3.8. Computational insights into effects of impurity atoms on electronic structure of InP quantum dots

Combined, the spectroscopic, EXAFS and Raman studies find that structural disorder in the form of impurity atom point defects are correlated with the appearance of broad redshifted emission. The question then remains, how do these structural defects alter the electronic and optical properties of the material? We see from our spectroscopic investigations that electrons remain in a delocalized $1S_e$ state on the timescale of emission and that non-radiative recombination results from hole trapping. Further, we find from the 2DES study that the redshifted radiative recombination in Zn-doped InP/ZnS core-shells occurs from a strongly LO phonon coupled state. Strong coupling to the LO motion of InP suggests a spatial separation of electron and hole in the emissive state. Given the long lifetime of delocalized electrons, the plausible explanation is that the redshifted and persistently broad emission occurs through a state with the hole localized in a defect atom related state that is ~100 meV above the valence band edge. To further address this hypothesis, a series of DFT calculations were undertaken by Dr. Danylo Zherebetskyy to whom I am grateful for the assistance and contribution on this project. Calculations were performed on a model nanoparticle with $In_{92}P_{68}$ core (~1.9 nm; In/P ratio 1.35). Surfaces were passivated with 72 fluorine atoms to provide a clean band gap with the density of electronic states (DOS) shown in Figure 3-10 with band gap energy $E_g = 0.92$ eV. Contour plots visualizing the three states nearest the band edges are shown in Figure 3-11 and corresponding state energies in Table 3-4. The magnitude of the band gap energy is underestimated here compared to experiment, hence the

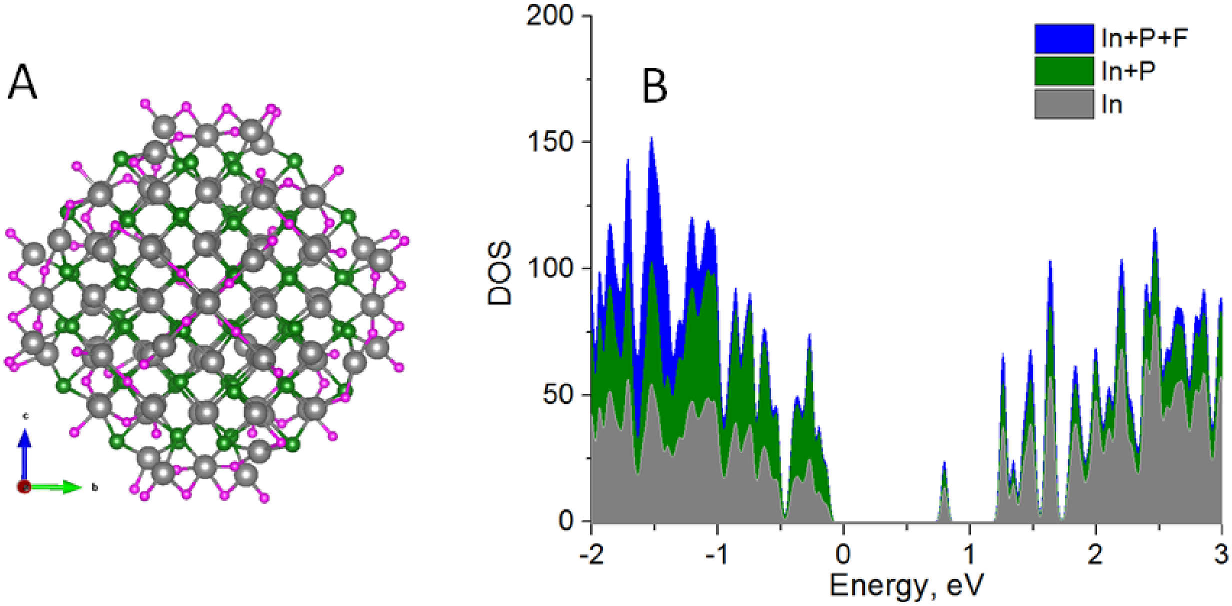

Figure 3-10: a) Ball and stick model of the fluorine terminated InP quantum dot used for modelling electronic structure with colored atoms showing In (Gray), P (green), and F (pink). **b)** Density of states plot for the modeled quantum dot. The colors here denote the types of atoms associated with the states at a given energy. While the conduction band is derived predominantly from In atomic orbitals, the valence band has a mixed P/In character.

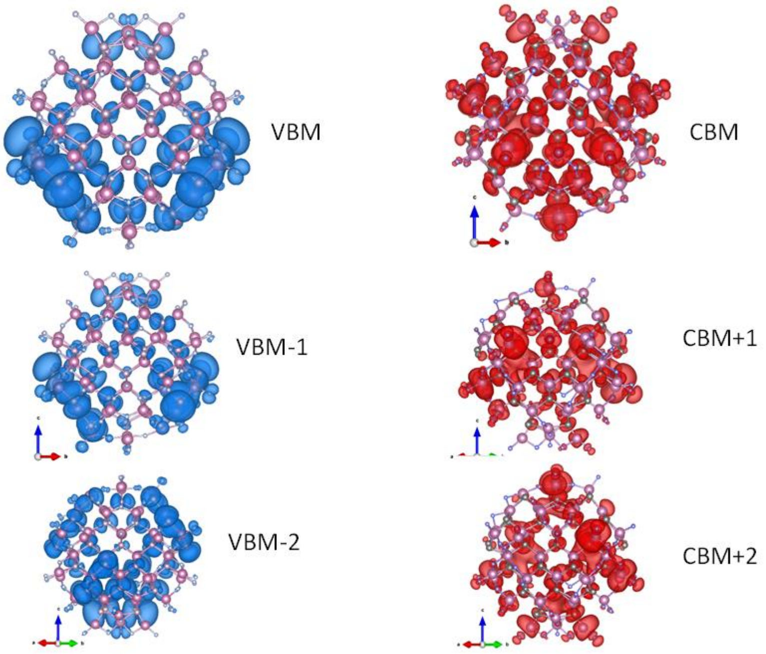

Figure 3-11: Visualization of band edge states in an InP quantum dot. Contour plots of the three states nearest the top of the valence band (blue, left) and the bottom of the conduction band (red, right) for a non-defected InP quantum dot model. The lowest conduction band state resembles the classical particle in a box type $1S_e$ envelope function while higher lying conduction band states are partially surface associated. All three valence band states shown here have a significant surface associated character and do not closely resemble the spherical harmonics expected for an ideally quantum confined semiconductor.

interpretation of the data focuses on comparing trends in electronic structure under changing surface passivation or introduction of defects. As an example, we found qualitatively similar electronic structure for $In_{92}P_{68}$ cores passivated with a mixture of acetate and hydroxyl ligands. This result supports our experimental findings that defect related emission seen for aerobically HF treated InP is not a result of surface fluorination but is caused by sub-surface defects that are introduced during the passivation process.

Interior Zn_{In} substitutions produce an additional form of electronic structure inhomogeneity. In addition to perturbing the valence band electronic structure, interior Zn dopants produce an in-gap-state (IGS) located above the VBM. As seen in the inset contour plot in

Structure model	Band Gap,eV	VBM-2, eV	VBM-1, eV	VBM, eV	IGS, eV	CBM, eV	CBM+1, eV	CBM+2, eV	CBM+3, eV
InP-F No Defects	0.9193	-5.5938	-5.5601	-5.5132		-4.5939	-4.1385	-4.1287	-4.1115
1Zn (11-1)edge(110)	0.9223	-5.5696	-5.5361	-5.4884		-4.5661	-4.1179	-4.1043	-4.0835
1Zn 3rdLayer	0.9644	-5.5644	-5.528	-5.4718	-5.4254	-4.5074	-4.0845	-4.0715	-4.0578
1Zn 2ndLayer	0.9282	-5.5719	-5.5167	-5.4499	-5.1831	-4.5217	-4.1019	-4.0974	-4.072
1Zn (111)corner(001)	0.9417	-5.582	-5.5489	-5.535		-4.5933	-4.1743	-4.132	-4.0877
1Zn (001)middle	0.9042	-5.5801	-5.5617	-5.5062		-4.602	-4.1838	-4.1407	-4.0718
1Zn (11-1)corner(001)	0.9124	-5.564	-5.5347	-5.4868		-4.5744	-4.2135	-4.1073	-4.0972
1Zn (111)corner(001)	0.9034	-5.5233	-5.5073	-5.4555		-4.5521	-4.0989	-4.0851	-4.0695
6Zn Surface	0.9598	-5.5711	-5.5631	-5.5134		-4.5536	-4.1577	-4.146	-4.1183

Table 3-4: Computed near band-edge state energies for InP quantum dots. The InP nanostructures are modeled with Zn atoms substituted for In at various surface and interior lattice sites. The two models with a Zn atom substitution at an interior site, marked as "1Zn 2nd layer" and "1Zn 3rd layer" show the presence of "in gap states" (IGS) above the valence band edge. The density profiles of these states are strongly associated spatially with the substituted Zn atom.

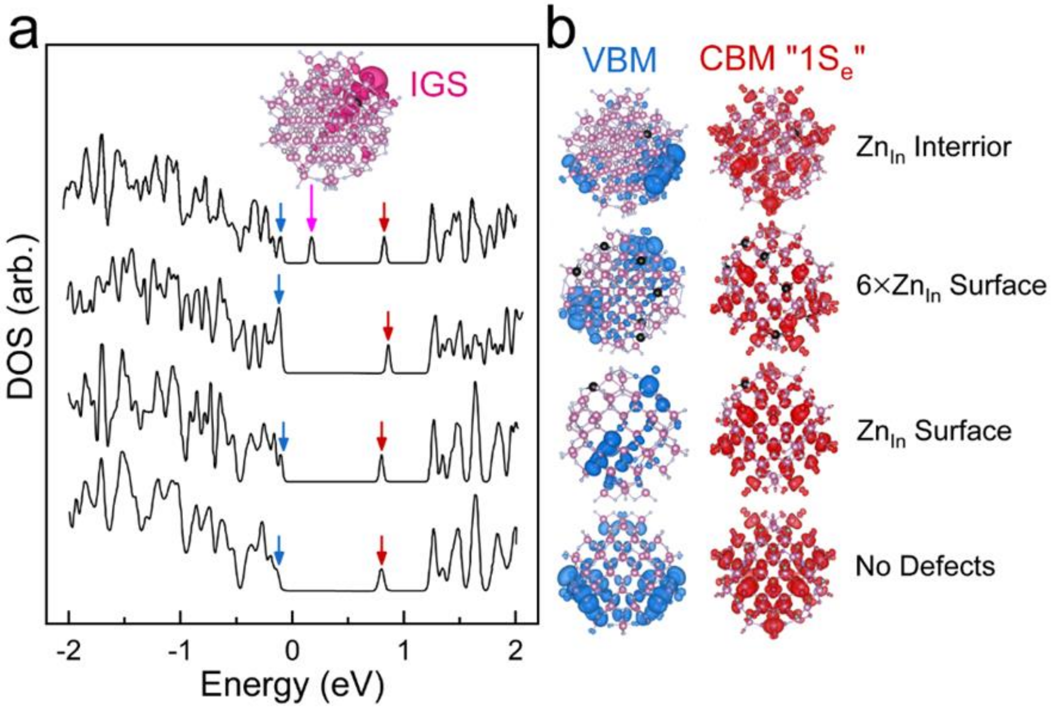

Figure 3-12: (a) Offset density of states traces calculated for In$_{92}$P$_{68}$ with the following substitutional Zn$_{In}$ defects from top to bottom: single interior Zn, 6 Zn atoms on surface, single Zn on surface, and no substitutions. The valence band maxima (VBM) and conduction band minima (CBM) are marked with blue and red arrows. The "in gap state" generated by the interior Zn substitution is marked with a magenta arrow and depicted on the inset contour plot. **(b)** Contour plots visualizing the VBM and CBM states marked by blue and red arrows in (a). Atoms are colored according to type: In(pink), P(grey), F(blue), and Zn(black).

Figure 3-12, this IGS has orbital density localized around the substituted Zn atom and an energy ranging between 50 – 250 meV above the VBM depending on the which interior In atom is substituted (Table 3-4). The appearance of such a state is expected given that Zn is a well-known p-type dopant used in commercial bulk InP wafers where it acts as an electron acceptor by introduction of a state above the valence band edge. For the purposes of quantum dot emitters, this variable energy IGS contributes further to broad ensemble emission by introducing a new radiative emission pathway. Following excitation of an electron-hole pair, the IGS can capture the hole, which subsequently recombines with the electron remaining in the $1S_e$ like CBM state. One effect of this CBM to IGS emission pathway can be to boost PL quantum yield by competing with non-radiative hole trapping at the quantum dot surface. Additionally, it provides an explanation for experimentally observed dot-to-dot variations of the apparent Stokes' shift and strongly phonon coupled emission.

3.9. Concluding remarks and future outlook on InP quantum dot emitters and the role of structural disorder on currently achievable performance

In summary, the data points to an important role of chemical disorder in the optical properties of InP quantum dots. The apparent Stokes' shift of the photoluminescence varies depending on chemistry suggesting that the electronic states that are active in emission also vary. Given that colloids with different emission redshift show similar properties as absorbers, this implies that the emission redshift is due to an electronic relaxation following absorption of bandedge light. Photoluminescence excitation spectra show that the deeply redshifted emission is coupled to a broad action spectrum with washed out features and with an absorption onset shifted substantially to the blue compared to the detected emission. Energy dissipation between absorption and emission in the form of electron relaxation to a sub-band edge state was ruled out by a series

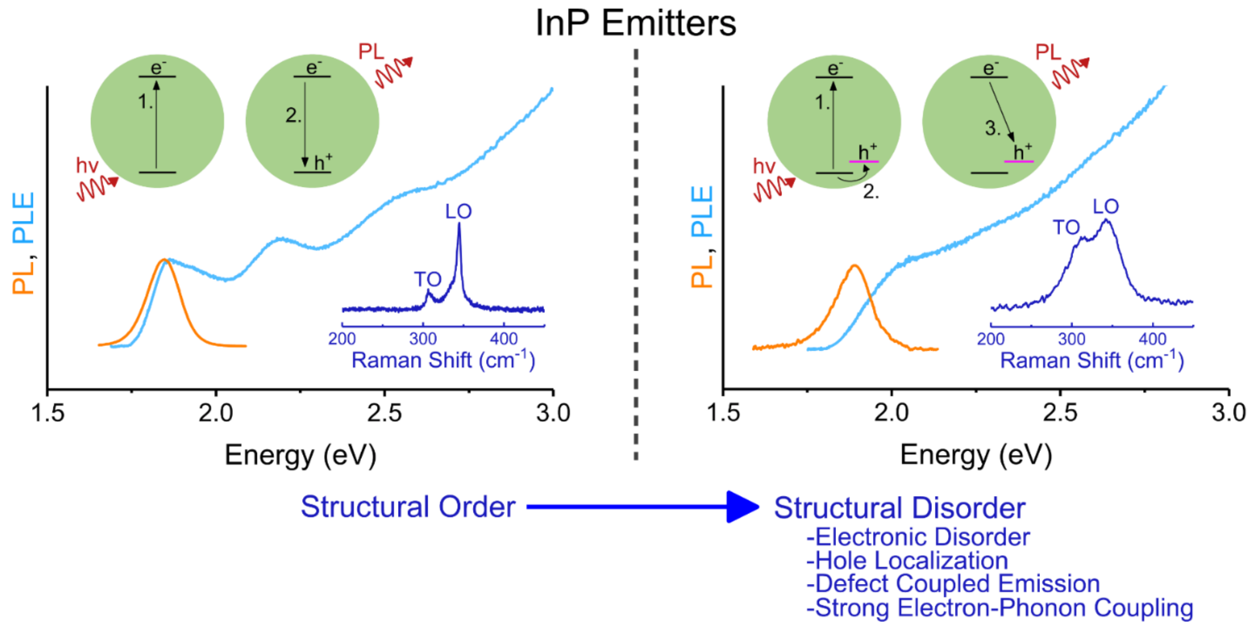

Figure 3-13: Summary of the conclusions of Chapters 2 and 3. The figure depicts ordered InP quantum dots on the left and disordered material with impurity atom coupled absorption and emission on the right. Energy level diagrams show the process of radiative recombination for each material, Raman spectra show the degree of broadening, and the PL and PLE spectra collected at the ensemble emission maximum show absorption and emission characteristics of sub-population of each sample.

of transient absorption experiments. There are two likely remaining mechanisms to explain the redshift. One is energy loss by shallow trapping of the valence band holes to a state which can combine radiatively with delocalized conduction band electrons. A second is a large geometric reorganization of the excited state resulting in large electron phonon coupling and emission to a vibrationally hot electronic ground state. However, the implications of the two mechanisms tend to converge as presence of one implies some role of the other. Shallow trapping is likely to be accompanied by an increased degree of localization of the hole which would result in a spatial separation between it and the delocalized electron. The resulting electric dipole induces a geometric distortion along the optical phonon coordinate of motion of the hole-trapped excited state. Thus, localization of the hole due to trapping can produce a stronger electron phonon coupling. Likely, the redshift in emission produced when InP nanoparticles are made brightly luminescent is due to a combination of the two effects which explains the persistently broad emission linewidth of typical high quantum yield InP samples. Raman experiments reveal disorder activated phonon modes and give us some clue as to the chemical nature of the lowered symmetry.

A common property of interstitial O^{2-}, S^{2-}, F^{-}, and substitutional Zn^{2+} is that all will be expected to p-type dope III-V semiconductors by charge balance arguments. In a quantum dot, the doping effect of such impurities is likely to be compensated by the presence of other point defects such as vacancies rather than by the presence of free holes. The net effect is then to produce filled states above the valence band edge that are expected to act as exactly the shallow hole traps implied by the luminescence and transient absorption experiments. The hypothesis consistent with all of the data is that the PL enhancing modifications of doping InP with Zn^{2+}, shelling with II-VI materials and etching with HF in aerobic conditions and illumination all play a double role of passivating surface sites and installing shallow hole traps. The radiative process combining free conduction band electrons with trapped holes then enhances PL quantum yield by providing an additional emissive recombination pathway competing with the expected band to band process. The end result is a redshifted and persistently broad emission profile that complicates efforts to apply InP colloidal quantum dots, for example, as phosphors emitting saturated primary colors. In detailing the obstacles to achieving narrow emitting, stable, and bright InP, we also hope to point toward a future direction to overcome them. InP quantum dots passivated by shells of higher bandgap III-V materials, an InP/InGaP/GaP type structure for example, should avoid the problem of emission through impurity atom related states. Developments in synthetic methods for the InP core that avoid oxidation during synthesis should also allow for a way to avoid oxide induced midgap states. With the correct synthetic protocol and passivation scheme, it should be possible for III-V based quantum dots to emit from band to band recombination with reduced phonon coupling. Future steps in this direction may prove necessary for achieving comparable performance to CdSe in nontoxic III-V materials.

3.10. Gallery of extended x-ray absorption fine structure spectroscopy (EXAFS) data

The images in this section depict R-space representations of experimental EXAFS data, along with fits used to extract the structural parameters reported in Table 3-2 and Table 3-3. The region of R-space used for defining the fit is noted also. Fitting was assisted by tools included in the Demeter software package, version 0.9.21, copyright Bruce Ravel, 2015.

<u>In K-edge fits (27.9399 eV):</u>

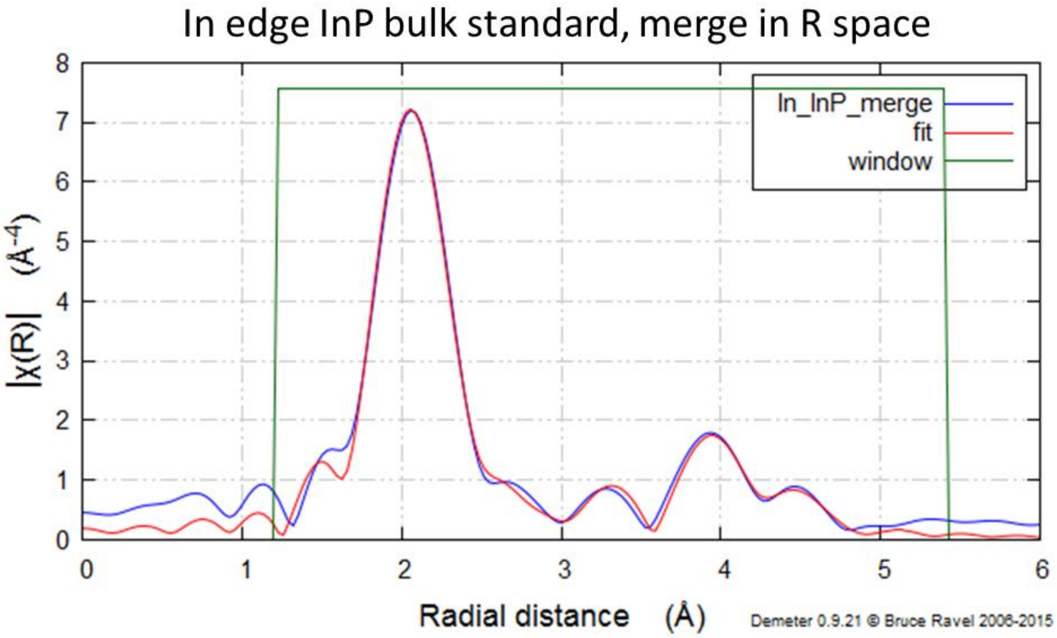

Figure 3-14: In K-edge fitting for the bulk, crystalline InP standard.

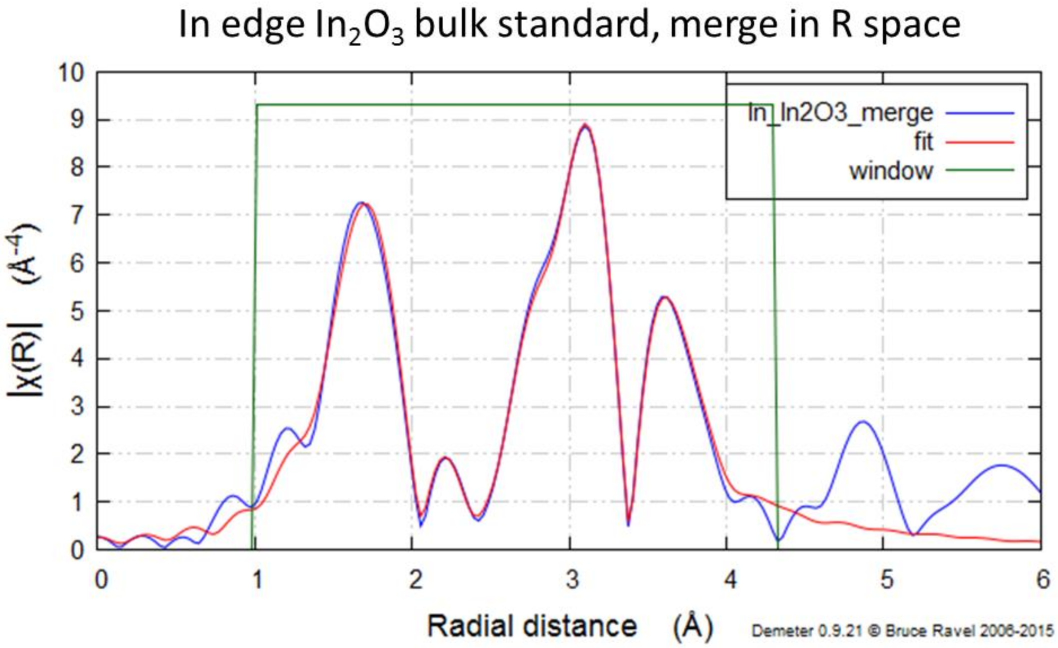

Figure 3-15: In K-edge fitting for the bulk, crystalline In_2O_3 standard.

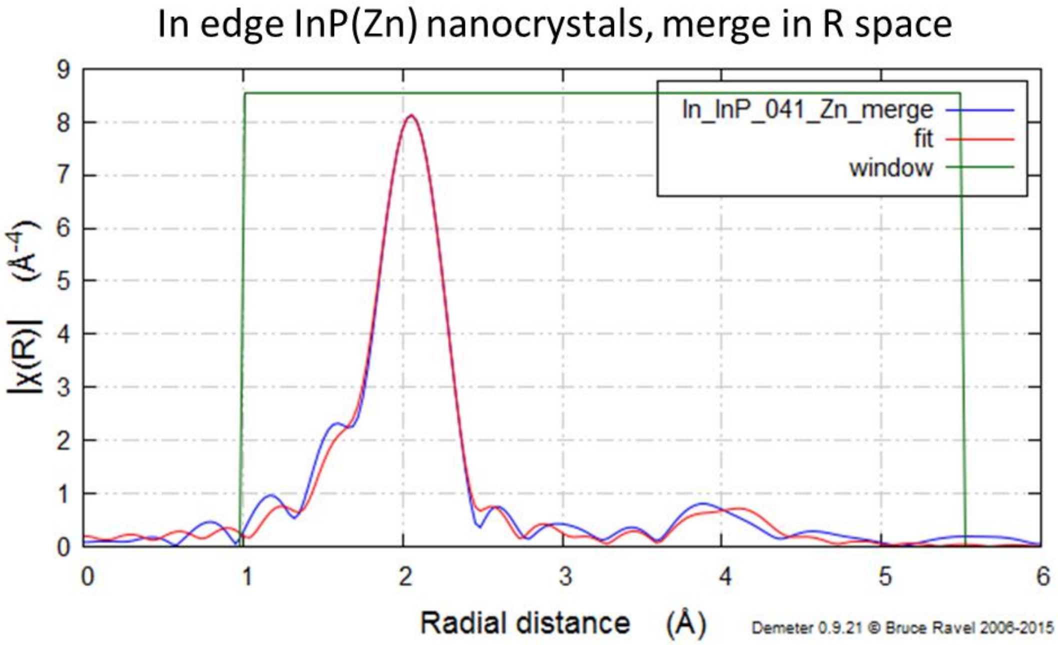

Figure 3-16: In K-edge fitting for Zn-doped InP nanocrystals.

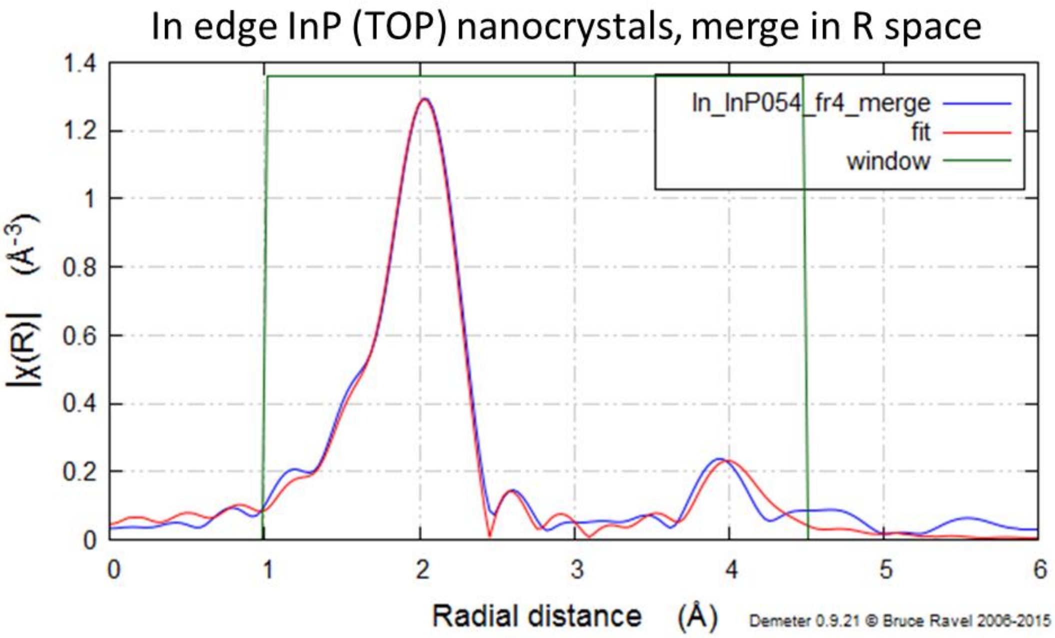

Figure 3-17: In K-edge fitting for undoped InP nanocrystals synthesized by dehalosilylation in TOP and TOPO as described the synthetic methods section in Chapter 2.

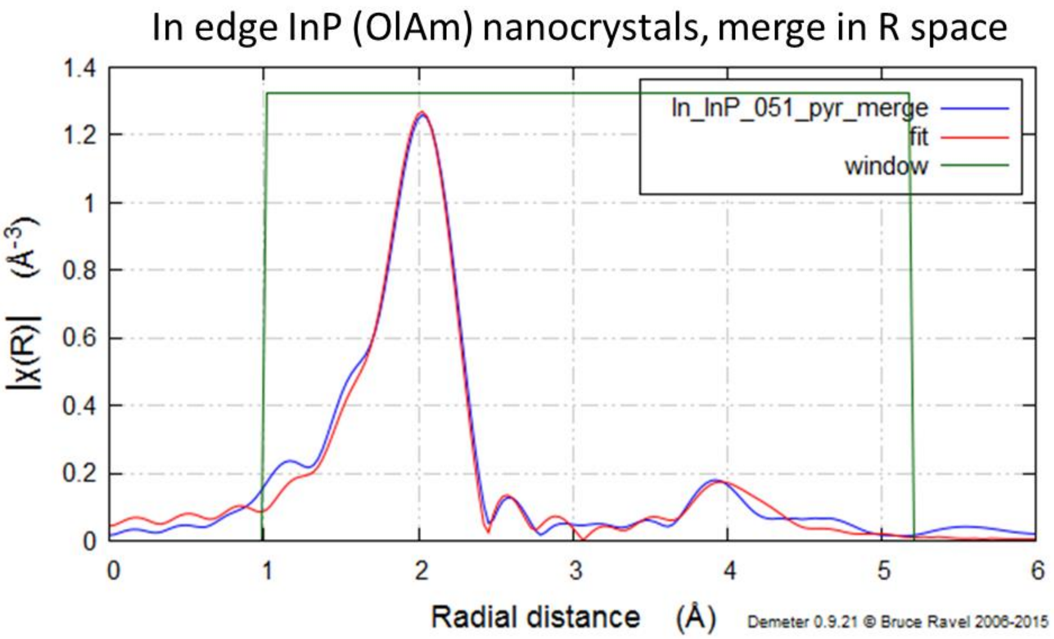

Figure 3-18: In K-edge fitting for undoped InP nanocrystals synthesized in oleylamine (OlAm) using tris(dimethylamino)phosphine as for the Zn-doped nanocrystals and the InP/ZnS core-shells but without doping or shelling.

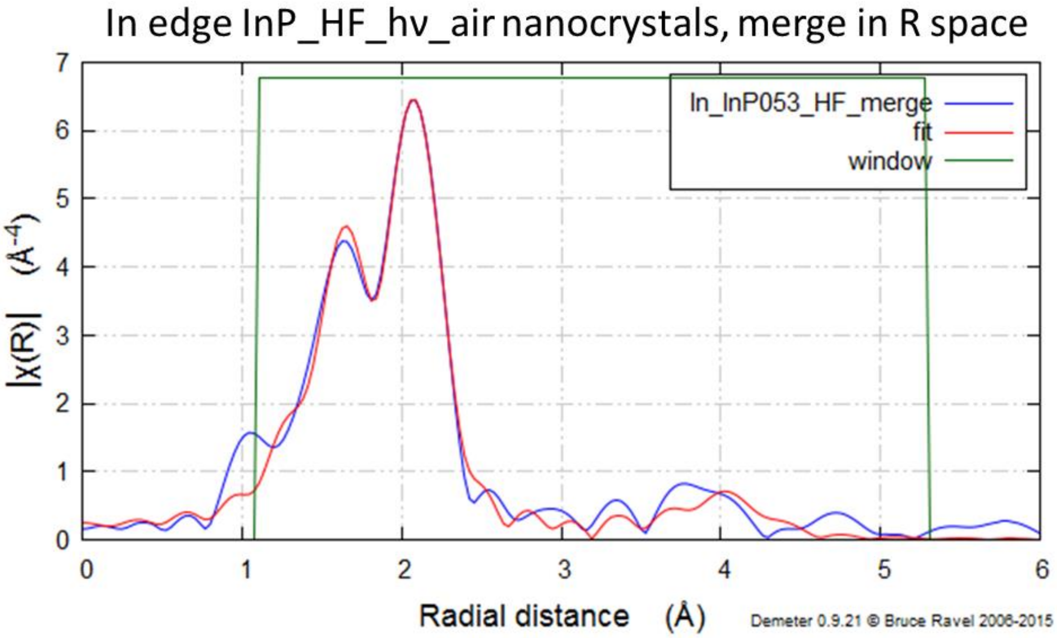

Figure 3-19: In K-edge fitting for InP nanocrystals after aerobic HF phototreatment.

Zn K-edge fits (9.6586 eV):

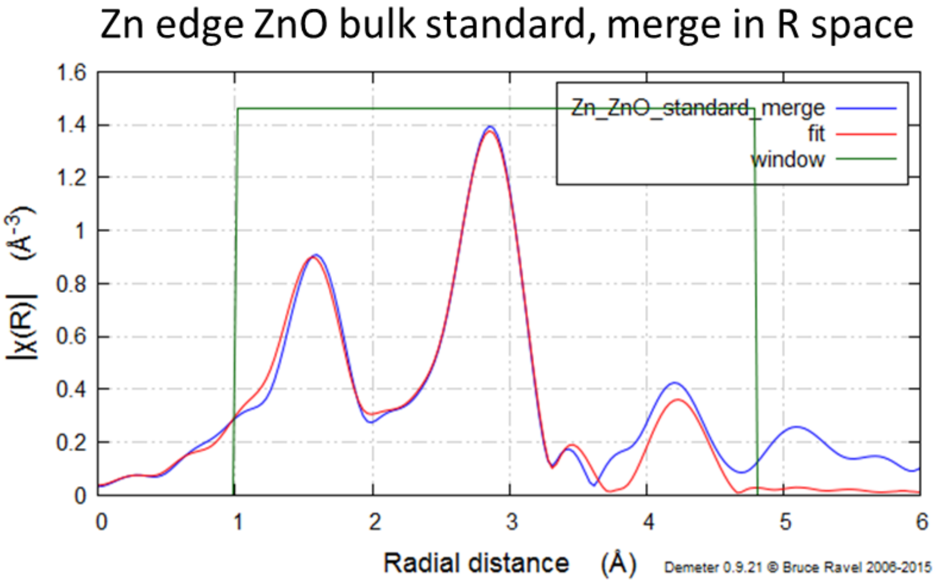

Figure 3-20: Zn K-edge fitting for the bulk, crystalline ZnO standard.

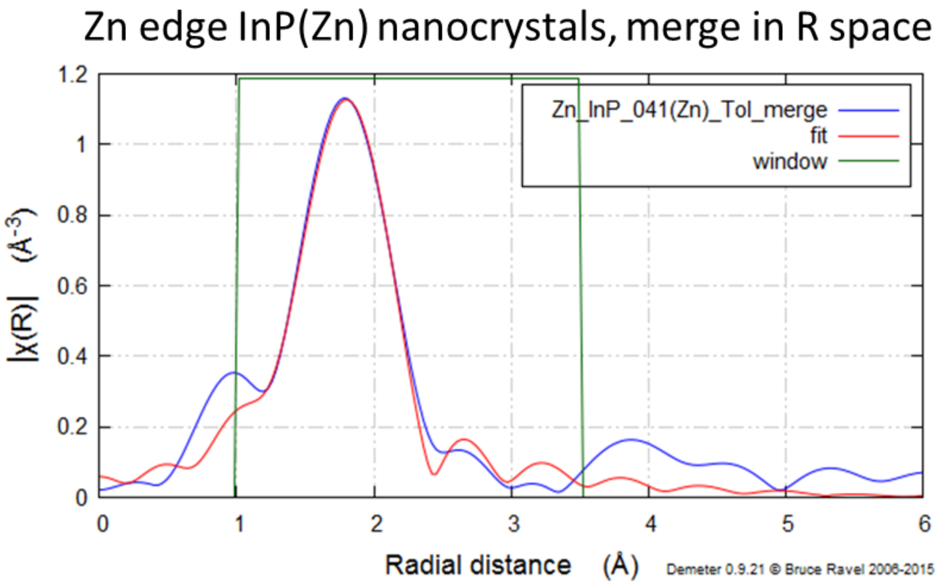

Figure 3-21: Zn K-edge fitting for Zn-doped InP nanocrystals.

3.11. Experimental Methods

Nanocrystal synthesis:

Colloidal nanomaterials were prepared following the same methods as detailed in Chapter 2 in Section 2.8 of this document (p. 49).

Raman spectroscopy:

Raman spectra were acquired on a Horiba LabRAM HR confocal Raman microscope with an Andor EMCCD detector. The instrument was calibrated daily to the 520 cm^{-1} Raman line of a silicon standard excited by the 623.8 nm line of HeNe laser. Spectra reported in the main text were acquired using a 473nm lasers. Samples were prepared by drop-casting nanocrystal colloids onto silicon substrates and measurements were made in backscattering geometry. For luminescent samples, a rising background due to sample fluorescence was corrected by baselining the data to a polynomial fit. Substrate background scattering was determined to be negligible by ensuring that the characteristic 520 cm^{-1} line of the crystalline Si substrate did not appear in the data.

Powder x-ray diffraction (PXRD):

Wide-angle powder x-ray diffraction (PXRD) data was acquired on a Bruker D8 diffractometer using a 1.541 Å Cu K-α source and a Vantec 2000 array detector. Nanocrystal samples were dropcast onto either crystalline silicon or sapphire substrates, and diffraction from these substrates was subtracted as background.

Elemental analysis by inductively coupled plasma atomic emission spectroscopy (ICP-OES):

Elemental analysis of nanocrystal samples was carried out by inductively coupled plasma optical emission spectroscopy on an Agilent 700 Series instrument. Nanocrystal samples were digested using 69.0% TraceSELECT grade nitric acid (Aldrich) and were diluted using ultrapure deionized water. For samples that did not dissolve completely in nitric acid, a small amount (500 ppm) of Br_2 (99.99% Aldrich) was added before dilution.

Extended x-ray absorption fine structure (EXAFS):

EXAFS measurements were collected at the Advanced Photon Source x-ray sciences division (XSD) beamline 20-BM at Argonne National Laboratory. Nanocrystal samples were measured as colloids in toluene and encapsulated in polypropylene cuvettes sealed under inert atmosphere. Bulk powder standards were prepared by milling polycrystalline compounds together with powdered hexagonal boron nitride as a diluent and cold pressing the mixture into a pellet which was then encapsulated in polyimide tape. Measurements at the In and Zn K-edges (27.9399 keV and 9.6586 keV respectively) were conducted with metal foil references measured in parallel with the sample and standard measurements.

EXAFS data reduction and analysis were conducted with the Demeter suite of x-ray absorption spectroscopy software[29]. Athena was used for background removal, deglitching, and data reduction. Artemis was used to fit the data to determine the amplitude reduction factor (S02), bond length (R), number of nearest neighbors (N), edge energy (E0), and the Debye-Waller factor. The amplitude reduction factor was obtained from fitting known standards at each energy, In foil, Zn foil, InP powder, In2O3 powder, and ZnO powder, where appropriate. This value was then set for the other fits such that the number of nearest neighbors could be a free parameter in the fit.

Computational Methods:

Electronic structure computations using DFT were carried out using the Vienna Ab-initio Simulation Package (VASP)[30-34] following previous works[35-37] on electronic structure of nanocrystals. Calculations were done under the Generalized Gradient Approximation (GGA) using the correlation-exchange functional of Perdew and Wang.[38,39] Both the fluoride surface ligands and internal atoms of QDs were relaxed until forces were less than 0.03 eV/Å. The kinetic energy cutoff was set at 400 eV. For calculations involving defects in the form of surface or substitutional zinc, atoms in the first coordination sphere of the defects were relaxed also. Because we consider these small modelled QDs as isolated particles, the Brillouin zone was sampled only at the gamma point.

3.12. Chapter 3 Bibliography

(1) Kelley, A. M. *ACS Nano* **2011**, *5*, 5254.

(2) Nelson, C. A.; Zhu, X. Y. *Journal of the American Chemical Society* **2012**, *134*, 7592.

(3) Bozyigit, D.; Yazdani, N.; Yarema, M.; Yarema, O.; Lin, W. M. M.; Volk, S.; Vuttivorakulchai, K.; Luisier, M.; Juranyi, F.; Wood, V. *Nature* **2016**, *531*, 618.

(4) Feenstra, R. M.; Hla, S. W.; Springer-Verlag Berlin Heidelberg.

(5) Fritsch, J.; Pavone, P.; Schröder, U. *Physical Review B* **1995**, *52*, 11326.

(6) Rao, C. S. R.; Sundaram, S.; Schmidt, R. L.; Comas, J. *Journal of Applied Physics* **1983**, *54*, 1808.

(7) Bedel, E.; Landa, G.; Carles, R.; Redoules, J. P.; Renucci, J. B. *Journal of Physics C: Solid State Physics* **1986**, *19*, 1471.

(8) Bedel, E.; Landa, G.; Carles, R.; Renucci, J. B.; Roquais, J. M.; Favennec, P. N. *Journal of Applied Physics* **1986**, *60*, 1980.

(9) Peercy, P. S. *Applied Physics Letters* **1971**, *18*, 574.

(10) Alivisatos, A. P.; Harris, T. D.; Carroll, P. J.; Steigerwald, M. L.; Brus, L. E. *The Journal of Chemical Physics* **1989**, *90*, 3463.

(11) Shiang, J. J.; Risbud, S. H.; Alivisatos, A. P. *The Journal of Chemical Physics* **1993**, *98*, 8432.

(12) Seong, M. J.; Mićić, O. I.; Nozik, A. J.; Mascarenhas, A.; Cheong, H. M. *Applied Physics Letters* **2003**, *82*, 185.

(13) Krauss, T. D.; Wise, F. W. *Physical Review B* **1997**, *55*, 9860.

(14) Klein, M. C.; Hache, F.; Ricard, D.; Flytzanis, C. *Physical Review B* **1990**, *42*, 11123.

(15) Kelley, A. M. *The Journal of Physical Chemistry Letters* **2010**, *1*, 1296.

(16) Kelley, A. M. *The Journal of Physical Chemistry A* **2013**, *117*, 6143.

(17) Schmitt-Rink, S.; Miller, D. A. B.; Chemla, D. S. *Physical Review B* **1987**, *35*, 8113.

(18) Mićić, O. I.; Cheong, H. M.; Fu, H.; Zunger, A.; Sprague, J. R.; Mascarenhas, A.; Nozik, A. J. *The Journal of Physical Chemistry B* **1997**, *101*, 4904.

(19) Talapin, D. V.; Gaponik, N.; Borchert, H.; Rogach, A. L.; Haase, M.; Weller, H. *The Journal of Physical Chemistry B* **2002**, *106*, 12659.

(20) Mićić, O. I.; Nozik, A. J.; Lifshitz, E.; Rajh, T.; Poluektov, O. G.; Thurnauer, M. C. *The Journal of Physical Chemistry B* **2002**, *106*, 4390.

(21) Adam, S.; Talapin, D. V.; Borchert, H.; Lobo, A.; McGinley, C.; de Castro, A. R. B.; Haase, M.; Weller, H.; Möller, T. *The Journal of Chemical Physics* **2005**, *123*, 084706.

(22) Dubois, L. H.; Schwartz, G. P. *Physical Review B* **1982**, *26*, 794.

(23) Gallet, D.; Hollinger, G. *Applied Physics Letters* **1993**, *62*, 982.

(24) Kwok, R. W. M.; Jin, G.; So, B. K. L.; Hui, K. C.; Huang, L.; Lau, W. M.; Hsu, C. C.; Landheer, D. *Journal of Vacuum Science & Technology A* **1995**, *13*, 652.

(25) Iyer, R.; Chang, R. R.; Dubey, A.; Lile, D. L. *Journal of Vacuum Science & Technology B* **1988**, *6*, 1174.

(26) Lau, W. M.; Jin, S.; Wu, X. W.; Ingrey, S. *Journal of Vacuum Science & Technology A* **1991**, *9*, 994.

(27) Wang, F.; Yu, H.; Li, J.; Hang, Q.; Zemlyanov, D.; Gibbons, P. C.; Wang; Janes, D. B.; Buhro, W. E. *Journal of the American Chemical Society* **2007**, *129*, 14327.

(28) Sluydts, M.; De Nolf, K.; Van Speybroeck, V.; Cottenier, S.; Hens, Z. *ACS Nano* **2016**, *10*, 1462.

(29) Ravel, B.; Newville, M. *J Synchrotron Radiat* **2005**, *12*, 537.

(30) Kresse, G.; Furthmüller, J. *Physical Review B* **1996**, *54*, 11169.

(31) Kresse, G.; Furthmüller, J. *Computational Materials Science* **1996**, *6*, 15.

(32) Kresse, G.; Hafner, J. *Physical Review B* **1993**, *47*, 558.

(33) Kresse, G.; Hafner, J. *Physical Review B* **1994**, *49*, 14251.

(34) Kresse, G.; Joubert, D. *Physical Review B* **1999**, *59*, 1758.

(35) Zherebetskyy, D.; Scheele, M.; Zhang, Y.; Bronstein, N.; Thompson, C.; Britt, D.; Salmeron, M.; Alivisatos, P.; Wang, L.-W. *Science* **2014**, *344*, 1380.

(36) Zhang, Y.; Zherebetskyy, D.; Bronstein, N. D.; Barja, S.; Lichtenstein, L.; Alivisatos, A. P.; Wang, L.-W.; Salmeron, M. *ACS Nano* **2015**, *9*, 10445.

(37) Zherebetskyy, D.; Zhang, Y.; Salmeron, M.; Wang, L.-W. *The Journal of Physical Chemistry Letters* **2015**, *6*, 4711.

(38) Perdew, J. P.; Chevary, J. A.; Vosko, S. H.; Jackson, K. A.; Pederson, M. R.; Singh, D. J.; Fiolhais, C. *Physical Review B* **1992**, *46*, 6671.

(39) Perdew, J. P.; Wang, Y. *Physical Review B* **1992**, *45*, 13244.

4. Growth and physical properties of electronically coupled supercrystalline solids

4.1. Introduction

Colloidal nanocrystals offer a route toward engineering new classes of materials by acting as discrete units that can be assembled to construct composite solids. The versatility of colloidal synthesis can be exploited to allow for nanoscale building blocks to be made from a wide variety of materials and grown in preselected shapes and sizes. These tailored structural elements can then be assembled into functional materials whose properties are determined by the collective interactions between their constituent parts. Nanocrystal synthesis, and assembly into three dimensional supercrystalline arrays represent the first steps on this path to total bottom-up design of new composite materials. Here, previous efforts have been very successful and are detailed in a large body of work[1,2] identifying conditions for assembly of nanocrystals into ordered arrays including multicomponent binary crystals[3-5] and quasicrystals[6,7]. These works have focused on assembly of nanoparticles that are sterically stabilized by long-chain organic surfactants. Long-chain organic ligands constitute an electrically insulating barrier, typically 1 – 2 nm in thickness, that separates neighboring nanocrystals in the final structure. The resulting supercrystalline composites are strongly insulating overall and material design prospects are constrained by the weak coupling between building blocks.

Simultaneous realization of strong electronic coupling and dense ordered packing of nanocrystal solids has remained elusive. Prior attempts[8,9] have had success with chemically stripping away organic surfactants after supercrystal growth though the resulting volume contraction leads to crack formation and tends to strongly limit the maximum achievable size of ordered domains. An alternative strategy has been to strip away native surfactant ligands to be replaced by shorter[10] or sparser[11] hydrocarbon-based species which provide colloidal stability with lesser steric bulk. In spite of these successes, high performance nanocrystal devices including FETs[12,13], solar cells[14] and LEDs[15] have typically been prepared using electrostatically stabilized nanocrystals cast from polar media without hydrocarbon based stabilizers. This approach yields well passivated surfaces and strong interparticle electronic coupling but produces glassy, disordered nanocrystal solids. For practical device applications, the benefits of hydrocarbon free passivation with compact inorganic ligands have outweighed the costs associated with the disordered morphologies that result. Pushing modular design of materials forward will require a way to preserve the strong coupling and good passivation afforded by the compact inorganic ligand strategy while also attaining high-density ordered packing.

I report here a method for growing highly ordered solids from colloidal metal nanocrystals that are electrostatically stabilized by inorganic chalcogenidometallate (ChM) anions. Slow addition of excess ChM salts to these colloids results in particles coalescing into faceted supercrystals with edge lengths on the order of microns. I first characterize the structure and optoelectronic properties of this material and, second, I examine the nature of the assembly process itself to identify the mechanism of supercrystal growth. The nanocrystals that make up these structures are packed into dense fcc arrays with nearest neighbor surface to surface distances of about 5Å. The interstitial space is filled with a glassy metal chalcogenide matrix which, combined with the short separation between particles, is expected to lead to very strong electronic coupling. This effect is verified by temperature dependent conductivity measurements that show metallic transport across our supercrystals with no evidence of thermally activated hopping processes. The temperature dependent component of resistivity is found to be fully describable by the Bloch-Grüneisen equation[16] within the Boltzmann transport picture for bulk metals.

4.2. Preparation of supercrystals from chalcogenidometallate capped nanocrystals

In a typical example of a supercrystal growth procedure, Au nanoparticles with diameters around 5 nm were synthesized with native 1-dodecanethiol (DDT) ligands providing colloidal stability in non-polar solvents. The Au particles were then re-functionalized by a two-phase ligand exchange process. DDT capped Au particles were dispersed in toluene and phase transferred by stirring into an immiscible hydrazine solution of the salt $(N_2H_5)_4Sn_2S_6$ (Fig 1a). During the phase

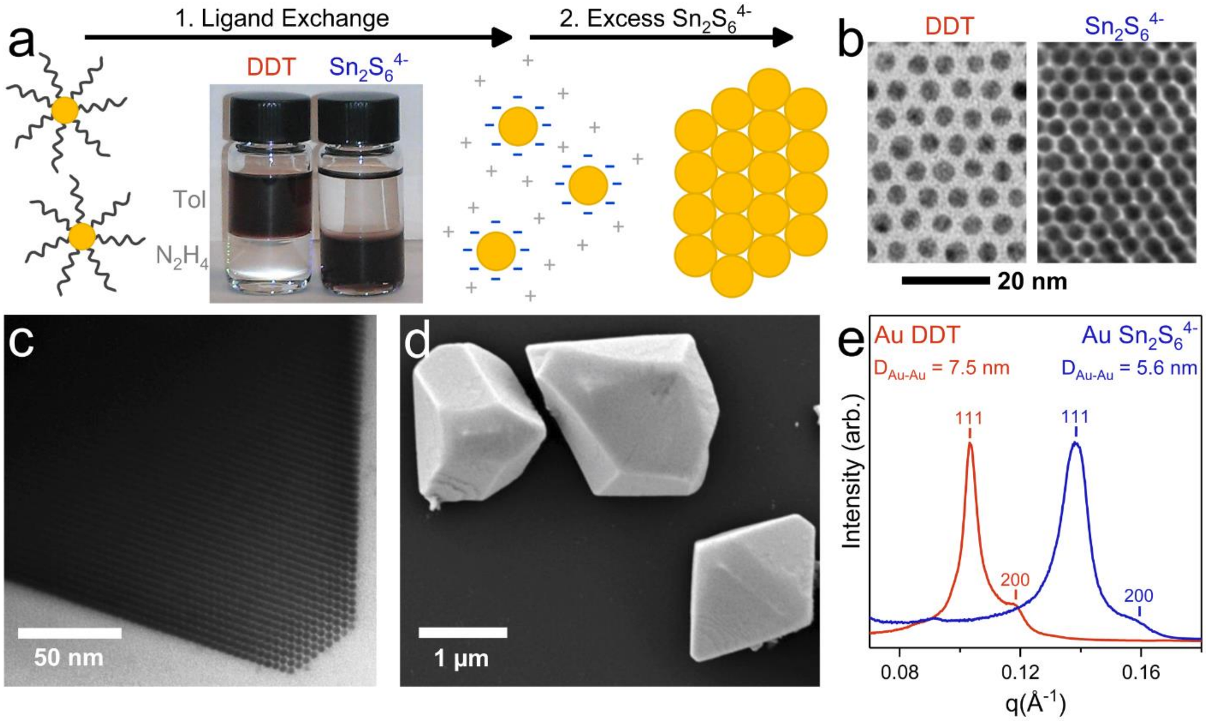

Figure 4-1 Ligand exchange of Au nanocrystals from native organic ligands to compact inorganic anions and subsequent self-assembly. a, A schematic depicting the ligand exchange and self-assembly processes. b, Zoomed in TEM image comparing spacing for self-assembled Au capped with DDT and $Sn_2S_6^{4-}$. c, TEM of an octahedral SC grown from $Sn_2S_6^{4-}$ capped Au. d, SEM image showing three large supercrystals of the same type in (c). e, SAXS data on a linear scale comparing the lattice spacing of assembled Au using long organic ligands and short $Sn_2S_6^{4-}$ ligands.

transfer process, surface bound anionic dodecanethiolate ligands are displaced by thiostannate in the following reaction: $4DDT^{-}_{Au} + (N_2H_5)_4Sn_2S_{6\ solution}$ -> $Sn_2S_6{}^{4-}{}_{Au} + 4(N_2H_5)DDT_{solution}$.

Purification steps were undertaken before and after the phase transfer procedure to remove excess organic residues. In a typical embodiment of the purification procedure, particles were washed by cycles of dispersal in non-polar solvent eg. toluene, and flocculation by non-solvents like acetone, 2-propanol, or ethanol. For air sensitive particles, CdSe, HgTe, Ni, all washing steps were done in a nitrogen glovebox. Au and Pd NCs were initially washed in air, then transferred into a nitrogen glovebox for storage. All subsequent manipulations were done under a nitrogen atmosphere in a glovebox. For metal particles, a pre-exchange thiol treatment was applied. After recovering particles from the synthetic mixture and washing, particles were dispersed in toluene at ~25 mg/mL and an equivalent mass of dodecanethiol was added. After 5 minutes of stirring, particles were flocculated with ethanol and redispersed in hexane or toluene for subsequent two-phase ligand exchange. This process exchanges native ligands for dodecanethiol (DDT) ligands. DDT capped metal particles phase transfer into ChM solutions in hydrazine or NMFA slowly, and are much more resistant to irreversible aggregation during phase transfer compared to NCs capped with the native ligands.

For two-phase ligand exchange into polar solvent, particles in an immiscible non-polar solvent (hexane, toluene) were layered onto a bottom phase consisting of a 25 mM solution of ChM in polar solvent. Note that for exchange into NMFA, hexane must be used as the non-polar phase as toluene is miscible with NMFA. In a typical procedure, 100 mg of DDT capped Au NCs in 12 mL of toluene along with 4 mL of a 25 mM hydrazine solution of $(N_2H_5)_4Sn_2S_6$ were placed in a 20 mL vial with a Teflon coated stirbar. After 12 hours of stirring, phase transfer completed and the clear non-polar top phase was discarded. The colloidal particles in the hydrazine phase were then flocculated by addition of 1.5 mL of acetonitrile, recovered by centrifugation and redispersed in hydrazine. At this stage, the particles were washed by:

1. Adding $(N_2H_5)_4Sn_2S_6$ stock solution to raise the free ChM concentration to 25 mM
2. Flocculating the particles by addition of a minimal amount of acetonitrile. 20% the volume of acetonitrile as compared to hydrazine was sufficient.
3. Collection of the flocculated particles by centrifugation.
4. Redispersal in pure hydrazine.

This washing cycle was repeated three times and the particles were then stored as a 100 mg/mL stock solution in hydrazine. After purification steps to remove organic residues eg. (N_2H_5)DDT, the resulting Au particles are electrostatically stabilized and net negatively charged by their capping layer of $Sn_2S_6^{4-}$ anions. Negative charge at the particle surfaces is balanced by free solvated cations, e.g. protons in the form of $N_2H_5^+$.

Slow addition of excess $(N_2H_5)_4Sn_2S_6$ solution to incrementally increase the concentration of unbound ligand results in flocculation of the colloidal Au. This is expected given that $(N_2H_5)_4Sn_2S_6$ is an electrolyte which dissociates into free ions in polar solvents (Table 4-1) and its addition should destabilize the colloid due to its effect on the ionic strength of the solution. As I show in the following mechanistic study (vide infra), the flocculation behavior is sensitive to the chemical identity of the added electrolyte. When the increased ionic strength is supplied specifically by ChM salts, flocculated particles assemble into ordered supercrystalline arrays (Figure 4-1a). Imaging of the ordered aggregates (Figure 4-1c,d) by TEM and SEM reveals a high degree of internal order with nanocrystal units packed into dense periodic arrays to form supercrystals with micron scale dimensions. Comparison of this material to self-assembled structures grown from DDT capped Au by established methods[5] reveals a marked contraction (Figure 4-1c) in the equilibrium spacing between particles due to the compact size of the $Sn_2S_6^{4-}$ anion relative to DDT. Small-angle x-ray scattering (SAXS) measurements (Figure 4-1e) confirm

10 mM hydrazine solutions	
Solution	Measured Resistance
Hydrazine	67.1 kΩ
KCl	412.1 Ω
NH_4Cl	414.8 Ω
$NaBF_4$	465.3 Ω
K_2S	197.0 Ω
$(N_2H_5)_2S$	470.8 Ω
$(N_2H_5)_4Sn_2S_6$	158.1 Ω
$(N_2H_5)_2In_2Se_4$	349.9 Ω
$(N_2H_5)_3AsS_3$	187.7 Ω

10 mM Aqueous solutions	
Solution	Measured Resistance
D. I. water	568.5 kΩ
KCl	447.6 Ω
NH_4Cl	338.3 Ω
$NaBF_4$	481.1 Ω

Table 4-1: Raw resistances of salt solutions in hydrazine measured at 1 kHz between a pair of platinum electrodes in a parallel plate geometry. Electrolytes were present at 10 mM of the stated formula in all cases. The portion of the table on the right shows data for selected aqueous electrolyte solutions measured by the same setup for comparison. These data show that ChM ligand solutions ionize to a significant degree in hydrazine solvent.

that fcc supercrystals grown from 5 nm Au show a reduction in nearest neighbor center to center distance from 7.5 nm for DDT capped Au down to 5.6 nm for the ligand exchanged Au assembled by flocculation from hydrazine.

4.3. Structural properties of all-inorganic supercrystals

Applying multiple structural characterization techniques, I posit that these composite superstructures consist of crystalline Au NC units embedded in a glassy matrix of amorphous

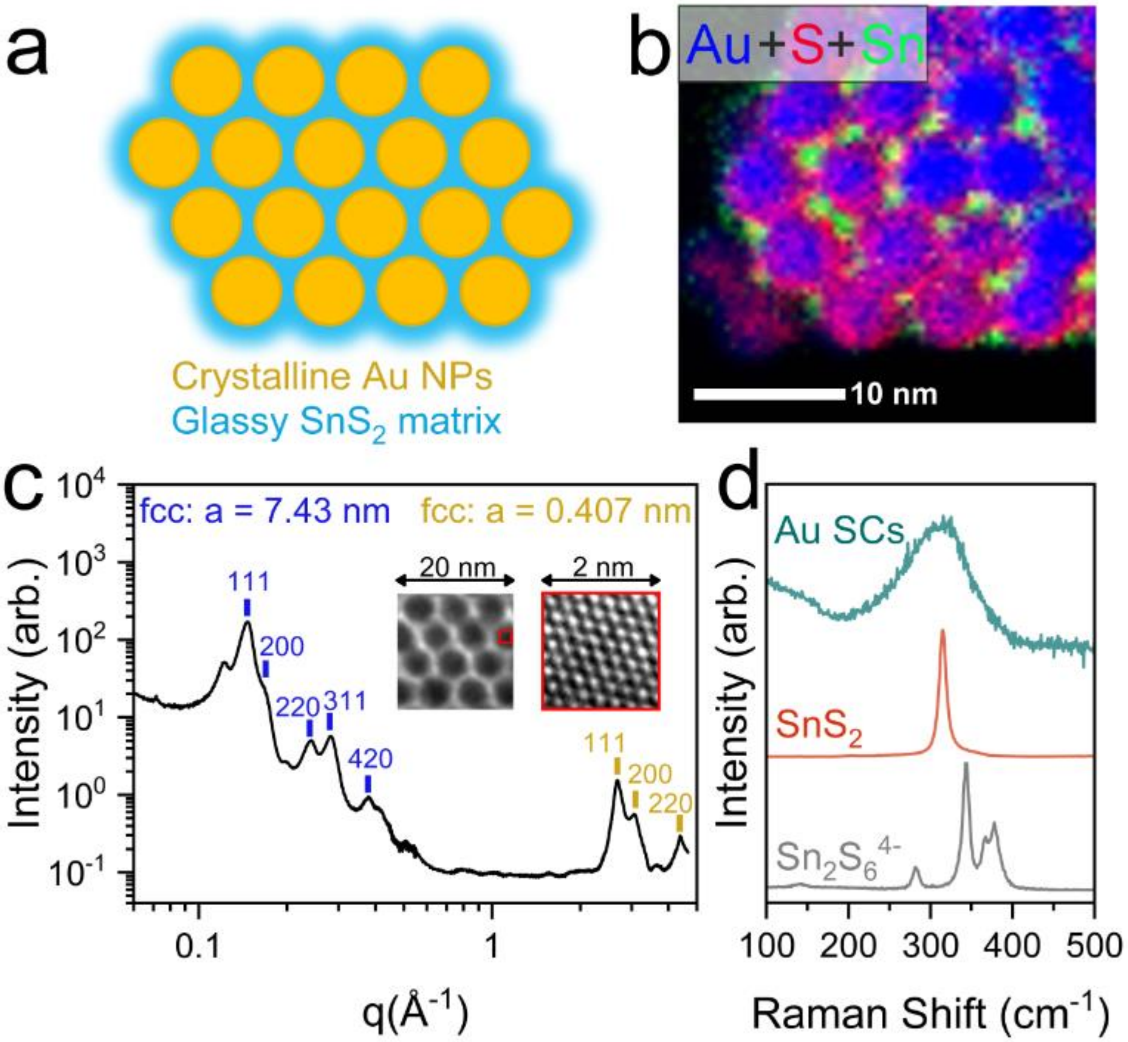

Figure 4-2: Structural characterization of Au supercrystals. a, A drawing depicting the assigned structure of an SC grown from $Sn_2S_6^{4-}$ capped Au. **b,** Elemental map from EELS data showing the concentration of Sn at the interstitial sites of the fcc lattice. **c,** Combined SAXS/WAXS showing the fcc packing of both Au atoms in individual nanocrystals (yellow) and fcc packing of Au nanocrystal units (blue) into supercrystals. Inset TEM images show the same in real space. **d,** Raman scattering data for Au SCs, crystalline SnS_2, and solid $(N_2H_5)_4Sn_2S_6$.

SnS_2 that occupies the void space between nanocrystals. The results are summarized in Figure 4-2.Elemental maps (Figure 4-2b) obtained from electron energy loss spectroscopy (EELS) show that Sn atoms are concentrated at the octahedral and tetrahedral voids in the fcc lattice formed by pure Au nanocrystals. I confirm the crystalline order of both the fcc array of Au nanocrystals and of the atoms in the individual nanocrystal units by a combined SAXS/WAXS measurement (Figure

4-2c) that captures the periodic character of the material at both length scales. The lattice constant of the Au atomic lattice measured here is unchanged from the bulk value, providing good evidence that individual Au nanocrystals are maintained intact during the ligand exchange and assembly process. Notably, diffraction features attributable to the SnS_2 matrix are absent. Weak diffraction from the matrix is consistent with its assignment from Raman spectroscopy as consisting of a tin sulfide glass. The Raman spectrum of Au supercrystals (Figure 4-2d) shows a prominent peak centered at 315 cm^{-1}, the longitudinal optical (LO) phonon frequency of crystalline SnS_2. However, compared to the crystalline material, there is a substantial broadening to a degree that is typically expected for amorphous solids[17]. Further, the rise in scattering intensity at lower shift energies is consistent with a disorder activated scattering from acoustic phonon type modes, also commonly seen in amorphous semiconductors. Taken together, the broadened Raman spectrum and lack of diffraction features point strongly to the matrix material being glassy SnS_2 resulting from partial decomposition of the original hydrazinium thiostannate according to: $(N_2H_5)_4Sn_2S_6$ -> 2 SnS_2 + 2 $(N_2H_5)_2S$. This reaction can be thought of as an analogue of the condensation reactions that are commonly seen in glassy metal-oxide networks in sol-gel processes.

4.4. Optical and electronic properties of all-inorganic supercrystals

Examining the optical and electronic properties of our material, we are able to observe the collective interparticle interactions that are enabled by our inorganic ligands. Figure 4-3 summarizes these results. Compared to assemblies of nanocrystals separated by insulating organic surfactants, the smaller interparticle spacing in our supercrystals and the semiconducting nature of chalcogenide glasses should facilitate much stronger electronic coupling between neighboring nanocrystal units. While optical characteristics of isolated NC units in solution are not strongly dependent on surface termination (Figure 4-4), measurements on the corresponding solids reveal

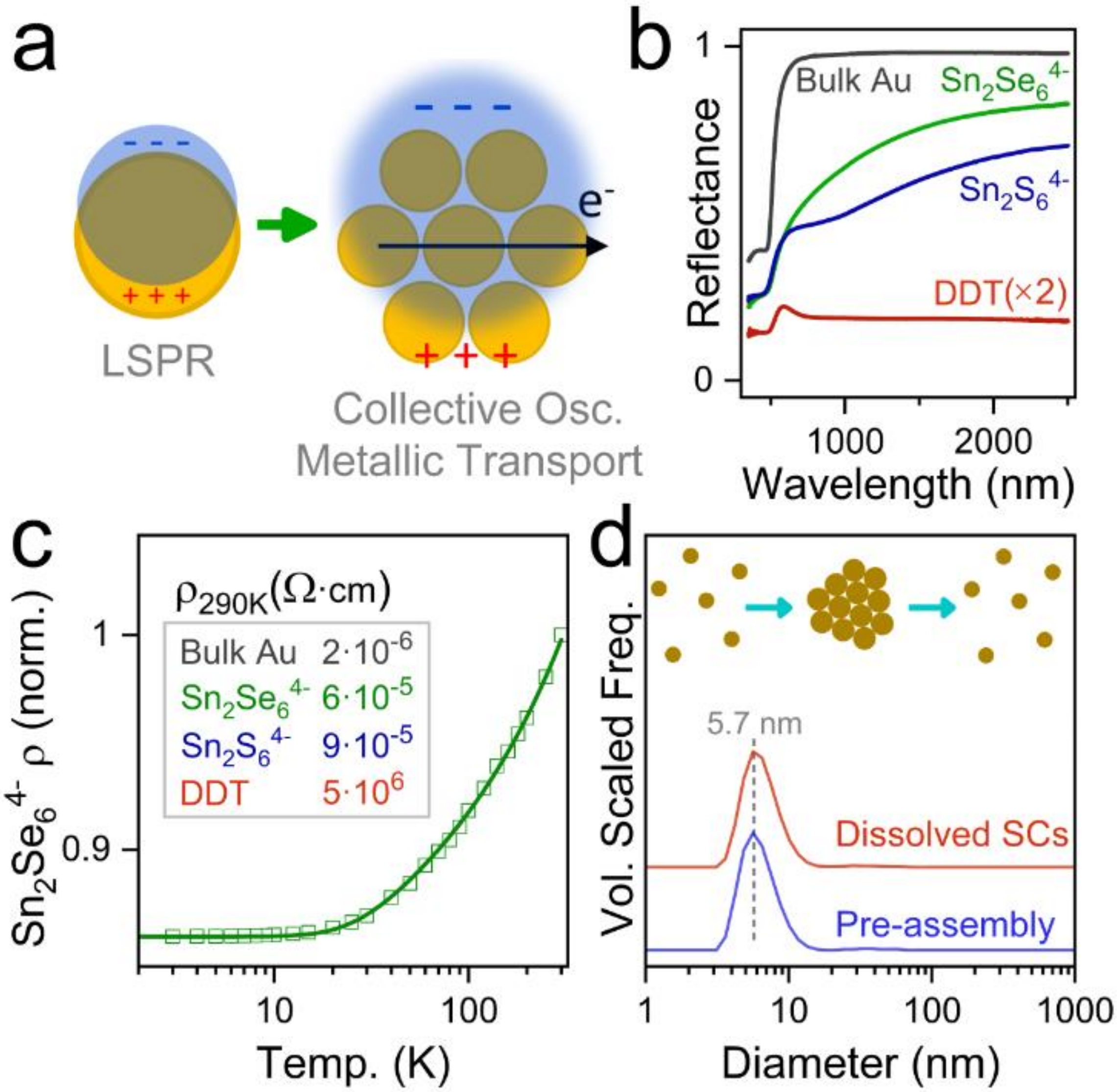

Figure 4-3: Optical and electronic properties of SCs. a, Schematic diagram depicting the transition from free carrier oscillations in a single nanocrystal to oscillations in an electronically coupled array of nanocrystals. **b,** Reflectance of evaporated bulk Au; and Au NCs with DDT, $Sn_2S_6^{4-}$, and $Sn_2Se_6^{4-}$ ligands. **c,** Temperature dependent resistivity data for $Sn_2Se_6^{4-}$ capped Au SCs. Inset gives ρ at 290K for bulk Au and Au NCs with three different ligands. **d,** DLS data showing that colloidal NCs can be assembled into SCs, then re-dissolved to recover the original colloidal state.

the effect of inorganic matrices on promoting strong interparticle coupling. Reflectance measurements (Figure 4-3b) show that the localized surface plasmon resonance (LSPR) of the original isolated Au NC units is strongly affected by assembly into supercrystalline solids.

Supercrystals of DDT capped Au NCs show a reflectance peak centered around the LSPR, broadened and redshifted to 585 nm relative to the 520 nm LSPR position measured in toluene solution. Here the particles are in the weak coupling limit, and the redshift and broadening of the LSPR result from changes in the local dielectric environment and from dipolar coupling between neighboring NC units. The characteristic redshift and broadening of spectral features of Au nanocrystals in close proximity has been studied previously[18,19], notably on films of Au nanocrystals terminated by organic ligands of varying length. The reflectance spectra obtained

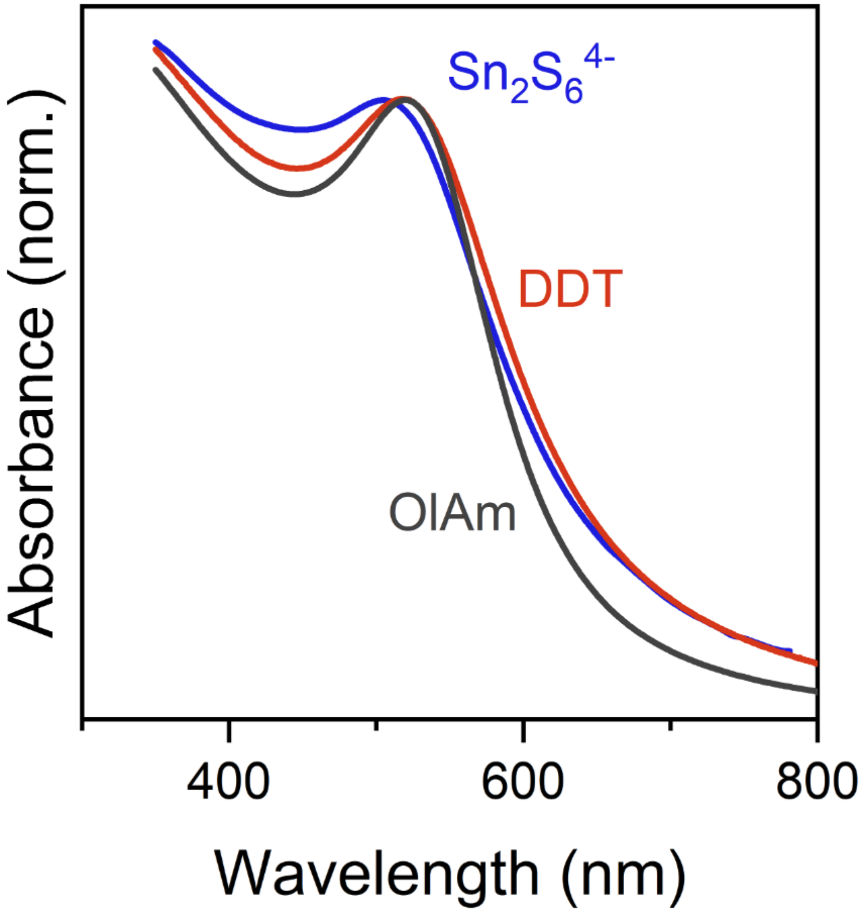

Figure 4-4: Solution phase absorption characteristics vs. capping. Absorbance spectra taken from 5nm diameter Au NCs from the same synthetic batch with native oleylamine ligands (OlAm), post-exchange to dodecanethiol ligands (DDT), and after phase transfer into hydrazine and capping with $(N_2H_5)_4Sn_2S_6$. The localized surface plasmon resonance (LSPR) is evident as an absorbance peak in all three cases.

from inorganic ligand terminated NCs, show the effect of crossing into the strong coupling regime. Comparing the spectra (Figure 4-3b) of DDT capped Au to that of $Sn_2S_6^{4-}$ capped Au SCs, there is a clear transition toward a bulk metallic character. The LSPR broadens to the point of becoming an indistinct shoulder and reflectance rises toward the bulk limit at longer wavelengths. Here, we gain further insight by varying the composition of the inorganic infill. For example, replacing sulfide ions with selenide in the same SC growth scheme yields ordered Au NCs in a glassy $SnSe_2$ matrix. For Au NCs assembled with the selenido species, $Sn_2Se_6^{4-}$ (Figure 4-3b), the transition to

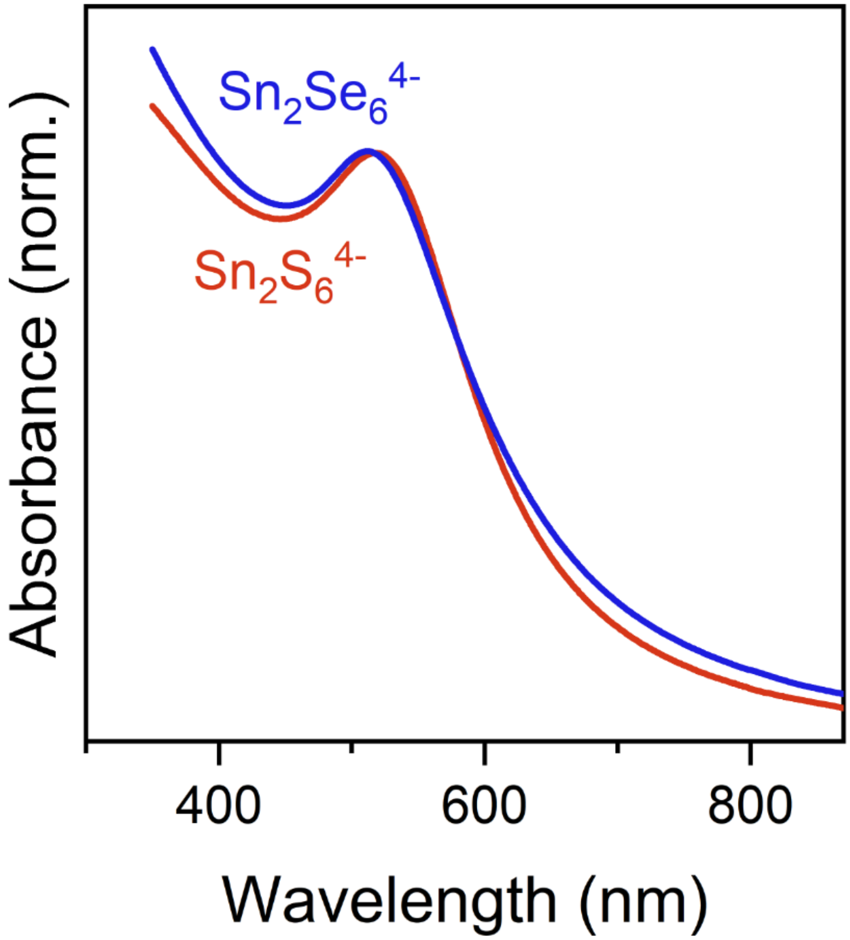

Figure 4-5: Effect of chalcogen on absorption characteristics of chalcogenidometallate capped Au nanocrystals. Absorbance spectra taken from Au NCs phase transferred into hydrazine with two different ChM ligands: $(N_2H_5)_4Sn_2S_6$. and $(N_2H_5)_4Sn_2Se_6$.

a metallic reflectance characteristic is even more complete, with higher reflectance overall and no sign of a residual LSPR related feature. The difference arises from modulation of the strength of interparticle interactions by the chemical nature of the inorganic infill material. The effect is only seen when particles are packed into extended solids; in the colloidal state, Au particles stabilized by surface bound DDT, $Sn_2S_6^{4-}$ or $Sn_2Se_6^{4-}$ all have similar absorption spectra. (Figure 4-5)

Measurements of DC transport (Figure 4-3c) further support assignment of metallic character to Au NC solids linked by ChMs. Resistivity of films composed of powdered of Au supercrystals decreases monotonously from 300K down to 4K. There is no evidence of thermally activated hopping transport which would manifest as increasing resistivity in the low kT limit.

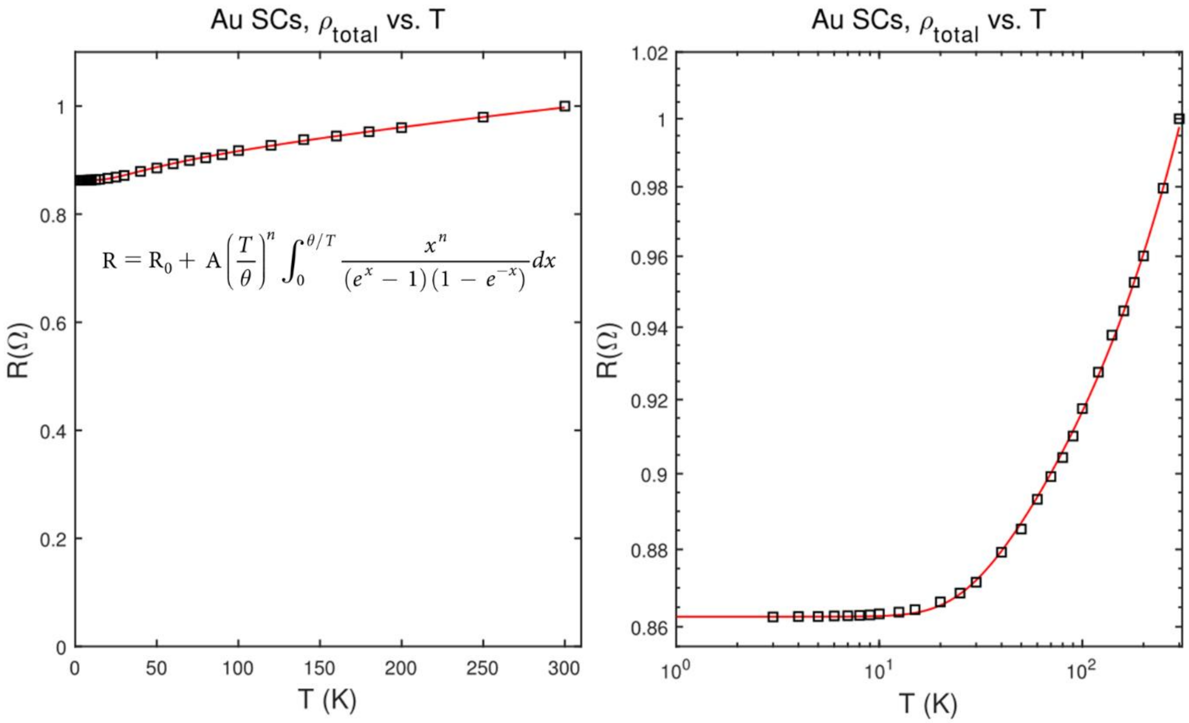

Figure 4-6: Detailed view of the temperature dependent transport data. Data points are plotted as open black squares, linear scale on the left, log–log scale on the right. The solid red line is a Bloch–Grüneisen model fit plotted according to the expression inset in the left panel. The exponential factor is set at n = 4.75 and Debye temperature θ = 135 K. The constants A and R_0 are a normalization factor and an offset for residual resistance respectively.

Instead the temperature dependent resistivity data, plotted as green squares in Figure 4-3c, is well described by Boltzmann transport theory, as for typical metallic solids.

A Bloch–Grüneisen model[16] fit (Figure 4-6) successfully captures the phenomenology of the R vs. T relation and is plotted as a solid line through the discrete data points (Figure 4-3c). Between 300 K and 4 K, the resistivity of the sample drops by a factor of 0.86 yielding a residual resistivity ratio (RRR) $\rho_{300K}/\rho_{4K} = 1.16$, a low value compared to what is observed for pure metal samples[20,21]. Such values of RRR are commonly measured from disordered metallic alloys[22,23] and degenerately doped crystalline semiconductors[24,25]. Room temperature transport in Au–ChM composites is bottlenecked mainly by temperature independent processes eg. surface or impurity scattering with a small, but non–negligible, temperature dependent contribution from phonon scattering. Magnitudes of 290K resistivities (Figure 4-3c, inset) of $Sn_2S_6^{4-}$ and $Sn_2Se_6^{4-}$ capped Au solids with no thermal annealing are within a factor of 50 of evaporated bulk Au films. These values are measured over “poly-supercrystalline” films and contain a resistivity contribution from grain boundary scattering, transport within a given supercrystallite should approach bulk values even more closely. The ChM ligand capped samples in Figure 4-3c both show resistivities that are lower by ~11 orders of magnitude compared to DDT capped Au NCs which are strongly in the insulating regime.

Surface ligand dependent transport in Au NC solids has been a subject of interest in various prior studies which have looked into the transition between insulating and metallic behavior. Measurements of DC conductivity of Au-EDT films have found coefficients of temperature dependence implying nonmetallic[19,26] or metallic[27] transport in different cases. Previously reported measurements[18] made on SCN^- capped Au NC films found clear metallic behavior and DC resistivity on the order of 10^{-5} $\Omega\cdot$cm, in line with our observations on Au ChM solids. However, previously studied conductive solids formed from networks of Au NCs share the common trait that particles are rendered insoluble by the chemical modifications that induce conductivity. Supercrystals grown from ChM capped Au particles dissolve completely into individual nanoparticle units when placed into pure hydrazine. Dynamic light scattering (DLS) measurements (Figure 4-3d) confirm that the colloidal particles that are recovered from re-dissolved supercrystals are indeed individual Au nanocrystals. This observation is significant because it ensures that the metallic transport that we observe does not result from particles necking or partially sintering. Metallic character of the assemblies is observed with no thermal annealing step and with infilling materials (glassy SnS_2 or $SnSe_2$) that do not have conduction bands aligned to the fermi level of Au. Strong electronic coupling between neighboring nanocrystal units in our supercrystals is achieved through a combination of the short interparticle distance, the greater polarizability, and lower tunneling barrier afforded by the inorganic infill compared to that of analogous organic ligands.

4.5. Chapter 4 bibliography

(1) Murray, C. B.; Kagan, C. R.; Bawendi, M. G. *Annual Review of Materials Science* **2000**, *30*, 545.

(2) Boles, M. A.; Engel, M.; Talapin, D. V. *Chemical Reviews* **2016**, *116*, 11220.

(3) Shevchenko, E. V.; Talapin, D. V.; Kotov, N. A.; O'Brien, S.; Murray, C. B. *Nature* **2006**, *439*, 55.

(4) Bodnarchuk, M. I.; Kovalenko, M. V.; Heiss, W.; Talapin, D. V. *Journal of the American Chemical Society* **2010**, *132*, 11967.

(5) Boles, M. A.; Talapin, D. V. *Journal of the American Chemical Society* **2015**, *137*, 4494.

(6) Talapin, D. V.; Shevchenko, E. V.; Bodnarchuk, M. I.; Ye, X.; Chen, J.; Murray, C. B. *Nature* **2009**, *461*, 964.

(7) Ye, X.; Chen, J.; Eric Irrgang, M.; Engel, M.; Dong, A.; Glotzer, Sharon C.; Murray, C. B. *Nature Materials* **2016**, *16*, 214.

(8) Dong, A.; Jiao, Y.; Milliron, D. J. *ACS Nano* **2013**, *7*, 10978.

(9) Baumgardner, W. J.; Whitham, K.; Hanrath, T. *Nano Letters* **2013**, *13*, 3225.

(10) Sayevich, V.; Guhrenz, C.; Dzhagan, V. M.; Sin, M.; Werheid, M.; Cai, B.; Borchardt, L.; Widmer, J.; Zahn, D. R. T.; Brunner, E.; Lesnyak, V.; Gaponik, N.; Eychmüller, A. *ACS Nano* **2017**, *11*, 1559.

(11) Bodnarchuk, M. I.; Yakunin, S.; Piveteau, L.; Kovalenko, M. V. *Nature Communications* **2015**, *6*, 10142.

(12) Jang, J.; Liu, W.; Son, J. S.; Talapin, D. V. *Nano Letters* **2014**, *14*, 653.

(13) Choi, J.-H.; Fafarman, A. T.; Oh, S. J.; Ko, D.-K.; Kim, D. K.; Diroll, B. T.; Muramoto, S.; Gillen, J. G.; Murray, C. B.; Kagan, C. R. *Nano Letters* **2012**, *12*, 2631.

(14) Liu, M.; Voznyy, O.; Sabatini, R.; García de Arquer, F. P.; Munir, R.; Balawi, Ahmed H.; Lan, X.; Fan, F.; Walters, G.; Kirmani, Ahmad R.; Hoogland, S.; Laquai, F.; Amassian, A.; Sargent, Edward H. *Nature Materials* **2016**, *16*, 258.

(15) Li, X.; Zhao, Y.-B.; Fan, F.; Levina, L.; Liu, M.; Quintero-Bermudez, R.; Gong, X.; Quan, L. N.; Fan, J.; Yang, Z.; Hoogland, S.; Voznyy, O.; Lu, Z.-H.; Sargent, E. H. *Nature Photonics* **2018**, *12*, 159.

(16) Chelikowsky, J. R.; Louie, S. G. *Quantum Theory of Real Materials*; Springer US, 1996.

(17) Brodsky, M. H. In *Light Scattering in Solids*; Cardona, M., Ed.; Springer Berlin Heidelberg: Berlin, Heidelberg, 1975, p 205.

(18) Fafarman, A. T.; Hong, S.-H.; Caglayan, H.; Ye, X.; Diroll, B. T.; Paik, T.; Engheta, N.; Murray, C. B.; Kagan, C. R. *Nano Letters* **2013**, *13*, 350.

(19) Fishelson, N.; Shkrob, I.; Lev, O.; Gun, J.; Modestov, A. D. *Langmuir* **2001**, *17*, 403.

(20) Hall, L. A.; Germann, F. E. E. *Survey of electrical resistivity measurements on 8 additional pure metals in the temperature range 0 to 273 K*; U.S. National Bureau of Standards; for sale by the Supt. of Docs., U.S. Govt. Print. Off., Washington, 1970.

(21) Lide, D. R. *CRC Handbook of Chemistry and Physics: A Ready-reference Book of Chemical and Physical Data*; CRC-Press, 1995.

(22) Clark, A. F.; Childs, G. E.; Wallace, G. H. *Cryogenics* **1970**, *10*, 295.

(23) Bardeen, J. *Journal of Applied Physics* **1940**, *11*, 88.

(24) Yamanouchi, C.; Mizuguchi, K.; Sasaki, W. *Journal of the Physical Society of Japan* **1967**, *22*, 859.

(25) Ahn, B. D.; Oh, S. H.; Kim, H. J.; Jung, M. H.; Ko, Y. G. *Applied Physics Letters* **2007**, *91*, 252109.

(26) Müller, K. H.; Herrmann, J.; Raguse, B.; Baxter, G.; Reda, T. *Physical Review B* **2002**, *66*, 075417.

(27) Zabet-Khosousi, A.; Trudeau, P.-E.; Suganuma, Y.; Dhirani, A.-A.; Statt, B. *Physical Review Letters* **2006**, *96*, 156403.

5. Assembly mechanism of electrostatically stabilized colloids

5.1. Introduction

With structural, optical, and electronic properties of the all-inorganic supercrystalline solids addressed, I sought to delve into the process by which they form. Combining experiment and simulation, I investigated the mechanism of the assembly process and found that formation of ordered structures depends on polarization effects. My endeavor built upon previous mechanistic studies of nanoparticle self assembly[1] making use of x-ray scattering techniques that have previously been employed[2-5] to track assembly of organic surfactant stabilized colloidal nanoparticles. The result was that ordering in the present electrostatically stabilized system was found to take place through a non-classical[6] mechanism involving a disordered but dense precursor phase. Such crystal growth schemes[7] that occur via multiple steps and take particles through one or more “pre-nucleation cluster” stages are well studied, especially in biological systems[8]. For assembly of colloidal nanocrystals, assembly via post-agglomeration ordering represents a new phenomenon and is possible as a direct result of interactions between the core material of the particles and their polar electrolyte environment.

When immersed in a solution of strongly binding multivalent ChM anions, metallic particles polarize forming image charges which allow for accumulation of a dense cloud of bulky anions to form around them. The interplay between charge asymmetry of an electrolyte, dielectric contrast between particle and solvent medium, and ion distribution around a charged nanoparticle has been previously predicted[9]. Self-assembly aided by forces related to accumulated ion layers represents a manifestation of this effect. Dense anion layers make ordering and super-crystallization possible by providing a strong short-range repulsive force between particles and preventing jamming into kinetically trapped, low density aggregates. Further, this assembly process is general across types of metal nanoparticle, polar solvent, particle size, and type of ChM salt. This degree of versatility opens up a wide parameter space for exploring different combinations of particle and matrix materials. More broadly, an understanding of the assembly of metal nanoparticles capped with inorganic ligands can point to future steps toward generalizing the process further and represents an important step toward bottom up design of functional nanocrystal composites.

5.2. Onset of ordering:

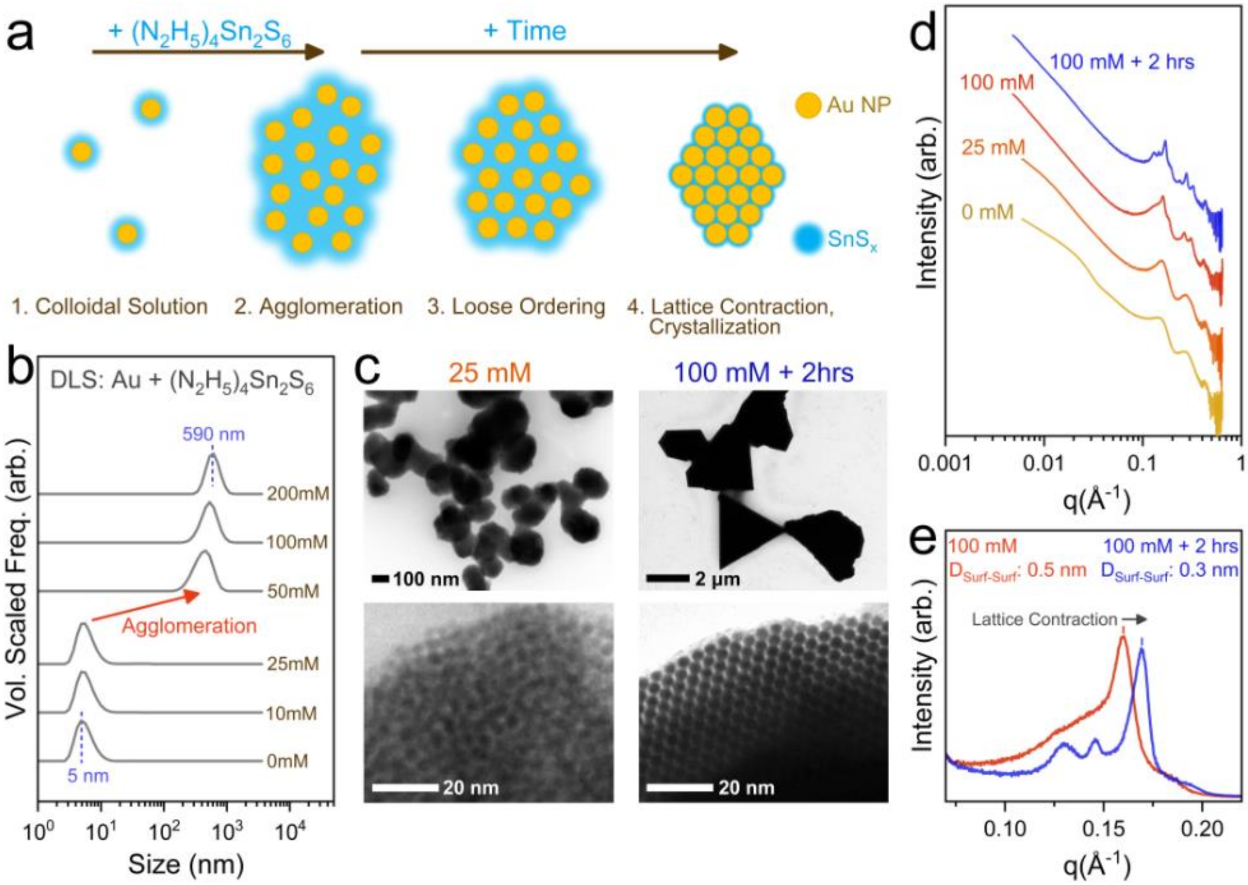

Figure 5-1: Mechanism of assembly of $Sn_2S_6^{4-}$ capped Au nanoparticles. a, Schematic diagram depicting the assembly process. **b,** DLS data showing the transition from the colloidal to agglomerated state that occurs at 25 mM < [$Sn_2S_6^{4-}$] < 50 mM. **c,** TEM images showing the material recovered from drying Au colloids with [$Sn_2S_6^{4-}$] = 25 mM and [$Sn_2S_6^{4-}$] = 100 mM. **d,** SAXS data on a log-log scale showing the progression of structuring with increase of [$Sn_2S_6^{4-}$]. **e,** Linear scale SAXS plot emphasizing the lattice contraction and ordering that occurs after the initial loose agglomeration.

Au colloids flocculated by the specific method of adding excess hydrazinium chalcogenidometallate ligands retain strongly repulsive interparticle forces at short range. With particles prevented from jamming, these loose agglomerations are able to find a global energetic minimum by ordering and densifying into supercrystals. The schematic in Figure 5-1a summarizes the proposed stages of the super-crystallization process. Addition of $(N_2H_5)_4Sn_2S_6$ ligand solution induces free colloidal particles to agglomerate. Over the timescale of hours, these suspended agglomerations first order loosely, then densify into the final supercrystalline structure as slow decomposition of the bound ligands leaves behind amorphous SnS_2 glass in the interstices.

To justify the proposed assembly mechanism, I apply a combination of techniques to monitor the changes that occur as free colloidal particles are assembled. First, in-situ dynamic light scattering (DLS) data (Figure 5-1b) shows that agglomeration occurs at a critical threshold as the concentration of excess ligand is increased. As the excess ligand concentration is incremented from 25 mM to 50 mM, the hydrodynamic radii of the species in solution increase from 5 nm free particles to ~0.5 µm agglomerations. A clear difference between these states can also be seen in real space imaging ex-situ by TEM. Dropcasting Au colloids with excess ligand levels of 25 mM or below onto TEM grids and imaging reveals glassy agglomerations 100 – 300 nm in diameter (Figure 5-1c). Particles are seen to pack relatively densely but randomly. This glassy internal structure is the result of fast drying such that the originally colloidal particles are not afforded sufficient time to reach an ordered state. What is seen in TEM imaging studies represents a frozen precursor to the supercrystals that form when a colloid is flocculated with excess $(N_2H_5)_4Sn_2S_6$ and let stand. TEM images (Figure 5-1c) obtained from a sample Au colloid flocculated in 100 mM thiostannate solution and aged for 2 hours reveal faceted supercrystals with 1 – 5 µm edge lengths. Images taken at higher zoom clearly show the internal lattice symmetry of these large structures.

Structural changes that occur during the assembly process can be monitored by a SAXS experiment that gives information about the onset of ordering. A series of assembly experiments were set up such that four identical starting colloids of Au in N_2H_4 in four separate vials each had the concentration of $(N_2H_5)_4Sn_2S_6$ incrementally increased taking the samples through four stages: **1.** 0 mM, **2.** 25 mM, **3.** 100 mM, and **4.** 100 mM + 2 hours wait time. In the course of this procedure, the assembly process was arrested by addition of MeCN to precipitate the colloid at the end of a different stage for each of the four samples. At the end of stage 4, all samples were collected and deposited on polyimide film for SAXS measurements (Figure 5-1d). The yellow and green traces show results for the two samples where MeCN was added at stage 1, and 2 respectively. These samples were still colloidal at the time of MeCN precipitation as the $(N_2H_5)_4Sn_2S_6$ concentration was below 50 mM. The result in both cases was formation of amorphously packed aggregates. These first two traces serve as a control experiment to verify that precipitation by a small amount of acetonitrile immobilizes the particles and prevents further reorganization. If particles could rearrange, the subsequent increase of the $(N_2H_5)_4Sn_2S_6$ concentration to 100 mM would result in supercrystals forming from these amorphous aggregates. In contrast, the samples precipitated after stage 3 and stage 4, shown in red and blue in Figure 5-1d, do show formation of ordered phases. For these samples, agglomeration occurs due to the 100 mM $(N_2H_5)_4Sn_2S_6$ concentration and the colloids are already destabilized by the time MeCN is added at the end of stages 3 and 4. The effective difference between these two samples is in the length of the wait time between raising the $(N_2H_5)_4Sn_2S_6$ concentration to 100 mM and the addition of MeCN to freeze the particles in place. Both samples show evidence of translational lattice symmetry by the SAXS measurements in Figure 5-1d, with sharper and more defined peaks indicating a higher degree of order in the sample precipitated after waiting 2 hours. A more surprising and counterintuitive difference between the internal structure of these two samples is highlighted in Figure 5-1e. During the 2 hour wait time, the agglomerated structures induced by $(N_2H_5)_4Sn_2S_6$ addition not only rearrange to a higher degree of order, they contract. The fcc lattice constant shrinks such that the calculated surface to surface distance between neighboring particles in the lattice decreases from 0.5 nm to 0.3 nm. Apparently, supercrystals form by particles first loosely ordering at a larger spacing followed by a contraction and densification that produces the final faceted energy minimized structures.

This strange observation motivates questioning why the loose assemblies contract at this final stage. What slow process results in the change in interparticle potentials that allows the final densification? The likely answer lies in the slow ligand decomposition process: $(N_2H_5)_4Sn_2S_6$ -> 2 SnS_2 + 2 $(N_2H_5)_2S$ as discussed regarding results presented in Figure 4-2d. The conversion of the original bulky anions to glassy SnS_2 eliminates sulfide ions from the tin-sulfur framework. Free S^{2-} ions are then able to diffuse out of the supercrystal in the form of $(N_2H_5)_2S$ with protonated solvent balancing charge. In addition to explaining the Raman results of Figure 4-2d and lattice contraction emphasized in Figure 5-1e, there is another initially counterintuitive observation that clarified by this hypothesis: The final contracted lattice constant of an Au supercrystal is quite insensitive to the size of the cation counterpart to the $Sn_2S_6^{4-}$ ion.

5.3. Flocculation of electrostatically stabilized colloids by electrolyte addition: effect of cation dimensions

I carried out an experiment in which the size of the charge balancing cations of the thiostannate anion was varied and resulting lattice parameters of the supercrystals grown with these salts was monitored by SAXS. In one set of experiments, the solvated proton cations, $N_2H_5^+$, were replaced by K^+. In another, amines were added to convert the $N_2H_5^+$ cation into the corresponding alkylammonium cation.

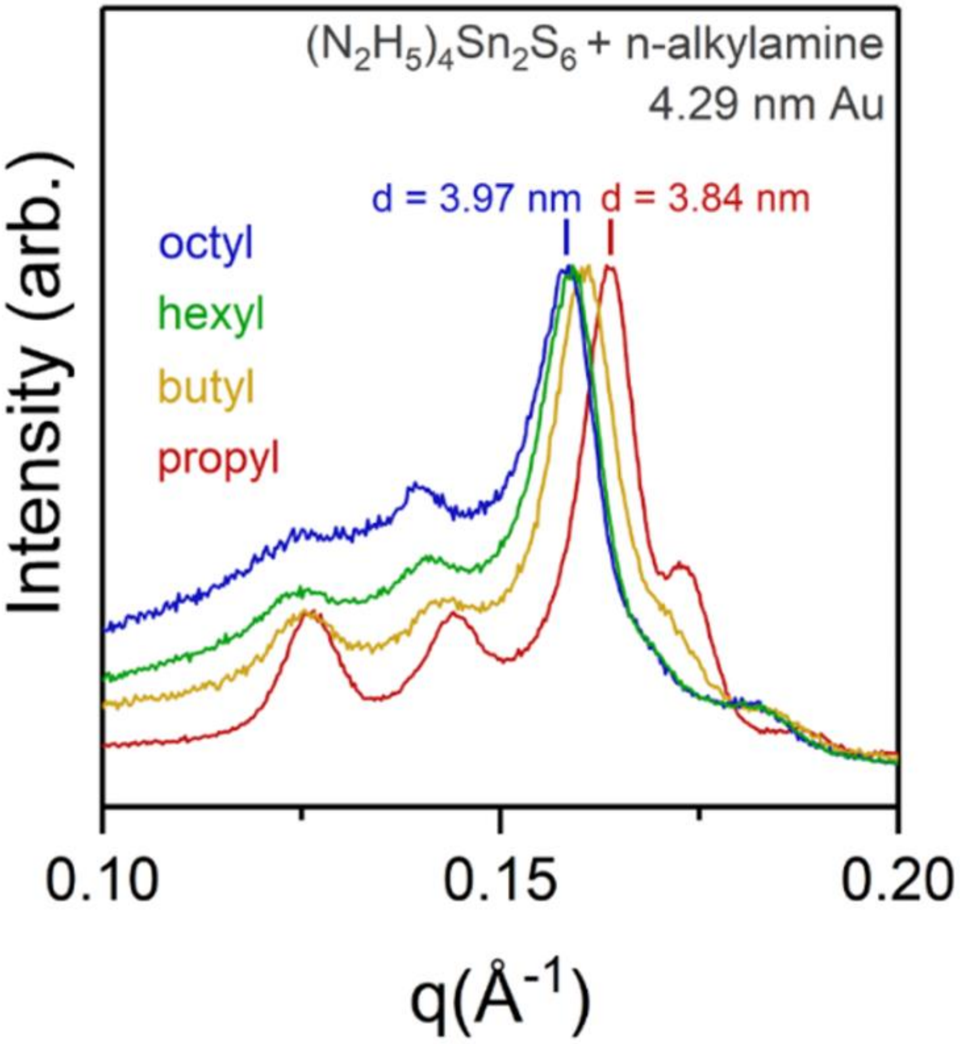

Figure 5-2: Normalized SAXS data taken from assemblies of $(N_2H_5)_4Sn_2S_6$ capped Au NCs flocculated by addition of co-solutions of $(N_2H_5)_4Sn_2S_6$ n-alkylamines.

All amines used in this experiment were soluble in hydrazine at the necessary 1 M concentration and reacted with hydrazinium cations to form n-alkylammonium thiostannates. Assembly by flocculation with these species resulted in superstructures with lattice constants that increased

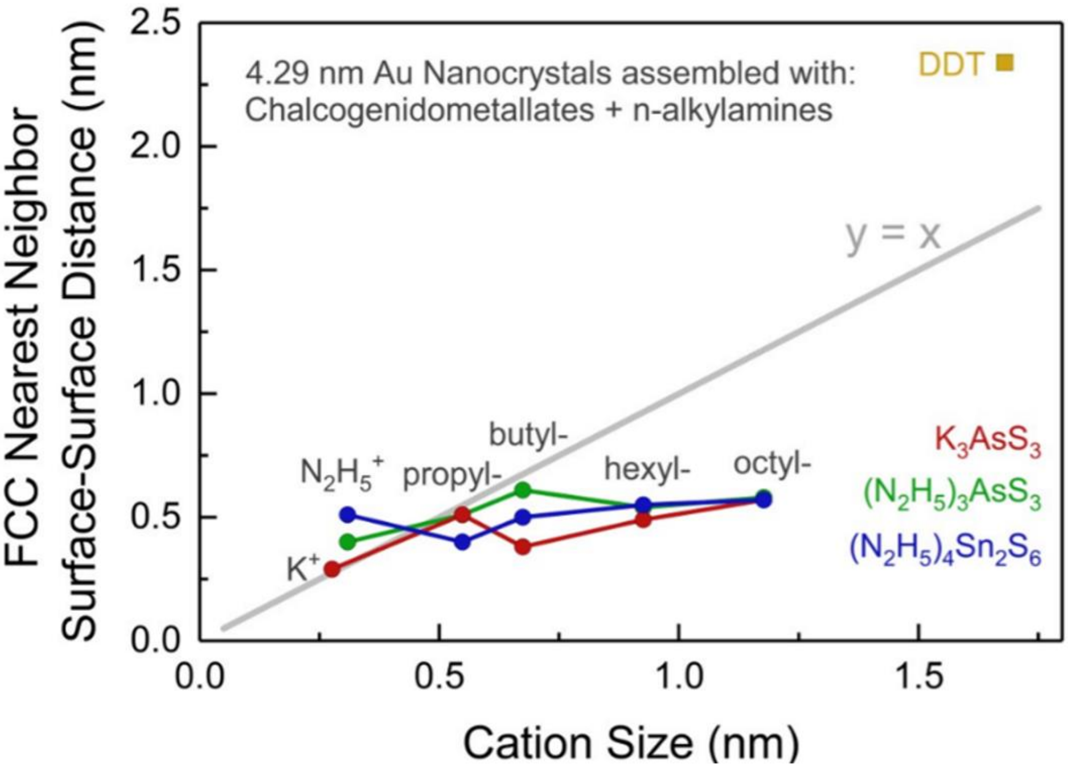

Figure 5-3: Supercrystal nearest neighbor surface to surface spacing related to cation dimensions

with increasing alkyl chain length. The increase in nearest neighbor surface to surface spacing is less than would be expected if cations were significantly intercalated into the final structures. This point is made in Figure 5-3 which plots nearest neighbor spacings for SCs grown by addition of 15 different ChM ligand solutions against the size of the cationic species. As cation size is increased, spacings increase less steeply than the y = x line which denotes the nearest neighbor distance that would be expected if the particles were spaced out by one monolayer of cations. In fact, the data do not support a strong trend of larger supercrystalline lattice constants with larger cation sizes. This provides strong evidence of a significant role of ChM decomposition and rearrangement as posited in the main text. The rearrangement pathway: $(\text{cation})_4Sn_2S_6 \rightarrow 2\ SnS_2 + 2\ (\text{cation})_2S$ to form glassy SnS_2 in the superlattice interstices results in expulsion of $(\text{cation})_2S$ from the growing lattice and a weak dependence of lattice dimensions on cation size. As a comparison, the relevant lattice parameter of DDT capped Au superlattices is also included and is plotted against the length of a dodecanethiol molecule as an effective "cation size". In DDT capped Au superlattices, the DDT ligands are present in significant amounts between neighboring particles and the result is a surface to surface distance that is, as expected, larger than the size of a dodecanthiol molecule.

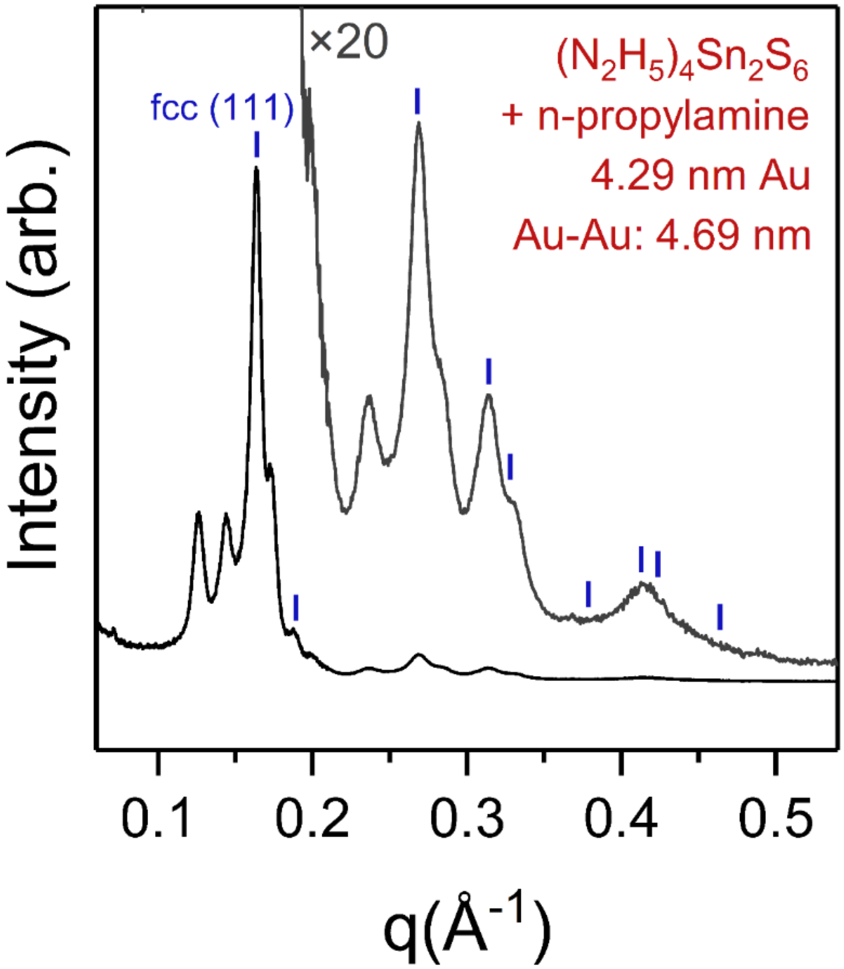

Figure 5-4: Linear scale SAXS data taken from powdered supercrystals assembled by addition of propylammonium thiostannate. The upper trace plots the same data as the lower trace but multiplied by a factor of 20 for clearer viewing of the higher index features. The blue marks denote peaks that are expected for an fcc supercrystal. This sample shows a uniquely pronounced incidence of non-fcc minority phases.

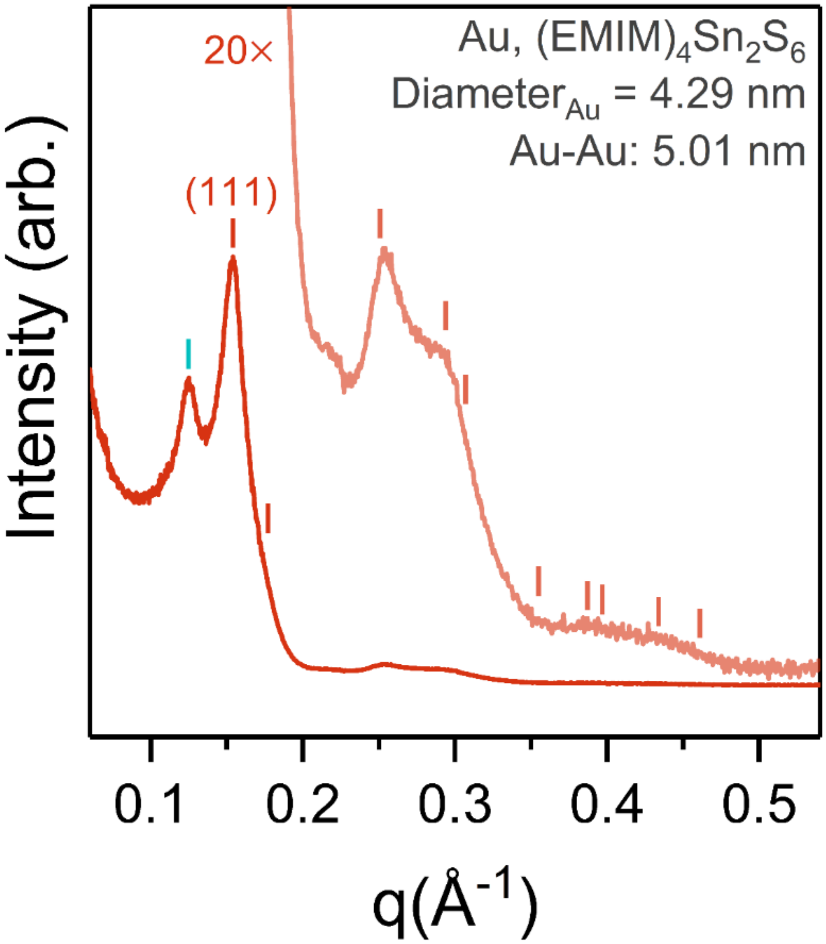

Figure 5-5: SAXS pattern of 4.29 nm diameter Au NCs assembled using a thiostannate solution where the monovalent cation is the aprotic 1-ethyl-3-methylimidazolium (EMIM). The marks indicate locations of fcc reflections calculated based on the indicated (111) reflection. The green mark denotes a peak from a non-fcc minority phase.

An additional experiment, Figure 5-5, examined the effect of using the (EMIM) cation as a counterion to thiostannate. This experiment represents a case where Au particles are assembled using thiostannate anions balanced by a bulky aprotic cation. In contrast to the experiments where n-alkyl ammonium cations were used, there is no proton equilibrium between bulky cations, solvent, and NC surfaces. Instead, the species carrying the positive charge is forced to remain bulky. This stands as a control experiment to be considered in tandem with the alkylammonium experiments. With protic bulky cations, it could be the case that electrostatic forces affect the proton equilibrium of cations surrounding a growing supercrystal such that protons are pulled onto smaller hydrazinium cations or even onto dangling sulfido moieties on the nanocrystal surfaces. Assembly using $(EMIM)_4Sn_2S_6$ resulted in a slightly expanded lattice dimension, but by less than expected if the EMIM cations are to remain entirely within the interstices of resulting structures.

Supercrystals grown using the same process but substituting the $N_2H_5^+$ cations for K^+, $EMIM^+$, or various n-alkylammonium cations all result in final contracted lattices with similar dimensions as measured by SAXS (Figure 5-2,Figure 5-3). This points to a solution phase ion equilibration process that allows excess anions to be solvated and diffuse out of growing superlattices to avoid building up a space charge. With all experimental data accounted for by a hypothesis that depends upon the specific decomposition chemistry of the $Sn_2S_6^{4-}$ anionic ligand, I now consider the chemical generality of the supercrystal assembly process as it relates to the anionic chalcogenidometallate species.

5.4. Flocculation of electrostatically stabilized colloids by electrolyte addition: effect of anion valency

Exploring the effects of different anion chemistries, I find that the flocculation and assembly of colloidal Au by addition of the $Sn_2S_6^{4-}$ ion is part of a general phenomenon that spans a broad range of chalcogenidometallate (ChM) ions. Further, the result of adding ChM to Au colloids cannot be simply explained by ionic strength effects. If salts of NO_3^-, Cl^-, or BF_4^- are added to a hydrazine solution of $Sn_2S_6^{4-}$ stabilized Au particles, a very different type of flocculation behavior results. Salts such as $NaNO_3$ dissociate as simple 1:1 electrolytes in hydrazine, are chemically inert and non-nucleophilic, and will not coordinate to Au surfaces or

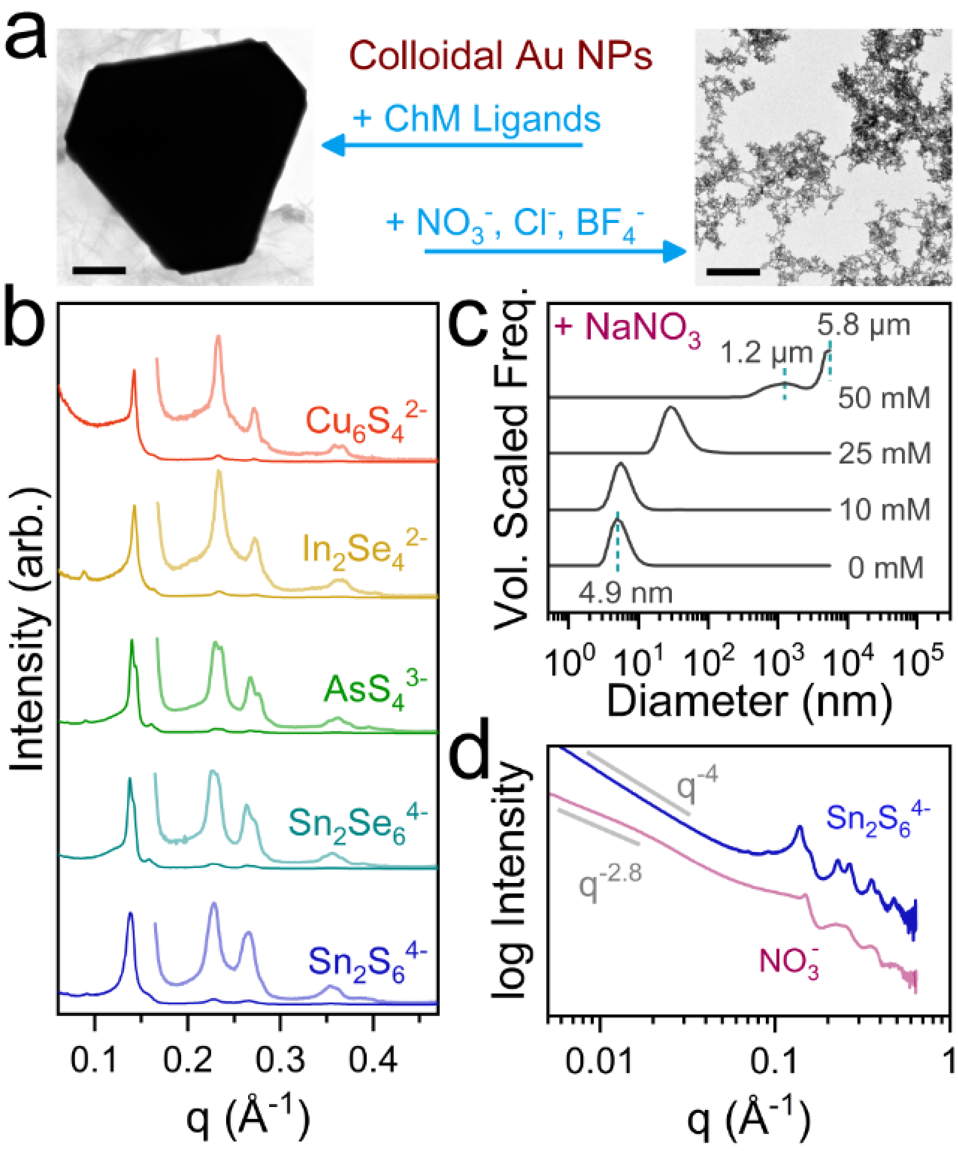

Figure 5-6: Generality of chalcogenidometallate based assembly of Au. **a,** TEM images summarizing the result of aggregating colloidal Au with ChM ligands (left) and non-binding 1:1 electrolytes (right). Scale bars are 500 nm. **b,** Linear scale SAXS data showing the result of assembling colloidal Au by adding different hydrazinium ChM salts. Light traces correspond to dark traces x20 for visibility. **c,** DLS data showing the uncontrolled fractal aggregation that results from addition of $NaNO_3$ to colloidal Au in N_2H_4. **d,** Log-log scale SAXS comparing the Porod's Law scaling at low q for Au aggregated with $NaNO_3$ and with $(N_2H_5)_4Sn_2S_6$.

displace bound ligands. These salts provide a way to vary ionic strength while leaving the concentration of binding species in solution unchanged. Figure 5-6a summarizes the contrasting results of flocculation by ChM ligands and non-binding electrolytes. While ChM ligands produce the familiar large faceted supercrystals, flocculation by $NaNO_3$, NaCl, NH_4Cl, $NaBF_4$, etc. result in porous, branching, low-density aggregates.

I confirm the crystalline order of supercrystals grown from multiple chemically distinct ChM ligands using SAXS (Figure 5-6b). These four types of supercrystals all adopt an fcc or fcc-approximate lattice all with similar lattice constants. This result speaks strongly to the generality of the supercrystal growth process and its insensitivity to the specific structure or chemical nature of a given ChM ligand. Crystallization is observed whether the ChM binds through S or Se donors, and for ChM species that are tetrahedral[10] (AsS_4^{3-}) edge-sharing tetrahedral dimers[11] ($Sn_2S_6^{4-}$) polymeric[12] ($In_2Se_4^{2-}$) or a range of compact cluster species[13] ($Cu_6S_4^{2-}$). This provides strong evidence that specific ligand-Au binding geometries or surface constructions are not a necessary condition for supercrystal formation. All of these ChM species have in common that they are symmetric electrolytes with monovalent cations and multivalent anions, all bind strongly to Au, and all are able to undergo decomposition reactions that eliminate anions to produce the corresponding neutral metal chalcogenide.

Flocculation of Au colloids by non-binding electrolytes that do not possess these properties results in formation of low-density branching aggregates. This is seen experimentally by addition of simple 1:1 salts such as $NaNO_3$ which destabilize Au colloids at concentrations of 25 mM or above. Tracking this process by DLS (Figure 5-6c), we see that flocculation of colloidal Au by $NaNO_3$ occurs by uncontrolled growth of multi-micron scale structures. This is in contrast to what occurs during flocculation by ChM species where growth has a self-limiting character (Figure 5-6b) and aggregates quickly attain sizes of ~0.5 µm that increase very slowly thereafter. I then inferred the presence of repulsive short-range interactions that prevent jamming and allow assembly and energy minimization of ChM aggregated particles. In contrast, DLS and TEM data imply that simply increasing ionic strength without adding ChM salts causes net-attractive interparticle potentials and rapid aggregation. A comparison of SAXS (Figure 5-6d) of Au colloids aggregated by $(N_2H_5)_4Sn_2S_6$ and by $NaNO_3$ supports this conclusion. The loose branching aggregates as seen in TEM for the NO_3^- flocculated material show a power law scaling of $q^{-2.8}$ in the SAXS region around q = 0.01. This indicates that the aggregates grow as mass fractals and are the result of particles that are kinetically trapped in low density structures due to sticky interactions at short-range. This mode of aggregation is well precedented[14] and formation of branched aggregates is the behavior that is expected upon destabilization of charged colloids in polar media. The question is then why flocculation of Au NPs using ChM salts represents such a general and unprecedented path to assembly.

5.5. Effect of nanocrystal material on aggregation behavior: Impact of polarization and image charges

Considering flocculation of nanocrystal materials other than Au gives additional insight into what conditions are necessary in order to observe supercrystal formation. I find that the interaction between Au and ChM salts is not unique. Rather, it represents an archetype of a more general interaction between metallic NPs and ChM ligands. Compared to colloidal nanoparticles of dielectric materials, metallic particles are able to stabilize a far denser layer ChM^- anions near their surfaces due to formation of attractive image charges at their surfaces. I observe this effect experimentally by elemental analysis results from ICP-OES and from x-ray fluorescence (XRF) (Table 5-1). Our measurements of capping density of ChM ligands on dielectric NCs agree previous literature[10,15] and find 1 – 2 ChM ligands/nm^2. In stark contrast, metallic NPs have apparent capping densities that are higher by between a factor of 4 and 10. Indeed, we often

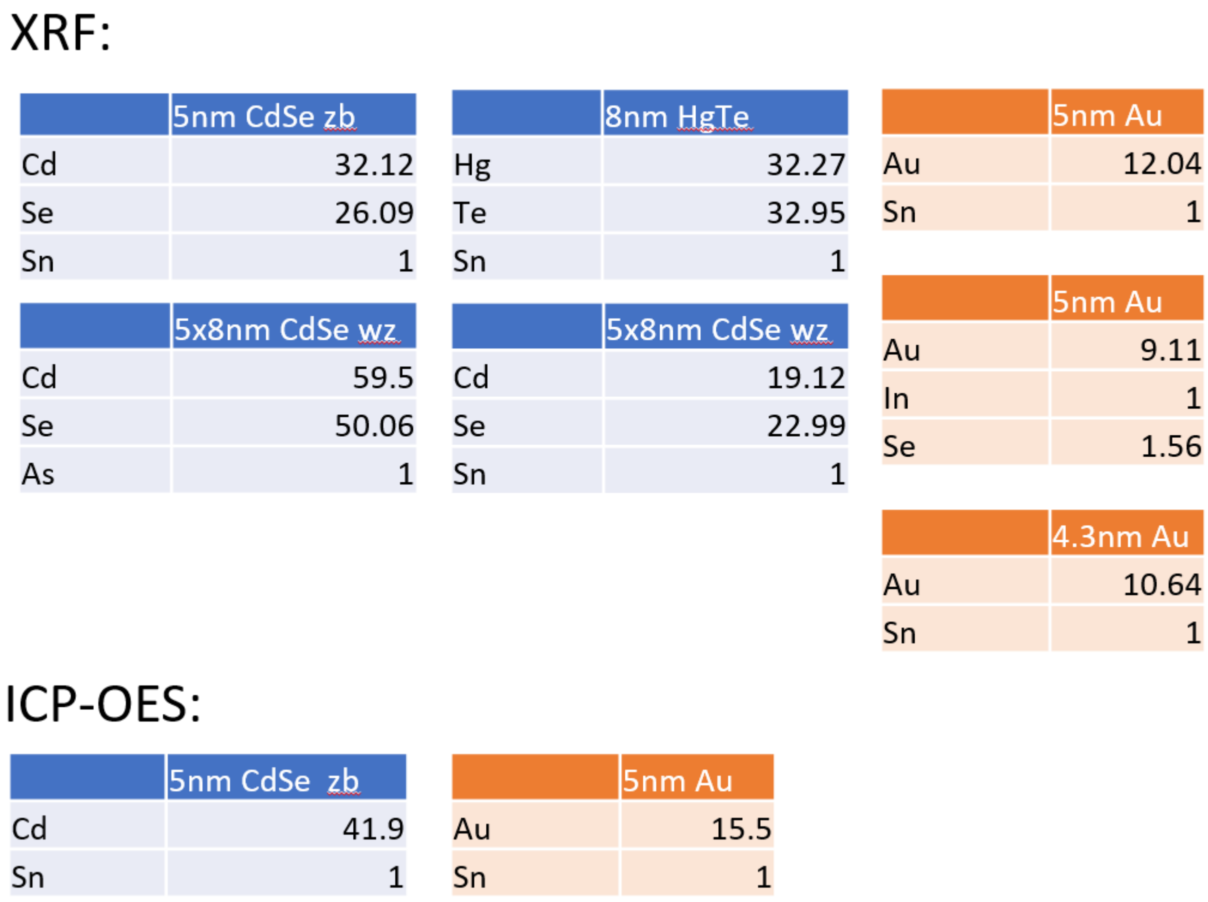

XRF:

	5nm CdSe zb
Cd	32.12
Se	26.09
Sn	1

	8nm HgTe
Hg	32.27
Te	32.95
Sn	1

	5nm Au
Au	12.04
Sn	1

	5x8nm CdSe wz
Cd	59.5
Se	50.06
As	1

	5x8nm CdSe wz
Cd	19.12
Se	22.99
Sn	1

	5nm Au
Au	9.11
In	1
Se	1.56

	4.3nm Au
Au	10.64
Sn	1

ICP-OES:

	5nm CdSe zb
Cd	41.9
Sn	1

	5nm Au
Au	15.5
Sn	1

Table 5-1, Elemental analysis: Elemental analysis by x-ray fluorescence (XRF) and inductively coupled plasma atomic emission spectroscopy (ICP-OES) for selected inorganic NCs stabilized in N_2H_4 solution variously by $(N_2H_5)_4Sn_2S_6$, $(N_2H_5)_3AsS_4$, or $(N_2H_5)_4In_2Se_6$. Tables show atomic ratios normalized to the principle heavy element in the ChM species: Sn, In, or As. Orange and blue colors indicate NC materials that are metallic and dielectric respectively. Metallic particles consistently have much more associated ChM for a given amount of NC core material. The samples are prepared from NC colloids that have been washed with acetonitrile to remove excess ChM that is not associated with the particle surfaces. As discussed in the main text, these numbers do not directly correspond to an inorganic ligand "capping density" as ChM species that are surface associated can be either directly chemically bonded to an NC surface, or can be held near a NC surface by electrostatics.

measure effective capping densities that are greater than the density of surface atoms on our metallic nanocrystals. What is measured in assessment of "capping density" for these samples by elemental analysis is the amount of ChM ligands that remain associated with the particles across precipitation and redissolution steps. The implication is that colloidal ChM stabilized metal NPs carry with them a blanket of closely associated ChM$^-$ anions beyond those that are directly grafted to the surface by chemical bonds. Increased concentration of multivalent ions at interfaces of metals and electrolytes has been predicted theoretically[9,16]. These studies identify a role of dielectric mismatch between solid and solution in formation of interfacial image charges that becomes increasingly important for more asymmetric electrolyte solutions. Our ChM salts are highly asymmetric: $(N_2H_5)_4Sn_2S_6$ combines a monovalent cation with a tetravalent anion and represents a likely system for producing observable manifestations of these electrostatic effects.

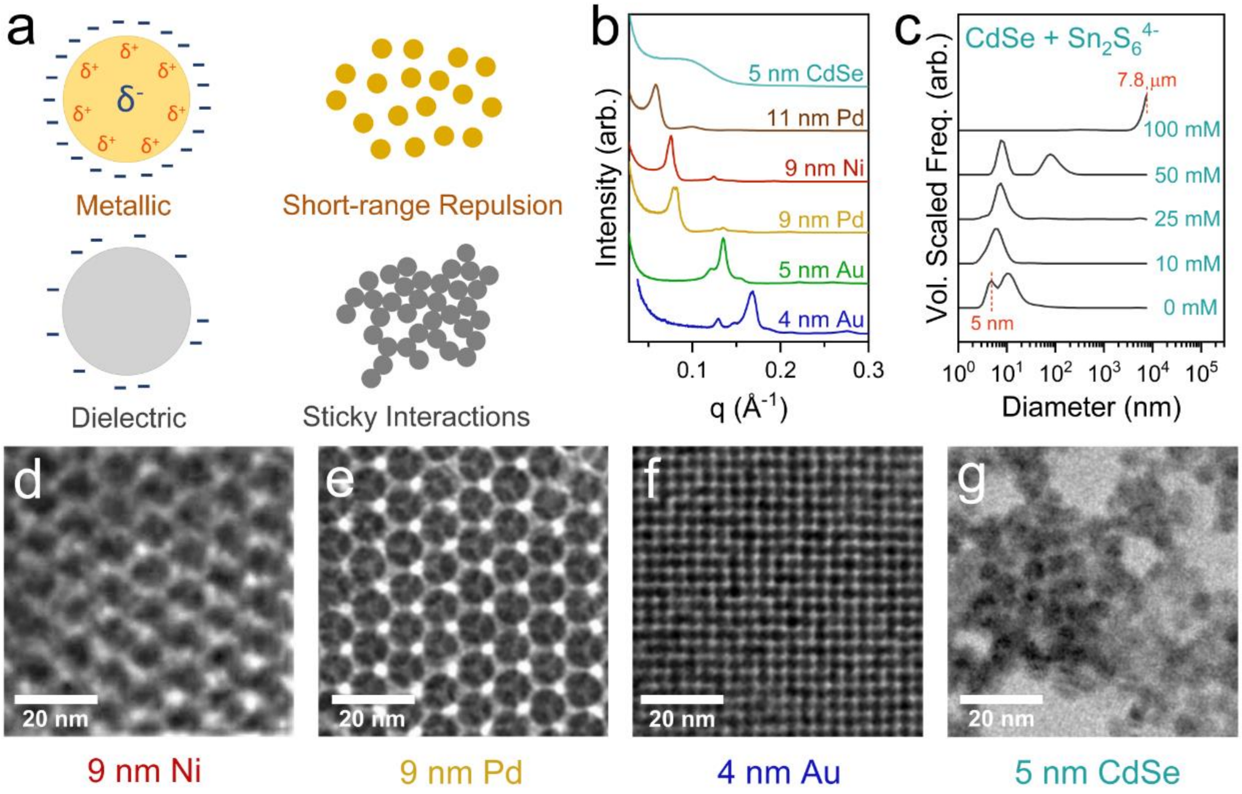

Figure 5-7: Role of NC core material in assembly. **a,** Schematic depicting the effect of dielectric polarizability of the NC core on density of associated anions and the resulting pair potentials. **b,** Linear scale SAXS data of particles of different sizes and core materials aggregated from N_2H_4 with $(N_2H_5)_4Sn_2S_6$. **c,** DLS data showing the uncontrolled fractal aggregation that results from adding $(N_2H_5)_4Sn_2S_6$ to CdSe in N_2H_4. **d,e,** TEM of (111) face of 9 nm Ni and Pd SCs. **f,** TEM of (100) face of 4 nm Au SC. **g.** TEM of CdSe showing disordered aggregation due to sticky short-range interactions.

The ramifications of this hypothesized image charge effect are summarized in Figure 5-7a. The denser layer of anions that are associated with the surface of metal particles produces the short-range repulsive forces that lead to assembly. Dielectric particles develop net-attractive pair potentials when flocculated by ChM salts and undergo the same “sticky aggregation” process that were described previously for metal particles treated with non-binding electrolytes. The difference in structure of aggregates formed by adding $(N_2H_5)_4Sn_2S_6$ to various Au, Pd, and CdSe nanocrystals is summarized in Figure 5-7b. The SAXS data is plotted here to emphasize the range of q-values that correspond to structural correlations on the lengthscale of a particle diameter. For all the various sizes of metallic nanocrystals that we investigate, I find evidence of dense packing in the form of sharp diffraction features that are related to the uniformity of the first coordination spheres of the particles that make up the aggregates. The much broader structure factor peak seen in the CdSe data is the result of loose packing and a high variation in the local packing density across the ensemble of nanocrystals in the aggregate. The behavior of CdSe upon addition of ChM species can also be tracked by in-situ DLS (Figure 5-7c) to monitor the onset of aggregation. Here we see a behavior that is phenomenologically similar to what was observed for Au NPs + $NaNO_3$ (Figure 5-7c). CdSe particles undergo uncontrolled aggregation to branching structures of micron scale dimensions whether they are destabilized by ChM salts or by non-binding electrolytes. Comparing TEM images (Figure 5-7d–g) of metallic and dielectric particles precipitated by $(N_2H_5)_4Sn_2S_6$ addition reinforces this point. While metallic particles of various sizes and types are able to reach a low-energy crystalline state, particles of dielectric materials are persistently trapped in loose open structures. Refer to Section 5.7 for a gallery of optical and electron micrographs showing the wide range of ordered structures that can be grown from different sizes and types of metallic nanoparticles.

To gain further insight into the relationship between NC core material and the morphology of the resulting assemblies, I consider the effect of particle polarizability on the effective two–body interaction between them. For this purpose, I collaborated with Trung Dac Nguyen of Northwestern University to study the system by molecular dynamics simulations. Preliminary results are described qualitatively in the remainder of the present section. Calculations were set up to model two NCs surrounded by a dense matrix of anions to compute the apparent repulsive force exerted on each NC. This condition corresponds to the early stage of agglomeration that acts as a precursor to the supercrystalline state for metal NCs. Because of the contrast in dielectric constants between the NCs and the dense anion matrix, there is a material dependent dielectric mismatch that leads to polarization effects at the NC surfaces.

Our results show that for NCs made of metallic materials the condensed counterions form a dense layer on the NC surface, whereas for dielectric NCs, the counterions are loosely associated with the NC surface. This is due to the larger dielectric mismatch between metallic NC cores and the surrounding electrolyte solution compared to that for dielectric NCs. The larger mismatch in turn leads to stronger polarization effects at metallic NC surfaces. Polarization effects are manifested by a greater magnitude of the positive induced charge, allowing accumulation a denser field of anions around the metallic NC surfaces. The radial density profiles of the anions for varying dielectric constants of the NPs indeed reveal that as the NC dielectric constant increases (i.e., as the NCs become more metallic), the anions accumulate in denser layers near the NC surface. Regardless of the interparticle separation, the condensed anion layers remain relatively intact, indicating that the driving force for the counterion condensation results from the attraction between the anions and the induced charges at the NC surface arising due to polarization effects. As the anion valency is decreased, the surface induced charges are reduced, leading to a loosely packed condensed anions, which again is consistent with experimental observations when monovalent and divalent anions are used in place of tri- and tetra- valent chalcogenidometallate species.

The accumulation of the condensed ChM anions in turn leads to stronger repulsive forces exerted on individual NCs as the NC dielectric constant increases. For dielectric NPs, the repulsive force does not change with the NC-NC distance; whereas, the short-range repulsion between the metallic NCs increases substantially as they approach each other. It is the repulsive force at short range between the NCs that prevents the formation of the branched aggregates early in the assembly process, and favors the re-arrangement of the NCs from a dense disordered structure into an ordered lattice to minimize the total repulsion forces, or equivalently, to minimize the system potential energy.

5.6. Concluding remarks on assembly of electrostatically stabilized colloids to form ordered all-inorganic composites

In summary, I have described a new method for growing composite materials consisting of ordered, three-dimensional, arrays of metal nanoparticles surrounded by a ~0.5 nm thick encapsulating matrix of an arbitrary chalcogenide glass. The nanoparticles that compose these supercrystals are preserved as separate units but with strong electronic coupling between them that allows for metallic transport across the assembly. Our investigations into the mechanism of assembly have found that formation of ordered phases by flocculation of an electrostatically stabilized colloid requires that the nanoparticles be metallic and the flocculating agent, a charge asymmetric ChM salt. Due to polarization effects, metal nanoparticles that are exposed to an increasing concentration of ChM ligand solution accumulate a dense cloud of bulky anions which hinders jamming and allows for energy minimized, ordered phases to appear. The resulting supercrystals represent an important step toward bottom-up design of composite materials by assembly of nanocrystal building blocks. More broadly, an understanding of assembly of charge stabilized nanocrystals under a specific subset of conditions can inform efforts toward achieving ordered assemblies under other more general conditions. Assembly of electrostatically stabilized nanocrystals of dielectric materials should be possible through engineering surface chemistries that supply the necessary repulsive forces to avoid jamming and archive ordering analogous to what is presently achievable with metallic particles. Semiconductor nanocrystals represent the most potentially interesting system in this regard and offer the possibility of new electronic band structure[17] emerging if a sufficient degree of order[18] and coupling strength[19] can be attained. Future work may push assembly of electronically coupled nanocrystals into this regime by use of ultra-monodisperse colloids assembled with ligands that allow very strong electronic coupling.

Thinking beyond assembly, densification of nanocrystal building blocks is desirable in a wide array of applications. For many of these, ordering of the nanocrystal sub-units will not be critical. For quantum dot LEDs, solution processed high-k dielectric layers, and printed wires made from inks of metallic NCs, supercrystalline order will be important mainly insofar as it allows higher achievable densities. In this sense, the value of the assembly study is as a demonstration of the relationship between physical properties of nanocrystals, their composition, and the resulting pair potentials. It serves to further understanding of how to engineer nanocrystal inks with high weight loading of particles while preventing jamming and allowing free flow through narrow diameter tubing. An important direction for future investigation could then be to move along a more applied tack and conduct a detailed study of rheology and wetting properties of concentrated metallic inks with an eye on developing patterned or 3D printed metals with a minimal thermal processing. Current methods for 3D printing conductors rely on high temperature annealing to sinter micron scale metal powders[20]. By using nanoscale precursor particles and thoroughly understanding the interplay between formulation chemistry and morphology of the deposited material, new Effects of both inorganic additives, i.e. ChM ligands and volatile surfactant species such as n-butylamine could be investigated in a search for an ink formulation with the desired rheology and which leaves smooth, dense material upon drying, and yields high conductivity with minimal post-processing.

5.7. Gallery of selected micrographs depicting metal nanoparticles assembled by chalcogenidometallate flocculation

Image captions denote the particle diameter, composition, ChM species, and solvent medium. Images are acquired by TEM with 300 kV accelerating voltage unless otherwise specified.

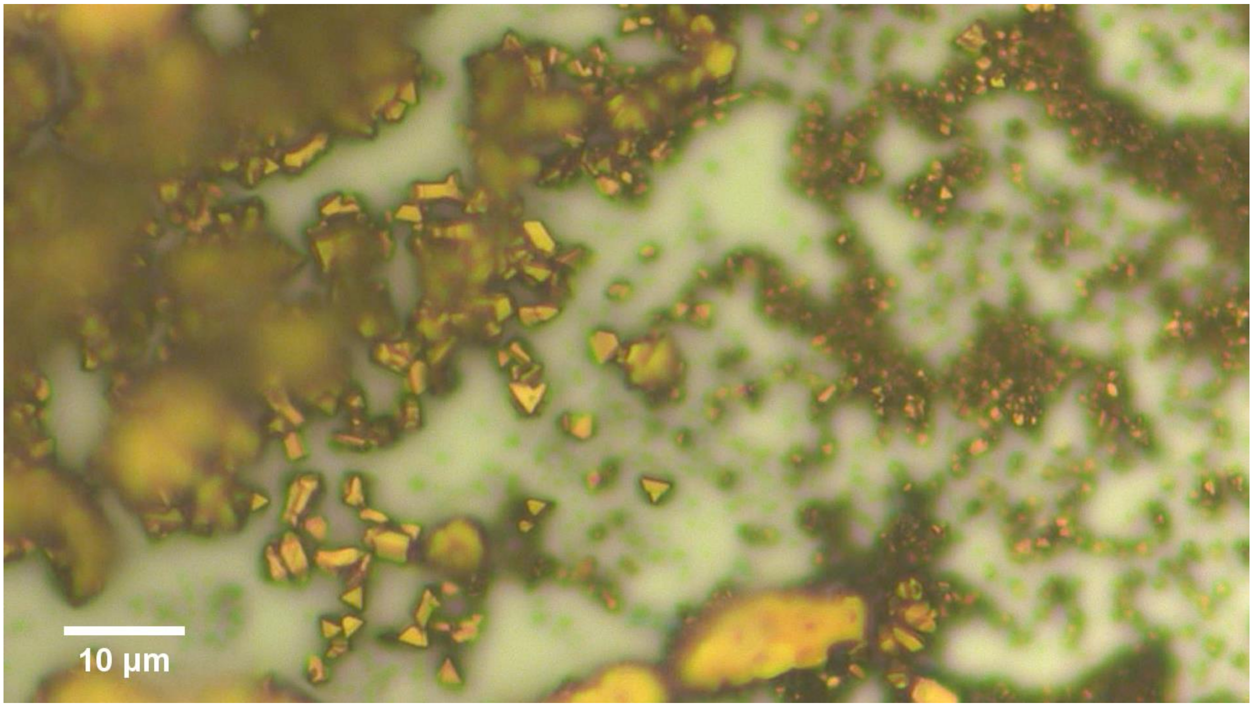

Figure 5-8: 5 nm Au $(N_2H_5)_4Sn_2S_6$, N_2H_4. Image taken by confocal optical microscope.

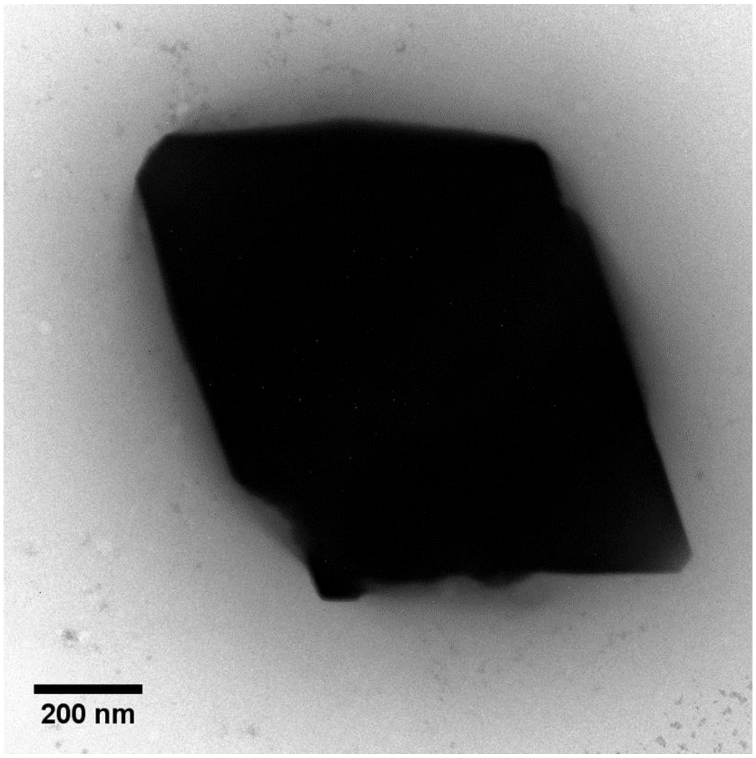

Figure 5-9: 3.8 nm Au $(N_2H_5)_4Sn_2S_6$, N_2H_4

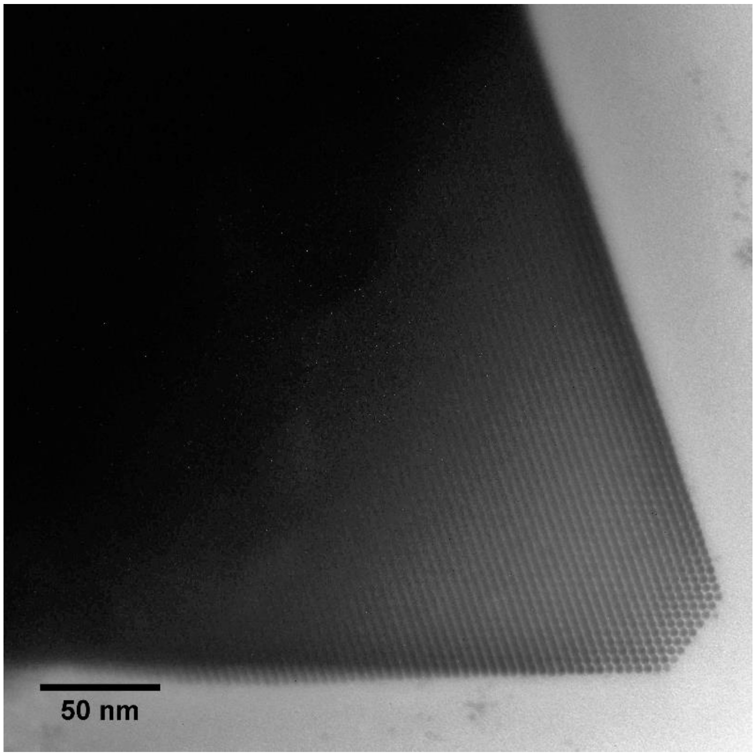

Figure 5-10: 3.8 nm Au $(N_2H_5)_4Sn_2S_6$, N_2H_4 (zoom)

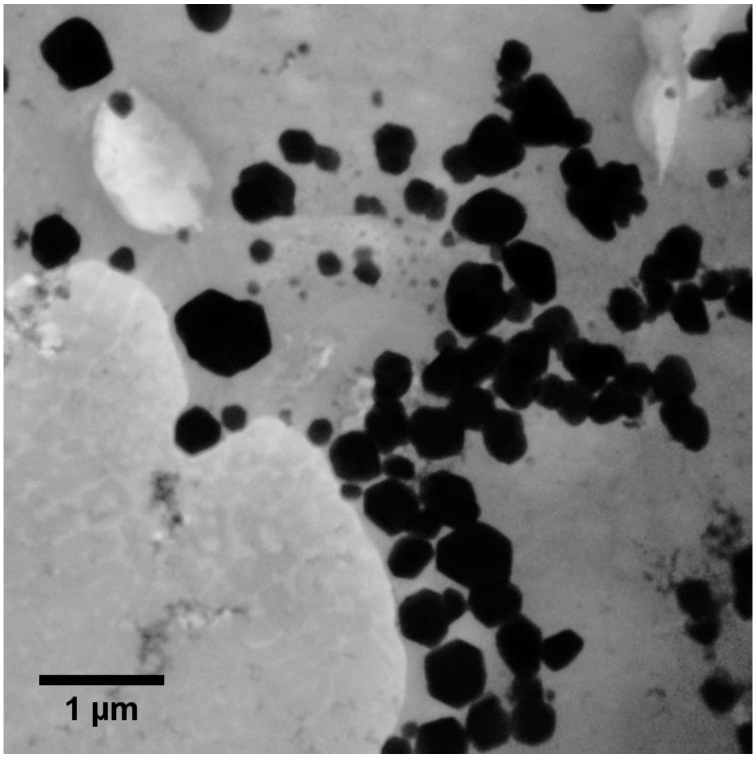

Figure 5-11: 5 nm Au $(N_2H_5)_4Sn_2S_6$, N_2H_4

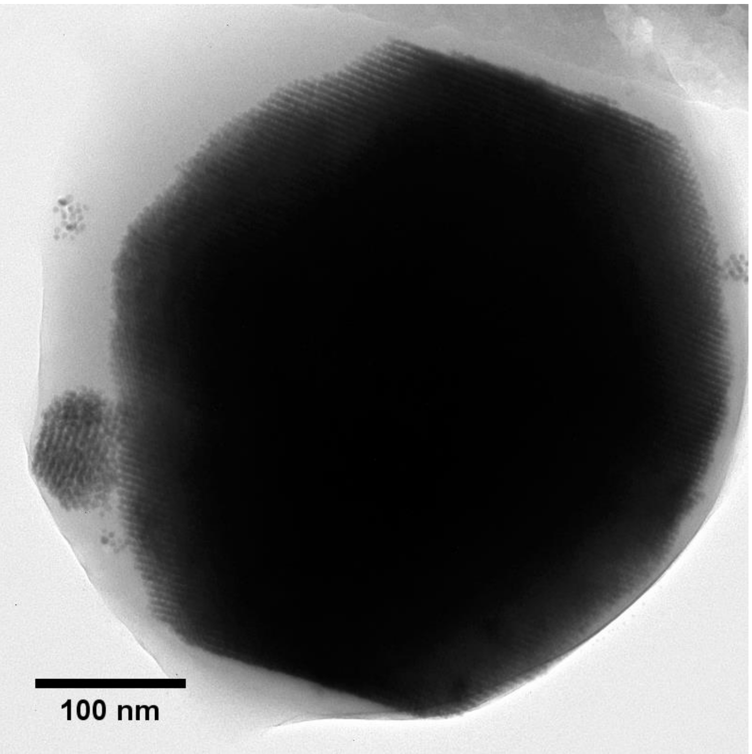

Figure 5-12: 5 nm Au $(N_2H_5)_4Sn_2S_6$, N_2H_4 (zoom)

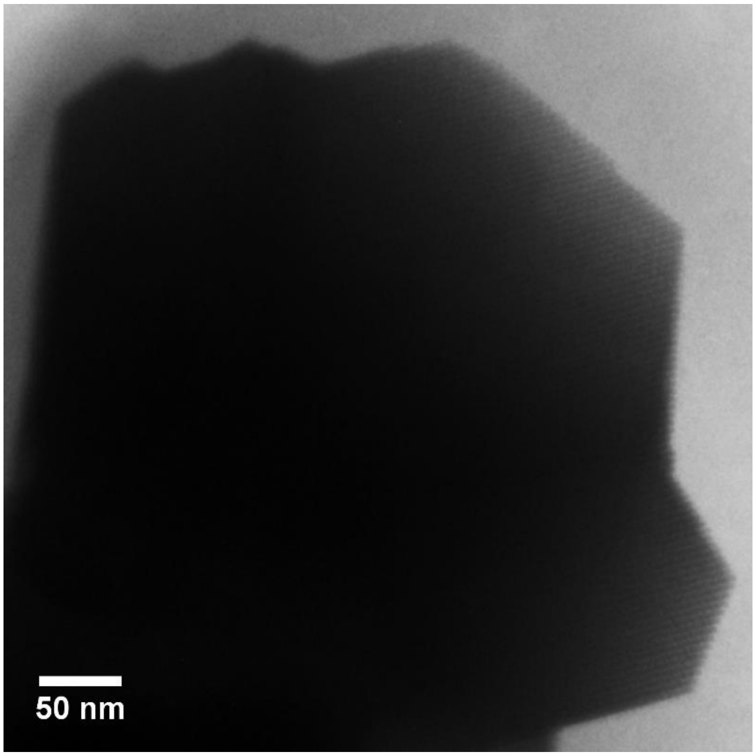

Figure 5-13: 4 nm Pd $(N_2H_5)_3AsS_4$, N_2H_4

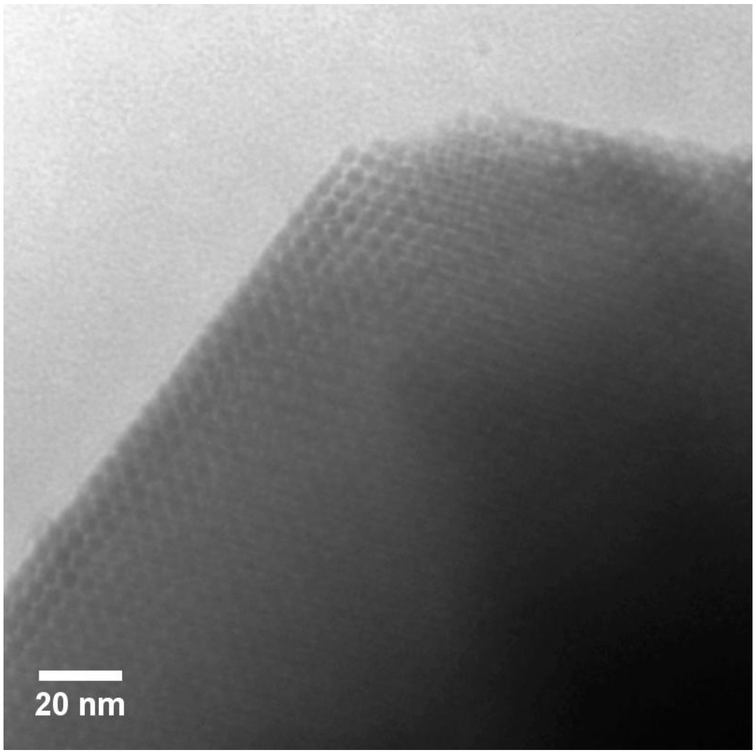

Figure 5-14: 4 nm Pd $(N_2H_5)_3AsS_4$, N_2H_4 (higher magnification)

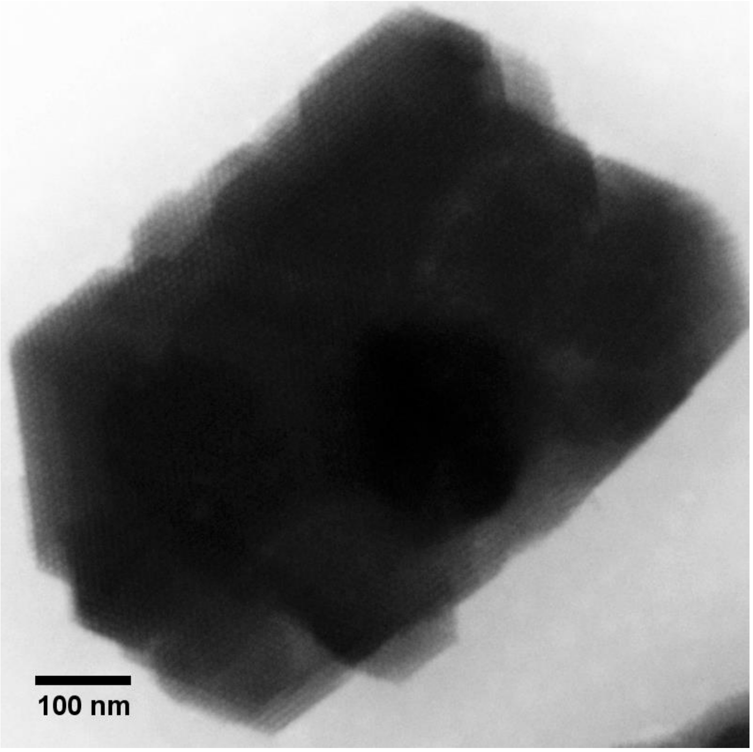

Figure 5-15: 7.5 nm Pd $(N_2H_5)_4Sn_2S_6$, N_2H_4

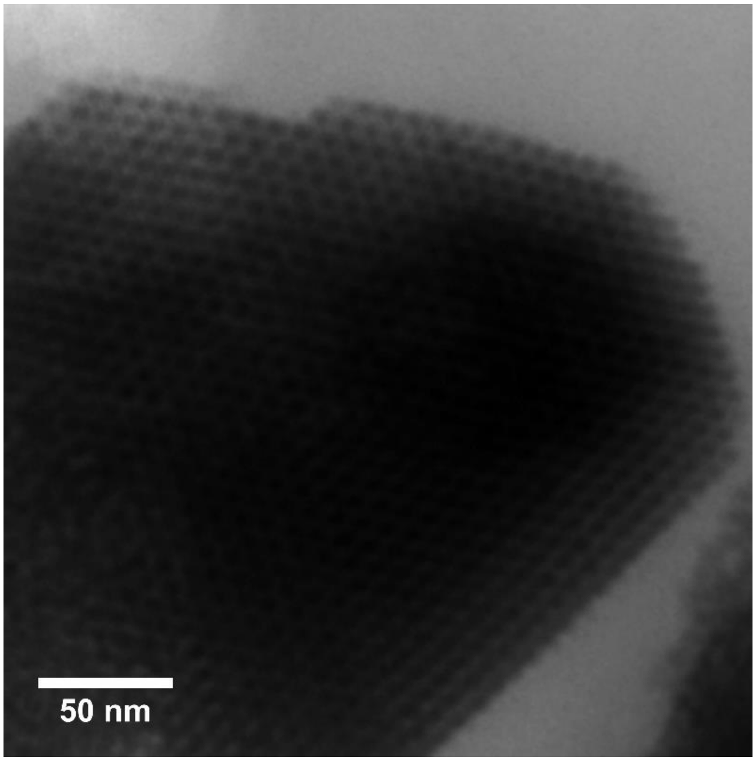

Figure 5-16: 7.5 nm Pd $(N_2H_5)_4Sn_2S_6$, N_2H_4 (zoom)

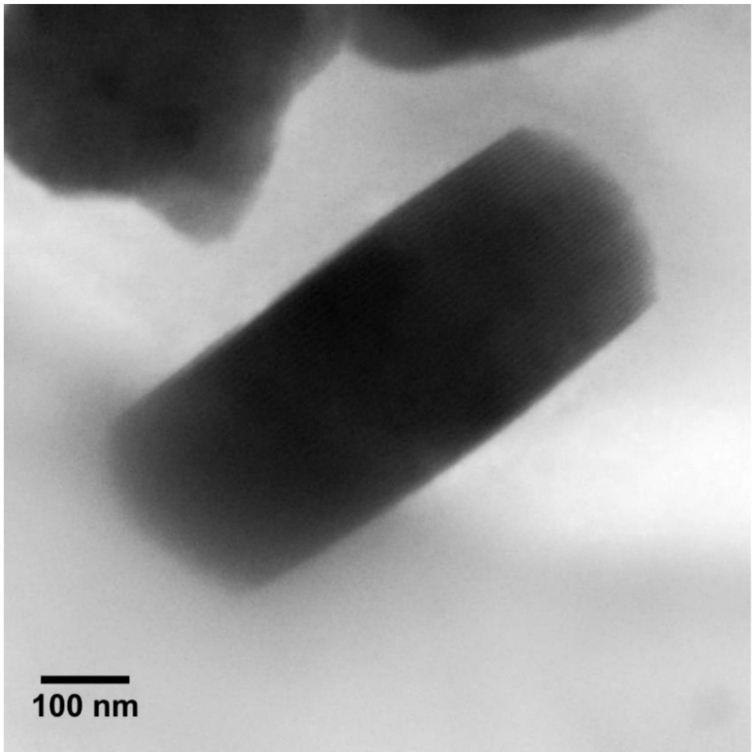

Figure 5-17: 7.5 nm Pd $(N_2H_5)_4Sn_2S_6$, N_2H_4

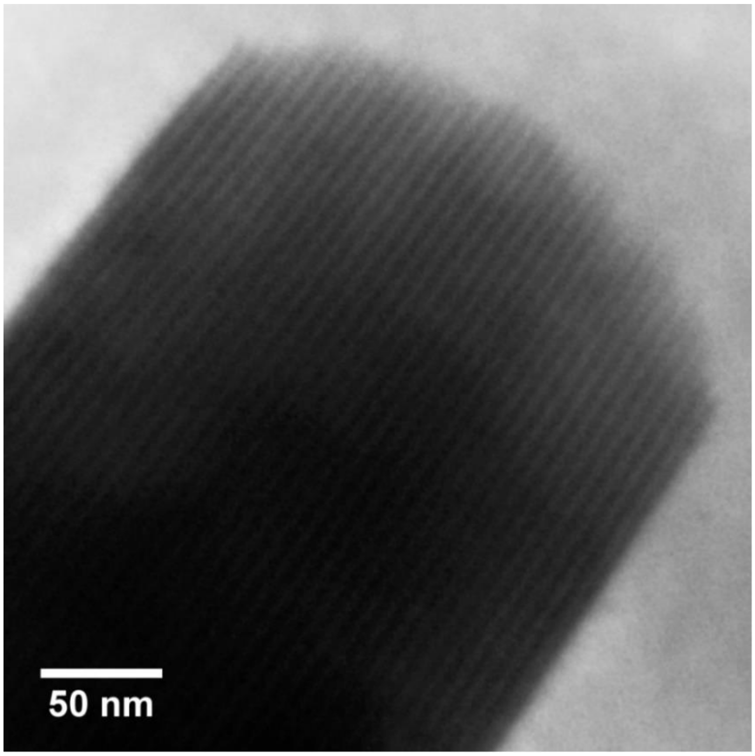

Figure 5-18: 7.5 nm Pd $(N_2H_5)_4Sn_2S_6$, N_2H_4 (zoom)

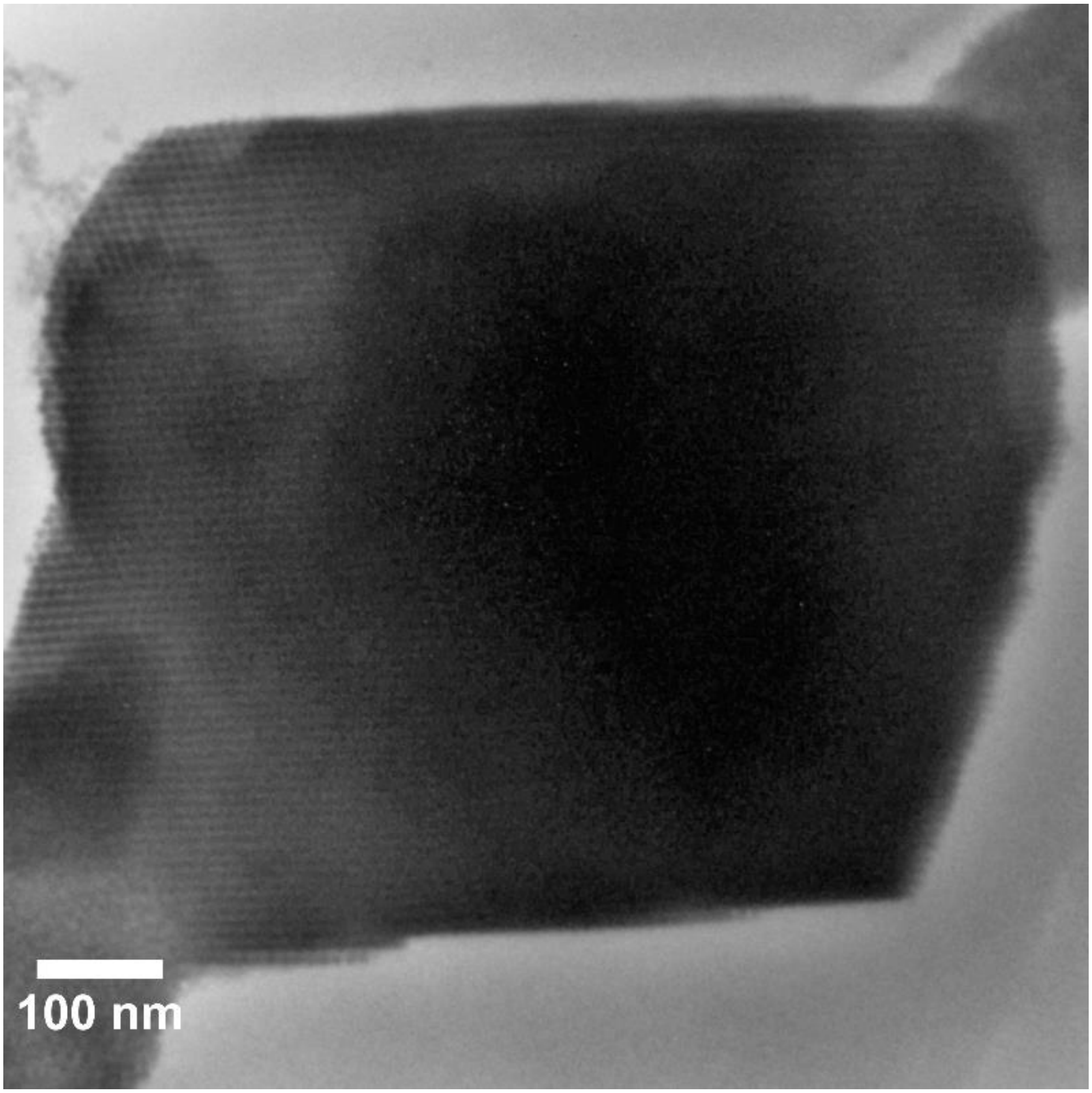

Figure 5-19: 11 nm Pd $(N_2H_5)_4Sn_2S_6$, N_2H_4

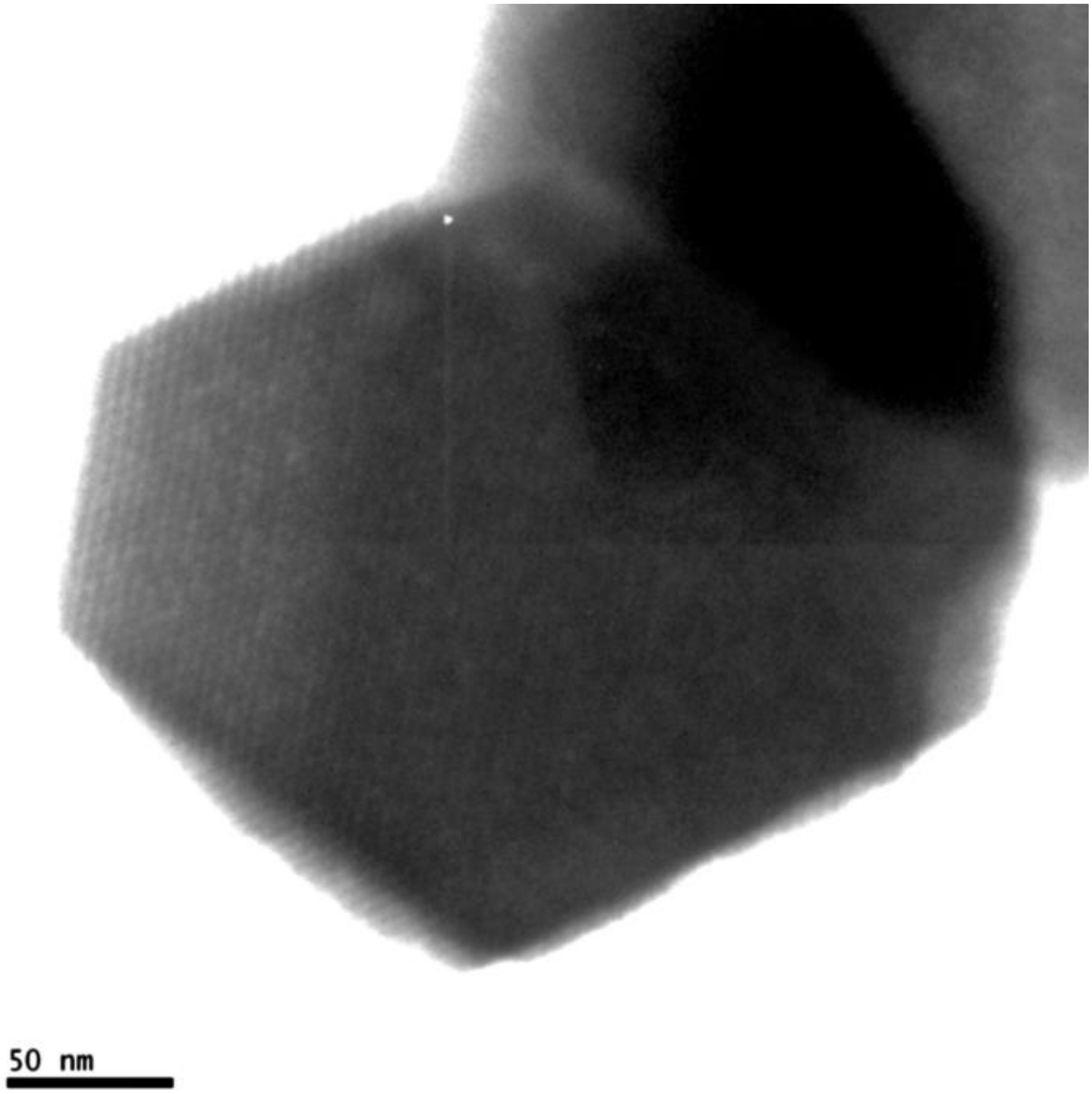

Figure 5-20: 5 nm Au $(N_2H_5)_3AsS_4$, N_2H_4

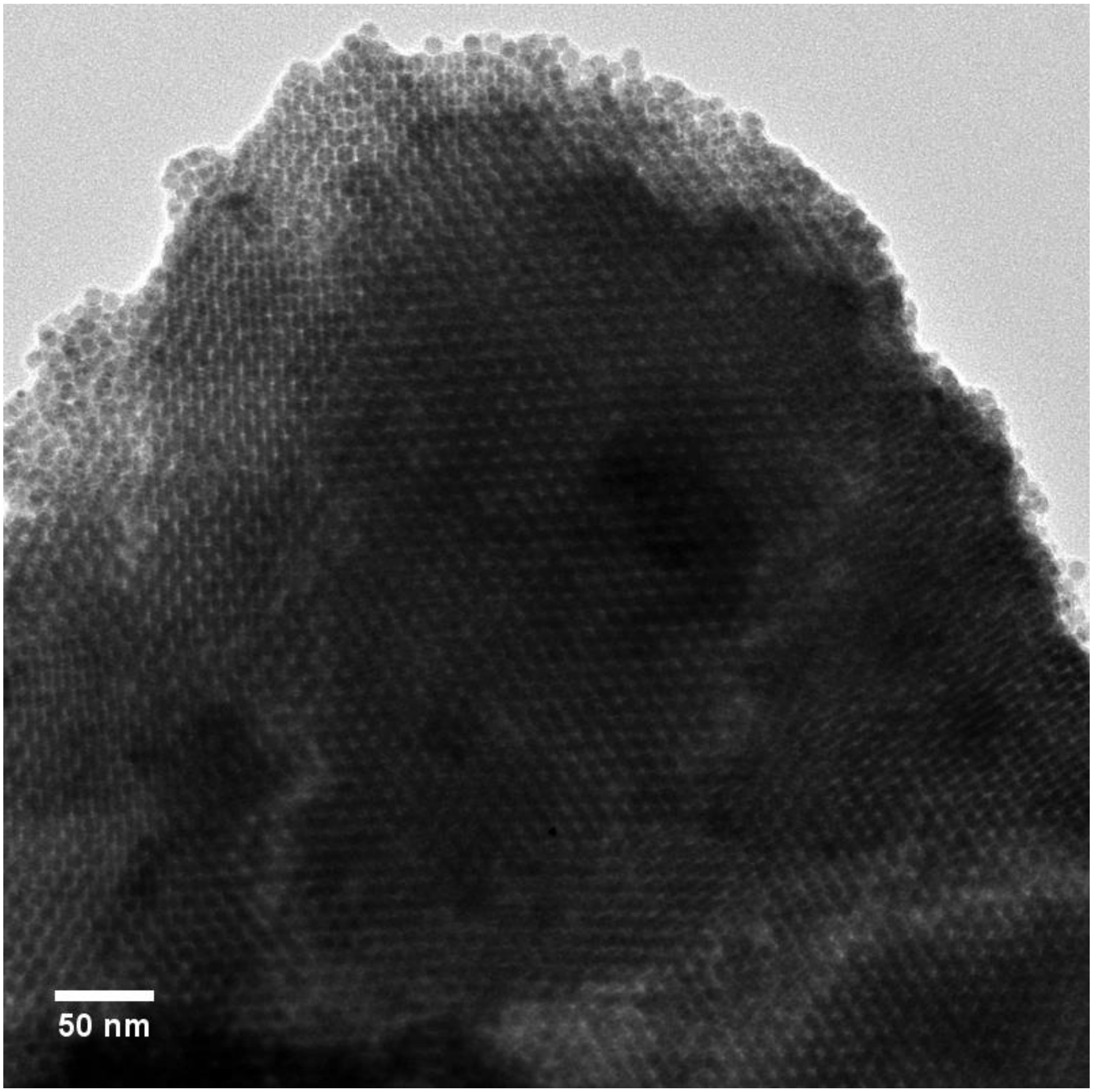

Figure 5-21: 10 nm Ni K_3AsS_3, N-methylformamide

5.8. Chapter 5 bibliography

(1) Boles, M. A.; Engel, M.; Talapin, D. V. *Chemical Reviews* **2016**, *116*, 11220.

(2) Pietra, F.; Rabouw, F. T.; Evers, W. H.; Byelov, D. V.; Petukhov, A. V.; de Mello Donegá, C.; Vanmaekelbergh, D. *Nano Letters* **2012**, *12*, 5515.

(3) Geuchies, J. J.; van Overbeek, C.; Evers, W. H.; Goris, B.; de Backer, A.; Gantapara, A. P.; Rabouw, F. T.; Hilhorst, J.; Peters, J. L.; Konovalov, O.; Petukhov, A. V.; Dijkstra, M.; Siebbeles, L. D. A.; van Aert, S.; Bals, S.; Vanmaekelbergh, D. *Nature Materials* **2016**, *15*, 1248.

(4) Goodfellow, B. W.; Patel, R. N.; Panthani, M. G.; Smilgies, D.-M.; Korgel, B. A. *The Journal of Physical Chemistry C* **2011**, *115*, 6397.

(5) Wu, L.; Willis, J. J.; McKay, I. S.; Diroll, B. T.; Qin, J.; Cargnello, M.; Tassone, C. J. *Nature* **2017**, *548*, 197.

(6) Karthika, S.; Radhakrishnan, T. K.; Kalaichelvi, P. *Crystal Growth & Design* **2016**, *16*, 6663.

(7) Gebauer, D.; Wolf, S. E. *Journal of the American Chemical Society* **2019**, *141*, 4490.

(8) De Yoreo, J. J.; Vekilov, P. G. *Reviews in Mineralogy and Geochemistry* **2003**, *54*, 57.

(9) Guerrero García, G. I.; Olvera de la Cruz, M. *The Journal of Physical Chemistry B* **2014**, *118*, 8854.

(10) Protesescu, L.; Nachtegaal, M.; Voznyy, O.; Borovinskaya, O.; Rossini, A. J.; Emsley, L.; Copéret, C.; Günther, D.; Sargent, E. H.; Kovalenko, M. V. *Journal of the American Chemical Society* **2015**, *137*, 1862.

(11) Mitzi, D. B.; Kosbar, L. L.; Murray, C. E.; Copel, M.; Afzali, A. *Nature* **2004**, *428*, 299.

(12) Mitzi, D. B.; Copel, M.; Chey, S. J. *Advanced Materials* **2005**, *17*, 1285.

(13) Chung, C.-H.; Li, S.-H.; Lei, B.; Yang, W.; Hou, W. W.; Bob, B.; Yang, Y. *Chemistry of Materials* **2011**, *23*, 964.

(14) Lin, M. Y.; Lindsay, H. M.; Weitz, D. A.; Ball, R. C.; Klein, R.; Meakin, P. *Nature* **1989**, *339*, 360.

(15) Kovalenko, M. V.; Scheele, M.; Talapin, D. V. *Science* **2009**, *324*, 1417.

(16) Wang, Z.-Y.; Ma, Z. *Journal of Chemical Theory and Computation* **2016**, *12*, 2880.

(17) L. Lazarenkova, O.; Balandin, A. *Miniband formation in a quantum dot crystal*, 2001; Vol. 89.

(18) Whitham, K.; Yang, J.; Savitzky, B. H.; Kourkoutis, L. F.; Wise, F.; Hanrath, T. *Nature Materials* **2016**, *15*, 557.

(19) Guyot-Sionnest, P. *The Journal of Physical Chemistry Letters* **2012**, *3*, 1169.

(20) Mostafaei, A.; Rodriguez De Vecchis, P.; Nettleship, I.; Chmielus, M. *Materials & Design* **2019**, *162*, 375.